Supporting Information

Dimerization of pillar[5]arene: length-adaptive encapsulation of long-chain guests

Shunsuke Ohtani,*[a] Keigo Nakagawa,[a] Shigehisa Akine,[b,c] Kenichi Kato,[a] and Tomoki Ogoshi*[a,c]

a. Department of Synthetic Chemistry and Biological Chemistry, Graduate School of Engineering, Kyoto University, Katsura, Nishikyo-ku, Kyoto, 615-8510 (Japan)

b. Graduate School of Natural Science and Technology, Kanazawa University, Kakuma-machi, Kanazawa, 920-1192 (Japan)

c. WPI Nano Life Science Institute (WPI-NanoLSI), Kanazawa University, Kakuma-machi, Kanazawa, 920-1192 (Japan)

*Corresponding author: Shunsuke Ohtani, E-mail: otani.shunsuke.6k@kyoto-u.ac.jp; Tomoki Ogoshi, ogoshi.tomoki.3s@kyoto-u.ac.jp.

General

^{1}H NMR and ^{13}C NMR spectra were recorded on JEOL JNM-ECS400, JNM-ECZ500R, and JNMECZ600R spectrometers at r.t., except where noted. Chemical shifts were reported in ppm versus tetramethylsilane (TMS) in chloroform-d_1 ($CDCl_3$). HSQC, HMQC, ^{1}H–^{1}H COSY experiments were performed on a JEOL JNM-ECA600R spectrometer. Analytical thin layer chromatography (TLC) was performed with silica gel 60 Merck F_{254} plates. Column chromatography was performed with Wakosil® 60 (64~210 μm) silica gel. High-resolution mass (HRMS) spectrometry was performed at the Technical Support Office (Department of Synthetic Chemistry and Biological Chemistry, Graduate School of Engineering, Kyoto University), and the HRMS spectra were obtained on a Thermo Fisher Scientific EXACTIVE spectrometer for electrospray ionization (ESI). Recycling preparative gel permeation chromatography (GPC) was performed with JAIGEL–2HR column and JAI LaboACE LC-5060. X-ray crystallographic analysis was carried out by Rigaku Saturn 724+ with MicroMax-007HF CCD diffractometer with Varimax Mo optics using graphite-monochromated MoKα radiation. The structures were solved by direct methods with SHELXT and refined by full-matrix least-squares techniques against F^2 (SHELXL-2018/3) by using Olex2 software package. Binding constants were determined by TitrationFit.[S1]

Materials

Commercially available compounds used without further purification:

1,4-Diethoxybenzene (Tokyo Chemical Industry Co., Ltd.)

Paraformaldehyde (Nacalai Tesque, Inc.)

Boron trifluoride diethyl ether complex ($BF_3 \cdot OEt_2$) (Wako Pure Chemical Industries, Ltd.)

Boron tribromide (BBr_3, 17% in dichloromethane, ca. 1 mol/L) (Tokyo Chemical Industry Co., Ltd.)

Sodium sulfate (Na_2SO_4) (Wako Pure Chemical Industries, Ltd.)

Trifluoromethanesulfonic anhydride (Tokyo Chemical Industry Co., Ltd.)

1,4-Benzenediboronic acid bis(pinacol) ester (Wako Pure Chemical Industries, Ltd.)

X Phos-Pd-G3 (Sigma-Aldrich Co. LLC)

Potassium carbonate (K_2CO_3) (Wako Pure Chemical Industries, Ltd.)

4,4′-Biphenyldiboronic acid (Tokyo Chemical Industry Co., Ltd.)

Oxacyclohexadecane-2-one (Tokyo Chemical Industry Co., Ltd.)

$LiAlH_4$ (powder) (Tokyo Chemical Industry Co., Ltd.)

Sodium hydroxide (NaOH) (Wako Pure Chemical Industries, Ltd.)

Carbon tetrabromide (CBr_4) (Tokyo Chemical Industry Co., Ltd.)

Triphenylphosphine (PPh_3) (Wako Pure Chemical Industries, Ltd.)

Bromo-1-hexadecanol (Wako Pure Chemical Industries, Ltd.)

Octadecanediol (Tokyo Chemical Industry Co., Ltd.)

Dimethylicosanedioate (Tokyo Chemical Industry Co., Ltd.)

1,2-Dibromoethene (**C2**) (Tokyo Chemical Industry Co., Ltd.)

1,3-Dibromopropane (**C3**) (Tokyo Chemical Industry Co., Ltd.)

1,4-Dibromobutane (**C4**) (Tokyo Chemical Industry Co., Ltd.)

1,5-Dibromopentane (**C5**) (Tokyo Chemical Industry Co., Ltd.)

1,6-Dibromohexane (**C6**) (Tokyo Chemical Industry Co., Ltd.)

1,7-Dibromoheptane (**C7**) (Tokyo Chemical Industry Co., Ltd.)

1,8-Dibromooctane (**C8**) (Tokyo Chemical Industry Co., Ltd.)

1,9-Dibrononane (**C9**) (Tokyo Chemical Industry Co., Ltd.)

1,10-Dibromodecane (**C10**) (Tokyo Chemical Industry Co., Ltd.)

1,11-Dibromoundecane (**C11**) (Tokyo Chemical Industry Co., Ltd.)

1,12-Dibromododecane (**C12**) (Tokyo Chemical Industry Co., Ltd.)

1,14-Dibromotetradecane (**C14**) (Wako Pure Chemical Industries, Ltd.)

1,2-Dicyanoethane (Tokyo Chemical Industry Co., Ltd.)

Ethylene glycol (**C2OH**) (Wako Pure Chemical Industries, Ltd.)

1,14-Tetradecanediol (**C14OH**) (Wako Pure Chemical Industries, Ltd.)

Commercially available solvents used without further purification:

1,2-Dichloroethane (Wako Pure Chemical Industries, Ltd.)

Methanol (Wako Pure Chemical Industries, Ltd.)

Acetone (Wako Pure Chemical Industries, Ltd.)

Dehydrated dichloromethane (Kanto Chemical Co., Inc.)

Dichloromethane (DCM) (Wako Pure Chemical Industries, Ltd.)

Hexane (Wako Pure Chemical Industries, Ltd.)

Ethyl acetate (Wako Pure Chemical Industries, Ltd.)

Dehydrated pyridine (Wako Pure Chemical Industries, Ltd.)

Super-dehydrated 1,4-dioxane (Wako Pure Chemical Industries, Ltd.)

Chloroform (Wako Pure Chemical Industries, Ltd.)

Toluene (Wako Pure Chemical Industries, Ltd.)

Dehydrated stabilizer free tetrahydrofuran (THF) (Kanto Chemical Co., Inc.)

Dehydrated diethyl ether (Kanto Chemical Co., Inc.)

Ethanol (Wako Pure Chemical Industries, Ltd.)

Chloroform-d_1 ($CDCl_3$) (Cambridge Isotope Laboratories, Inc.)

Compounds prepared as described in the literatures

1[S2]

1,13-Dibromotridecane (**C13**)[S3]

Synthesis

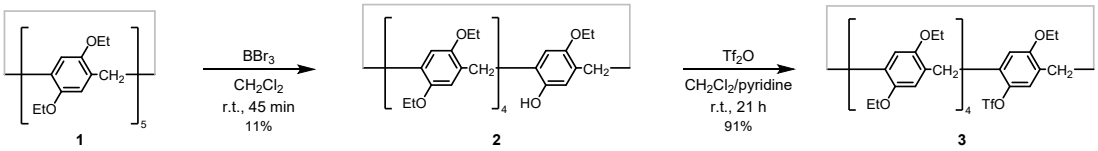

Scheme S1. Synthesis of **3**.

2 was synthesized according to the literature[S4] with slight modification. Under nitrogen atmosphere, **1** (5.0 g, 5.6 mmol) was dissolved into dry DCM (160 mL). BBr_3 (5 mL, 5 mmol) was added to the mixture at 0 °C, and then, it was stirred at r.t. for 45 min. After H_2O was added to the mixture, the organic layer was extracted with DCM and washed with H_2O and brine. The organic layer was dried over anhydrous Na_2SO_4. After filtration, the filtrate was concentrated on a rotary evaporator. The residue was purified by silica gel column chromatography using a mixture of *n*-hexane and ethyl acetate (10/1, *v*/*v*) to afford **2** as a white solid (526 mg, 0.609 mmol, yield: 11%). ^{1}H NMR ($CDCl_3$, 500 MHz, ppm): δ 6.90 (s, 1H), 6.78 (s, 1H), 6.70 (s, 1H), 6.68 (s, 1H), 6.64 (s, 1H), 6.63 (s, 1H), 6.62 (s, 1H), 6.55 (s, 1H), 6.55 (s, 1H), 6.54 (s, 1H), 6.48 (s, 1H), 4.05–3.60 (m, 28H), 1.42–1.01 (m, 27H). The spectroscopic data was identical to those reported in the literature.[S5] The synthetic yield was lower than the reported value, likely due to difficulties in maintaining temperature control on a large scale.

3 was synthesized according to the literature[S6]. Under nitrogen atmosphere, **2** (250 mg, 0.290 mmol) was dissolved into dry DCM (8 mL) and pyridine (0.3 mL). To the solution, trifluoromethanesulfonic anhydride (74 μL, 0.44 mmol) was added at 0 °C, and then, it was stirred at r.t. for 24 h. After H_2O was added to the mixture, the organic layer was extracted with DCM and washed with H_2O and brine. The organic layer was dried over anhydrous Na_2SO_4. After filtration, the filtrate was concentrated on a rotary evaporator. The residue was purified by silica gel column chromatography using a mixture of *n*-hexane and DCM (1/1, *v*/*v*) to afford **3** as a white solid (261 mg, 0.262 mmol, yield: 91%). ^{1}H NMR ($CDCl_3$, 500 MHz, ppm): δ 7.16 (s, 1H), 6.77 (s, 1H), 6.75 (s, 1H), 6.74 (s, 1H), 6.72 (m, 3H), 6.71 (s, 1H), 6.68 (s, 1H), 6.67 (s, 1H), 3.91–3.74 (m, 28H), 1.35–1.22 (m, 24H), 1.15 (t, 3H, J = 7.0 Hz). ^{13}C NMR ($CDCl_3$, 151 MHz, ppm): δ 155.36, 150.05, 150.02, 149.87, 149.84, 149.79, 149.79, 149.58, 149.50, 140.54, 132.61, 129.59, 129.45, 129.05, 128.66, 128.58, 128.47, 128.19, 126.67, 126.01, 123.39, 115.17, 115.11, 115.11, 115.11, 115.11, 115.11, 114.49, 114.43, 114.13, 63.90, 63.88, 63.85, 63.83, 63.83, 63.77, 63.59, 63.47, 63.39, 30.61, 29.96, 29.68, 29.59, 29.54, 15.20, 15.14, 15.07, 15.07, 15.07, 15.03, 14.81, 14.76, 14.71. The spectroscopic data was identical to those reported in the literature.[S6]

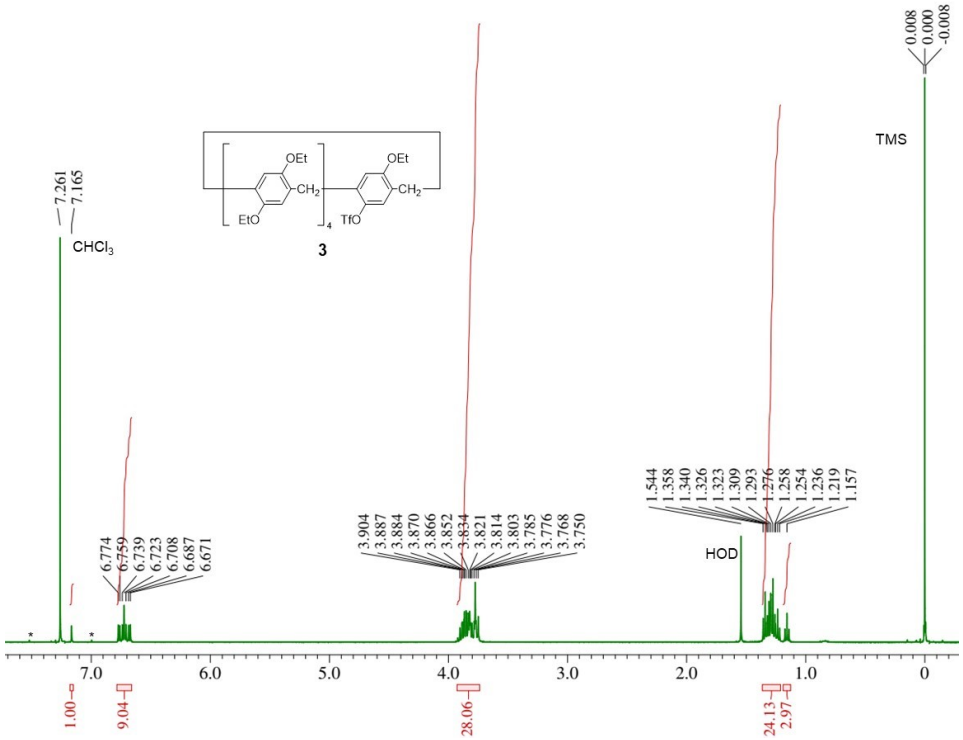

Figure S1. ^{1}H NMR spectrum (500 MHz, $CDCl_3$, 295 K) of compound **3**. Asterisks mean ^{13}C satellites of chloroform peak.

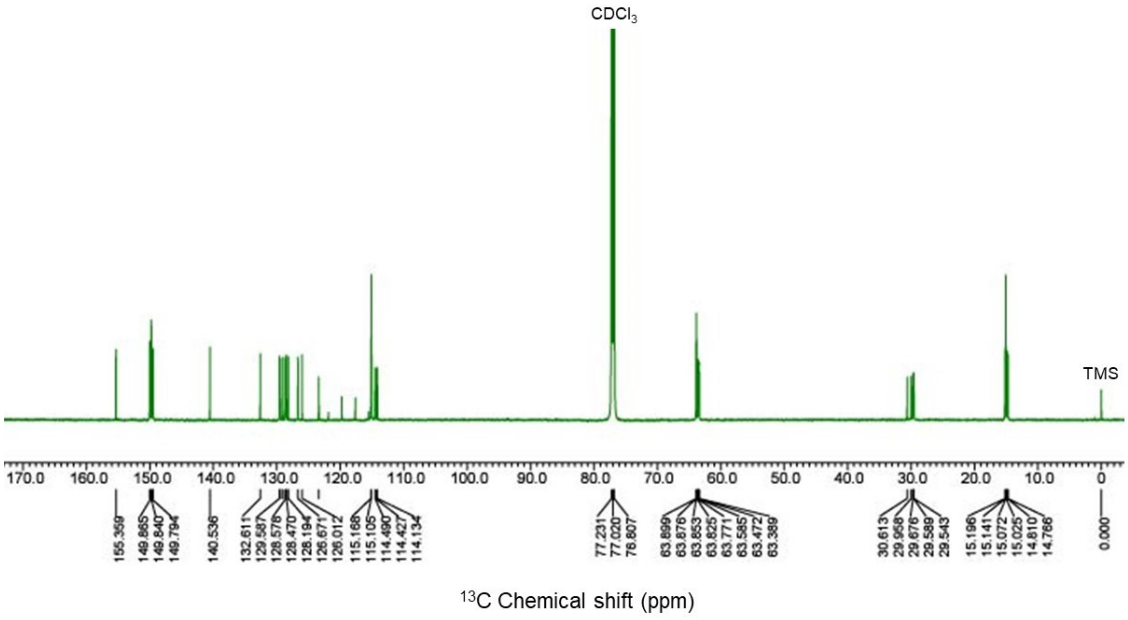

Figure S2. ^{13}C NMR spectrum (151 MHz, $CDCl_3$, 295 K) of compound **3**.

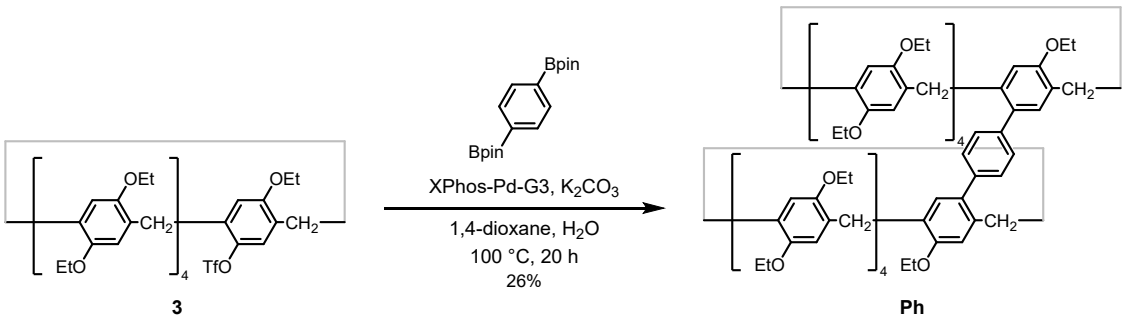

Scheme S2. Synthesis of **Ph**.

Under nitrogen atmosphere, **3** (100 mg, 0.100 mmol), 1,4-benzenediboronic acid bis(pinacol) ester (27 mg, 0.082 mmol), XPhos-Pd-G3 (8 mg, 0.009 mmol) and K_2CO_3 (276 mg, 2.00 mmol) were dissolved into 1,4-dioxane (4 mL) and H_2O (0.8 mL). The mixture was stirred at 100 °C for 20 h, and then, the solvent was removed on a rotary evaporator. The residue was dissolved into DCM and the organic layer was washed with H_2O and brine. The organic layer was dried over anhydrous Na_2SO_4. After filtration, the filtrate was concentrated on a rotary evaporator. The residue was purified by silica gel column chromatography using a mixture of *n*-hexane and ethyl acetate (14/1, *v*/*v*). The residue was further purified by recycling GPC using chloroform as eluent, then recrystallized with *n*-hexane and chloroform to afford **Ph** as a white solid (23 mg, 0.013 mmol, yield: 26%). ^{1}H NMR ($CDCl_3$, 400 MHz, ppm): δ 7.30 (s, 4H), 7.19 (s, 2H), 6.79 (s, 2H), 6.75–6.73 (s, 8H), 6.66 (s, 2H), 6.65 (m, 4H), 6.05 (s, 2H), 3.91–3.54 (m, 56H), 1.33–1.22 (m, 36H), 1.15 (t, 6H, J = 7.0 Hz), 1.09 (t, 6H, J = 7.0 Hz), 0.99 (t, 6H, J = 7.0 Hz). ^{13}C NMR ($CDCl_3$, 151 MHz, ppm): δ 155.60, 150.28, 149.92, 149.87, 149.87, 149.87, 149.80, 149.60, 149.39, 140.29, 138.06, 132.81, 132.77, 129.49, 128.74, 128.70, 128.70, 128.68 128.68, 128.50, 128.34, 127.98, 127.44, 115.71, 115.49, 115.22, 115.17, 115.07, 115.03, 114.69, 114.50, 113.38, 63.92, 63.87, 63.87, 63.87, 63.81, 63.75, 63.67, 63.67, 62.87, 32.45, 31.00, 30.11, 30.00, 29.75, 15.15, 15.10, 15.03, 15.03, 15.01, 15.01, 14.91, 14.80, 14.34. HRMS (ESI): Calcd for $[M+Na]^+$: 1789.9462. Found: 1789.9473.

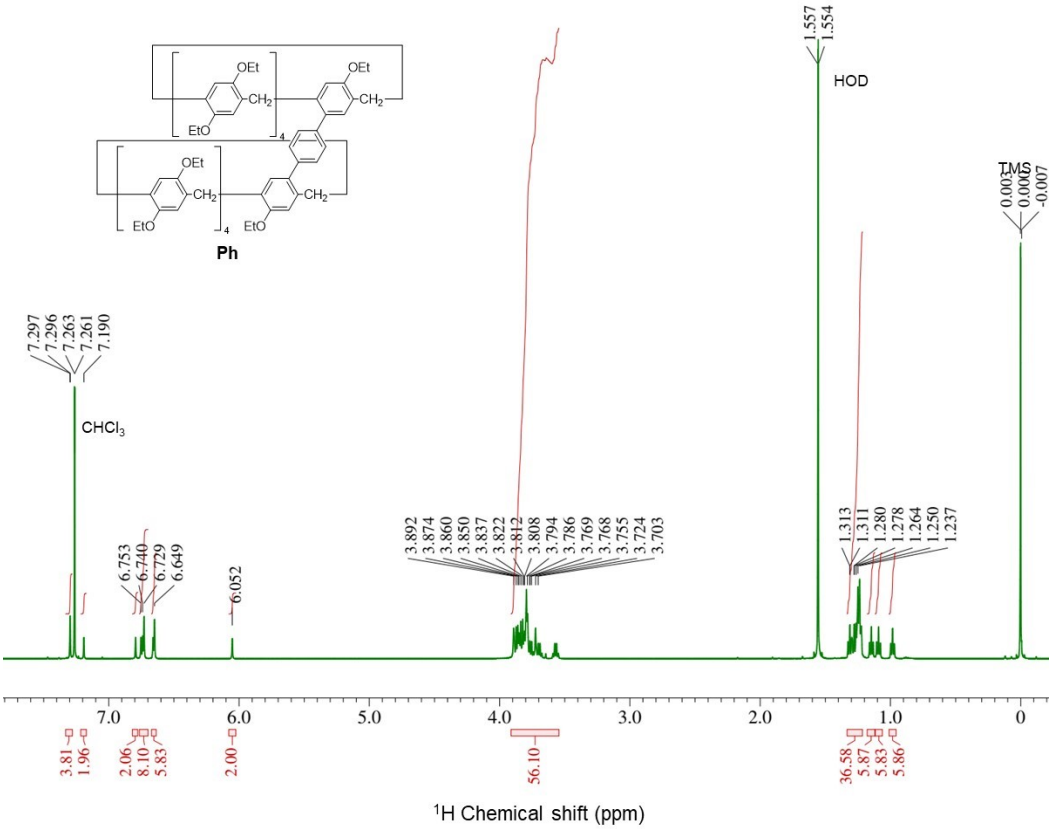

Figure S3. ^{1}H NMR spectrum (400 MHz, $CDCl_3$, 295 K) of **Ph**.

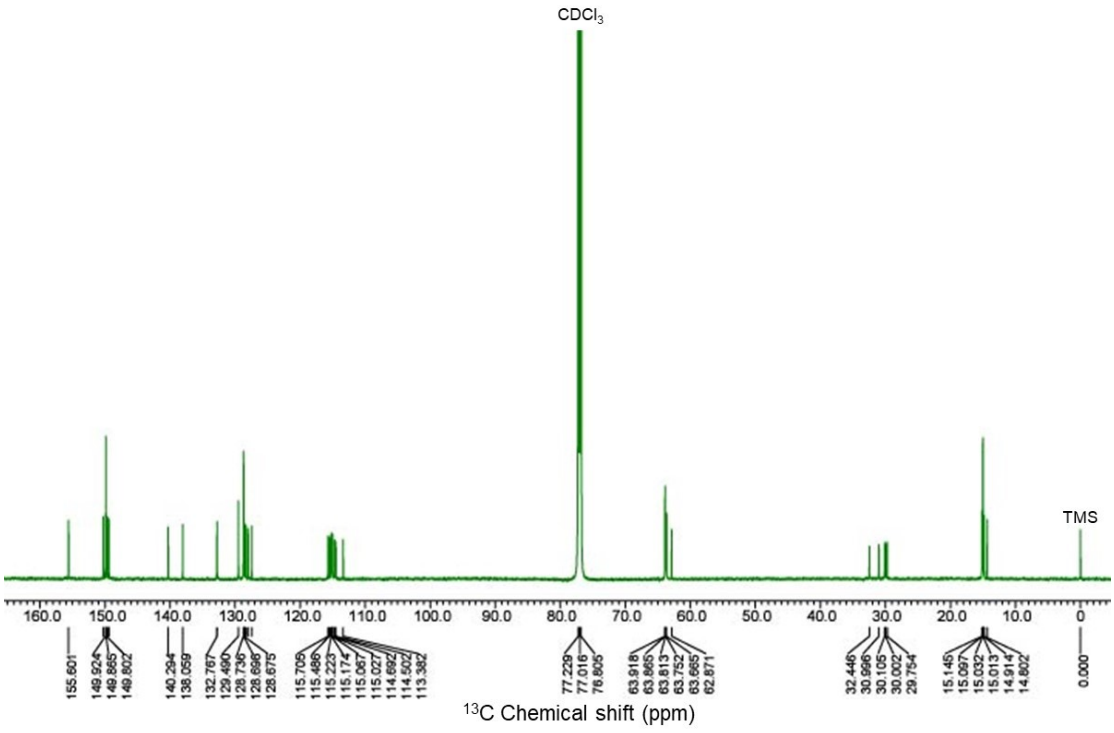

Figure S4. ^{13}C NMR spectrum (151 MHz, $CDCl_3$, 295 K) of **Ph**.

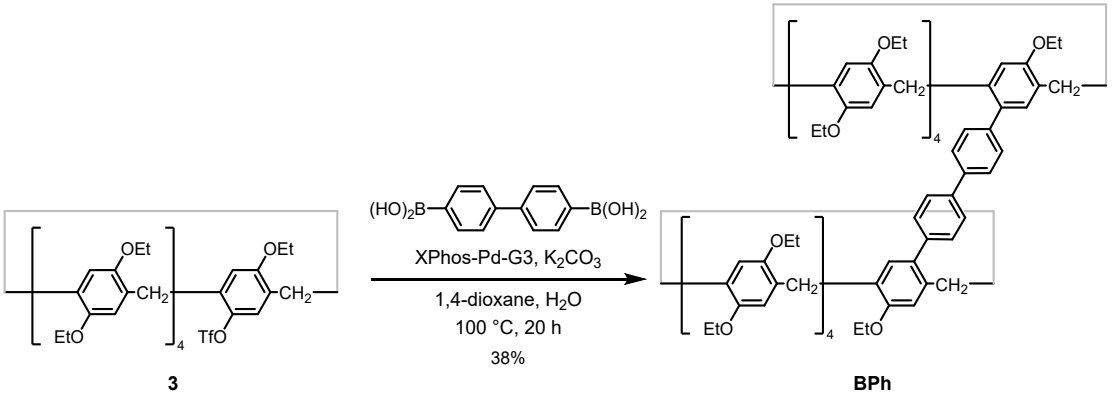

Scheme S3. Synthesis of **BPh**.

Under nitrogen atmosphere, **3** (100 mg, 0.100mmol), 4,4′-biphenyldiboronic acid (20 mg, 0.083 mmol), XPhos-Pd-G3 (8 mg, 0.0095 mmol) and K_2CO_3 (276 mg, 2.00 mmol) were dissolved into 1,4-dioxane (4 mL) and H_2O (0.8 mL). The mixture was stirred at 100 °C for 20 h, then the solvent was removed on a rotary evaporator. The product was dissolved into DCM and the organic layer was washed with H_2O and brine. The organic layer was dried over anhydrous Na_2SO_4. After filtration, the filtrate was concentrated on a rotary evaporator. The residue was purified by silica gel column chromatography using a mixture of *n*-hexane and ethyl acetate (14/1, *v*/*v*). The residue was then purified by recycling GPC using chloroform as eluent, then recrystallized with *n*-hexane and chloroform to afford **BPh** as a white solid (35 mg, 0.019 mmol, yield: 38%). ^{1}H NMR ($CDCl_3$, 600 MHz, ppm): δ 7.63 (d, 4H, J = 8.4 Hz), 7.32 (d, 4H, J = 8.4 Hz), 7.16 (s, 2H), 6.80 (s, 2H), 6.75–6.74 (m, 8H), 6.69 (s, 2H), 6.65 (s, 2H), 6.61 (s, 2H), 5.98 (s, 2H), 3.89–3.53 (m, 56H), 1.33 (t, 6H, J = 6.9 Hz), 1.29–1.21 (m, 30H), 1.12–1.04 (m, 18H). ^{13}C NMR ($CDCl_3$, 151 MHz, ppm): δ 155.65, 150.26, 149.96, 149.90, 149.88, 149.80, 149.78, 149.58, 149.46, 141.52, 138.63, 137.99, 132.64, 132.61, 130.36, 128.77, 128.77, 128.74, 128.73, 128.55, 128.52, 128.41, 127.99, 127.58, 126.38, 115.70, 115.38, 115.27, 115.23, 115.18, 114.99, 114.65, 114.58, 113.58, 63.93, 63.93, 63.90, 63.84, 63.84, 63.82, 63.67, 63.61, 62.96, 32.83, 30.77, 30.03, 29.95, 29.76, 15.17, 15.08, 15.07, 15.07, 15.02, 15.02, 14.81, 14.81, 4.44. HRMS (ESI): Calcd for $[M+Na]^+$: 1865.9775. Found: 1865.9840.

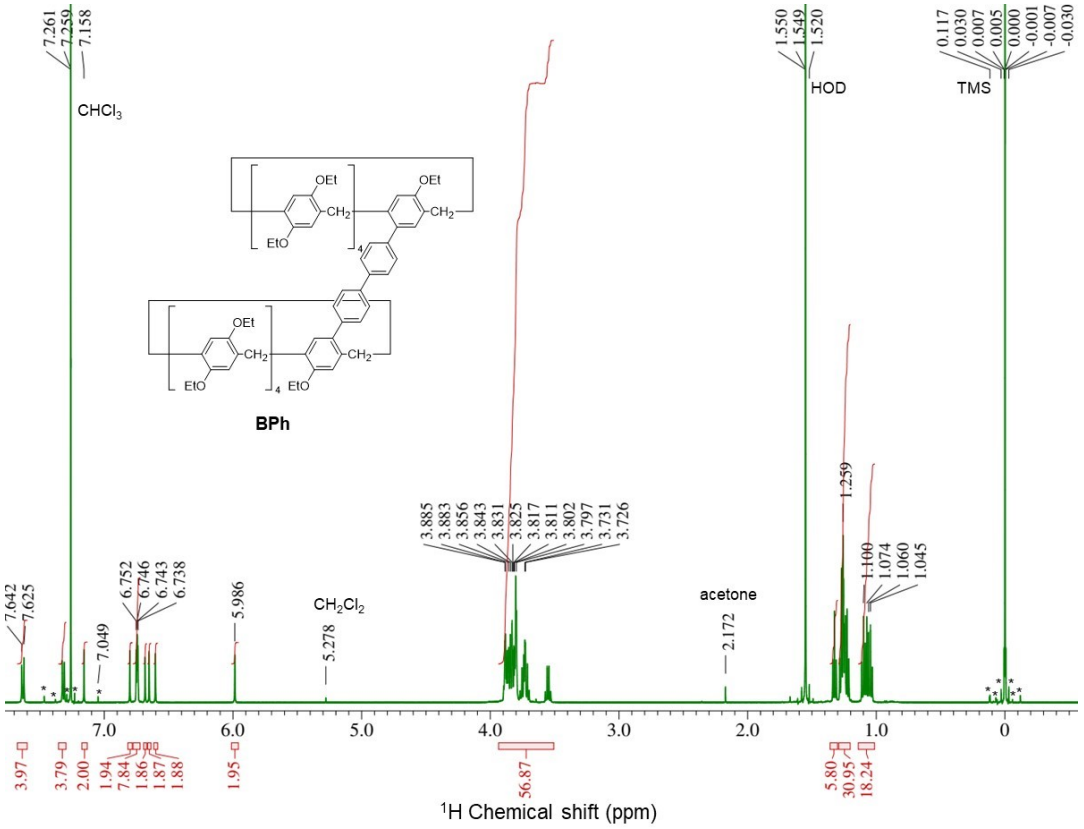

Figure S5. ^{1}H NMR spectrum (600 MHz, $CDCl_3$, 295 K) of **BPh**.

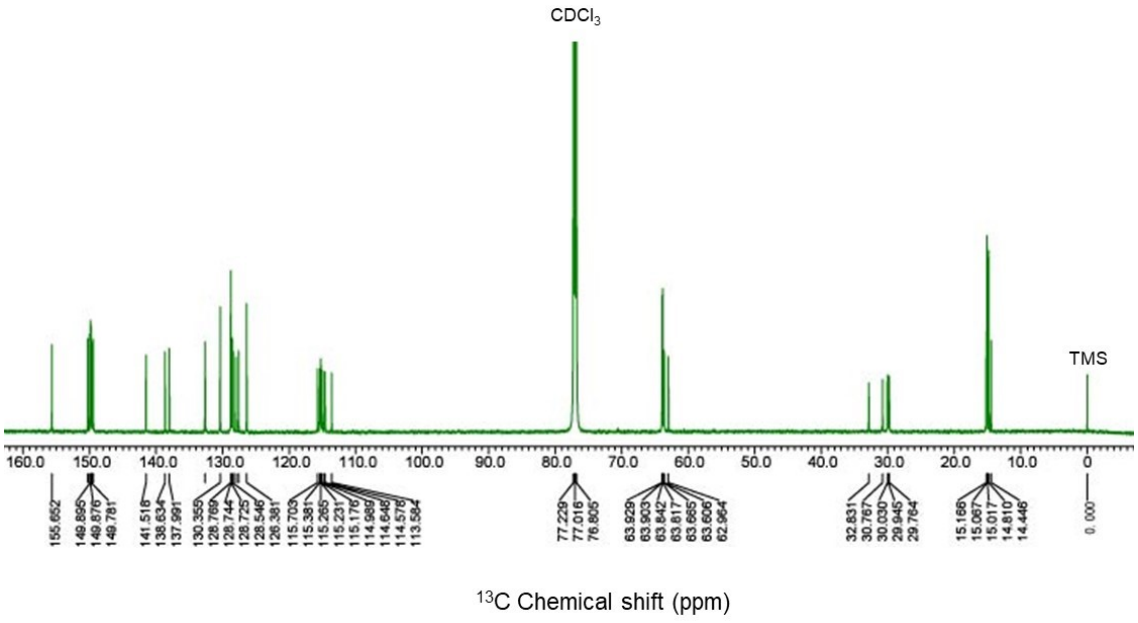

Figure S6. ^{13}C NMR spectrum (151 MHz, $CDCl_3$, 295 K) of **BPh**.

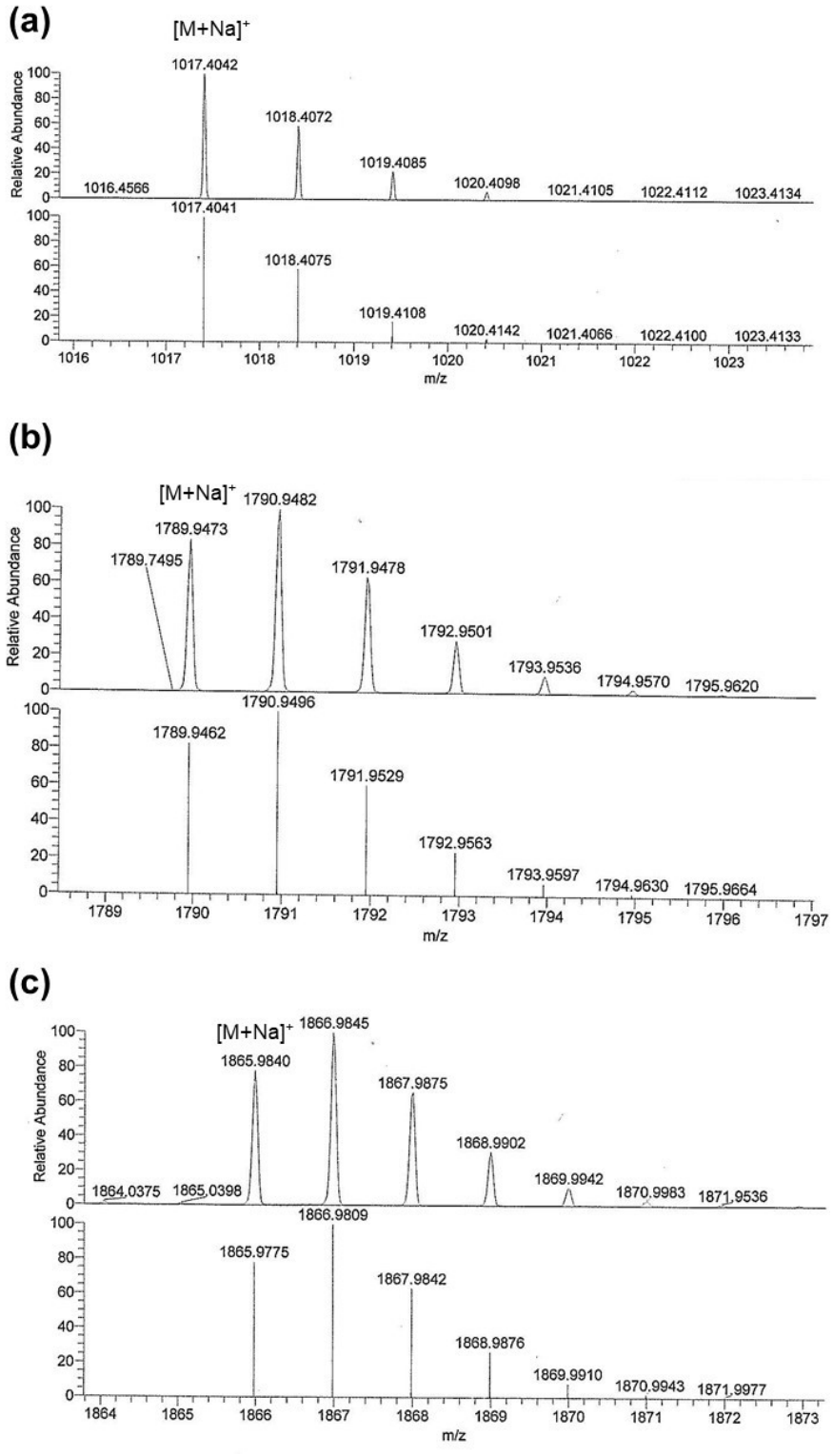

Figure S7. Observed (top) and simulated (bottom) ESI-MS spectra of (a) **3**, (b) **Ph** and (c) **BPh**.

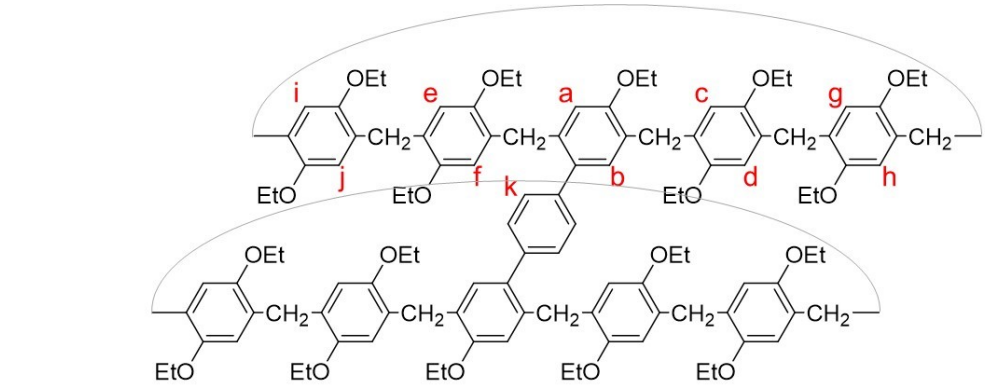

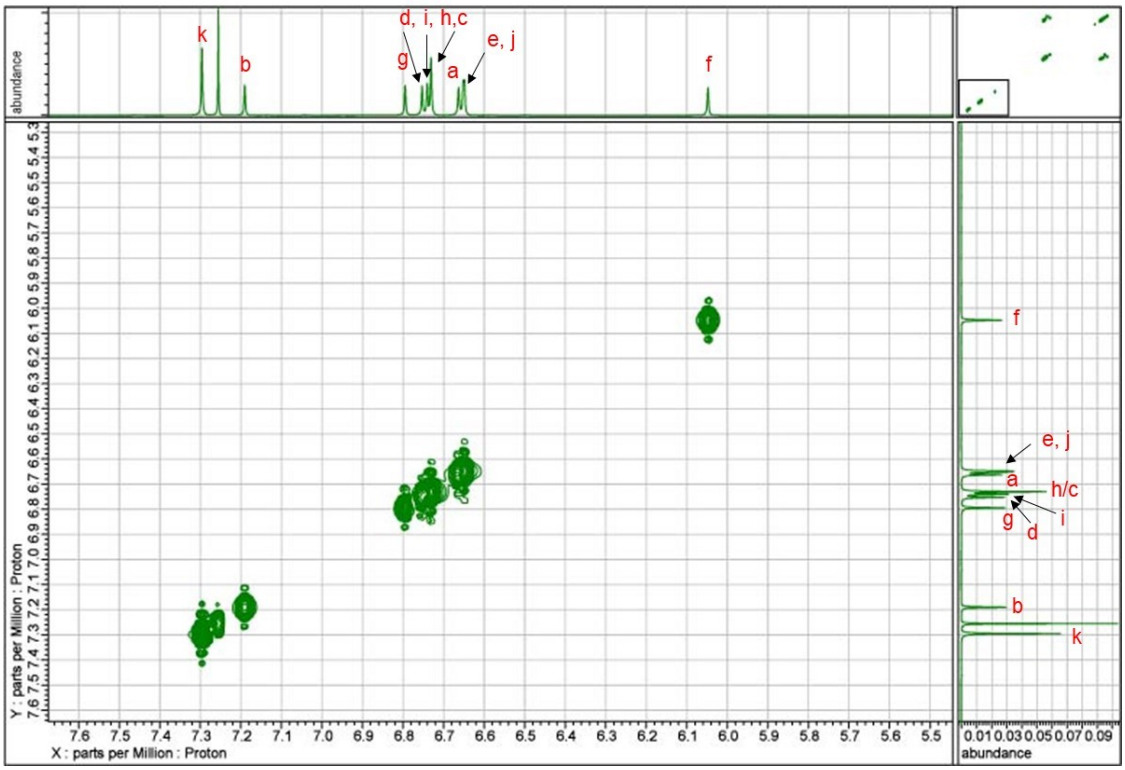

Figure S8. Partial $^{1}H–^{1}H$ COSY correlations (500 MHz, $CDCl_3$, 295 K) of **Ph**.

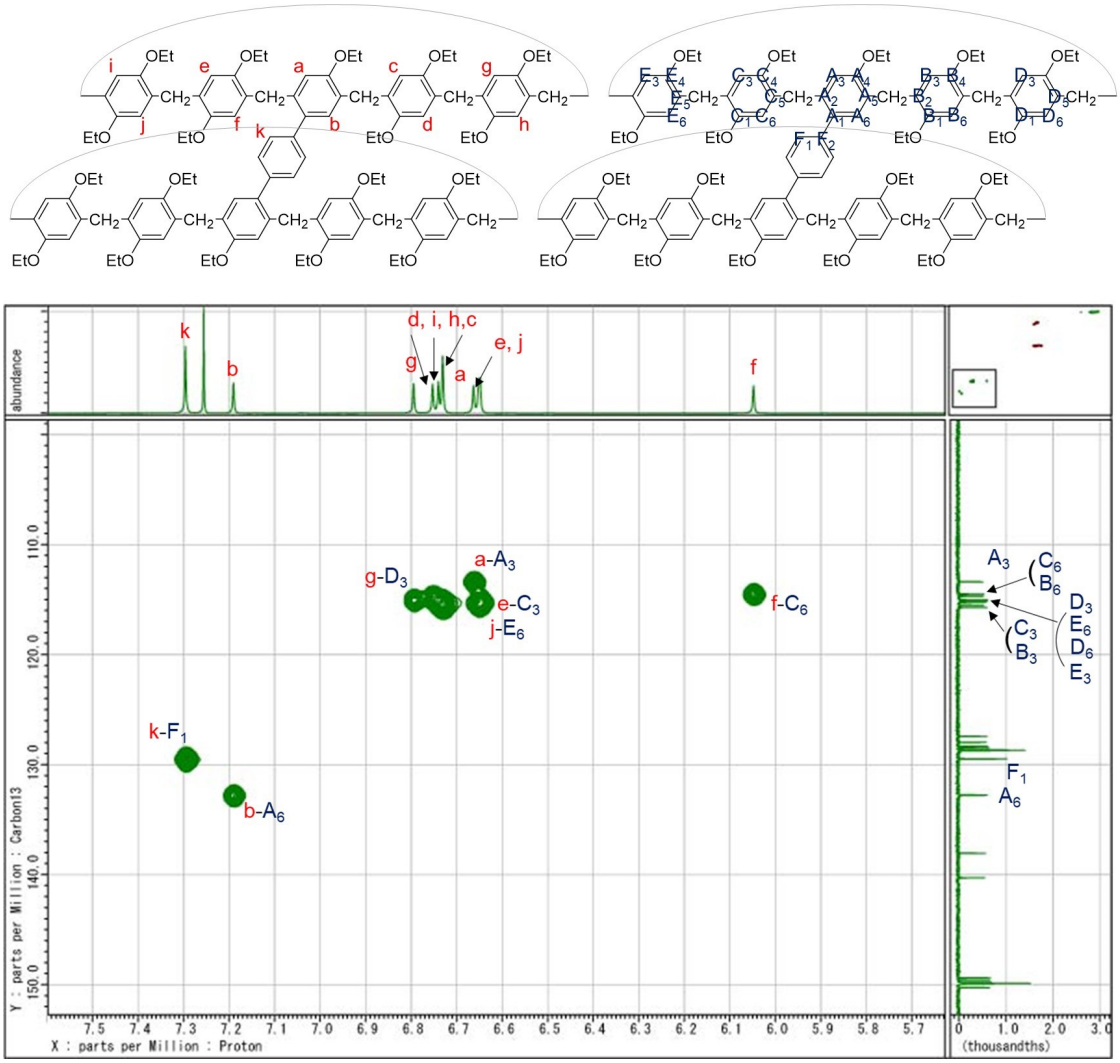

Figure S9. Partial HSQC correlations (500 MHz, $CDCl_3$, 295 K) of **Ph**.

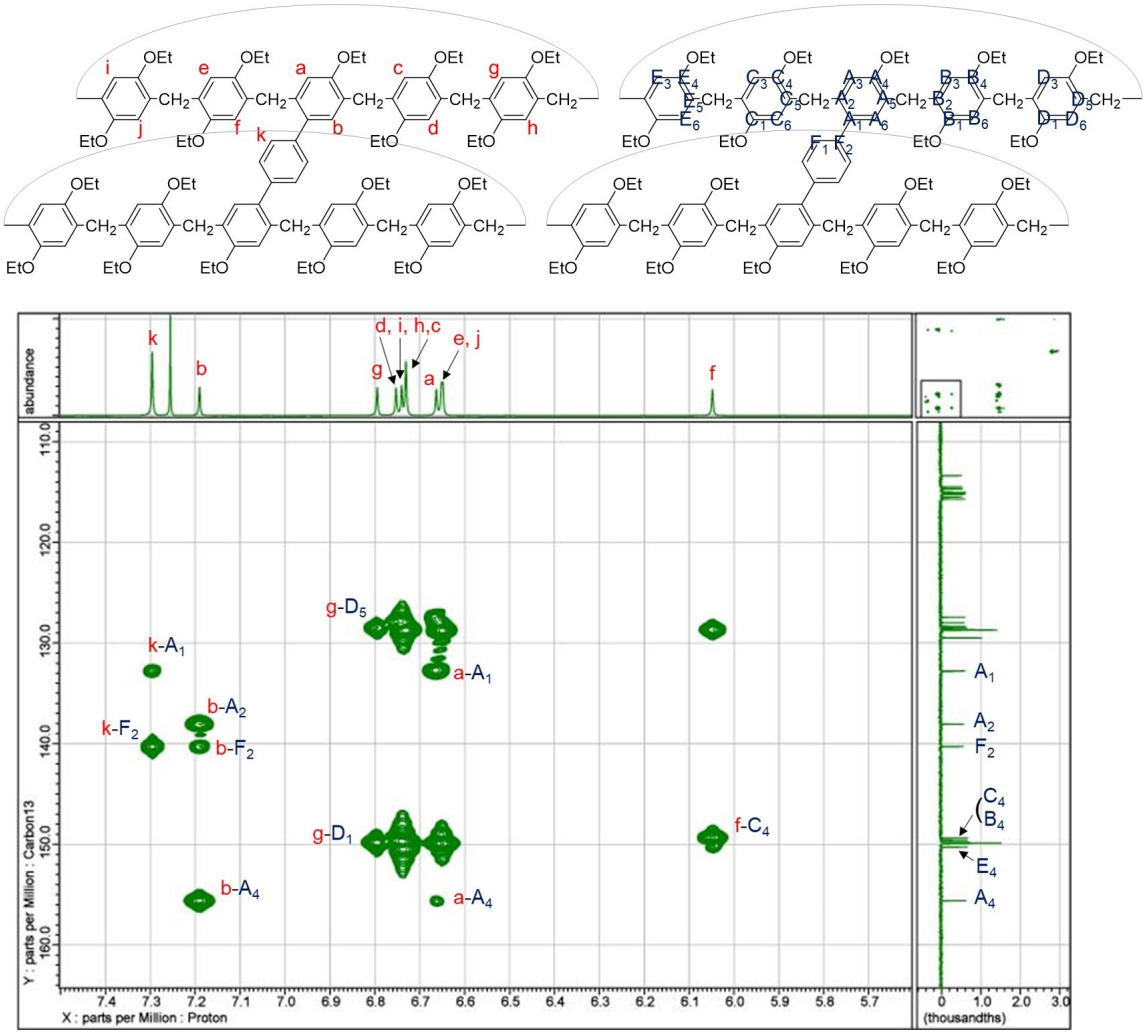

Figure S10. Partial HMBC correlations (500 MHz, $CDCl_3$, 295 K) of **Ph**.

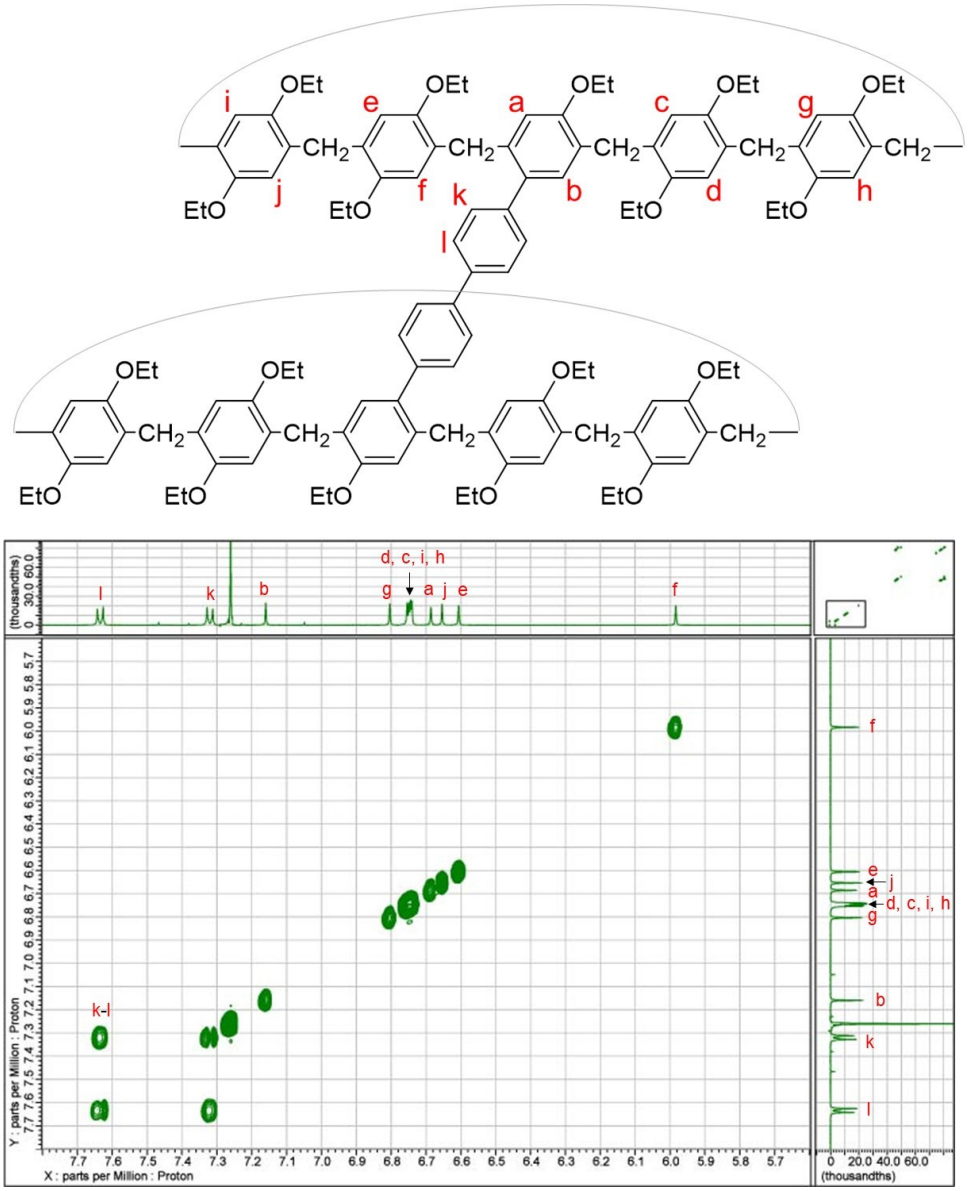

Figure S11. Partial ^{1}H–^{1}H COSY correlations (500 MHz, $CDCl_3$, 295 K) of **BPh**.

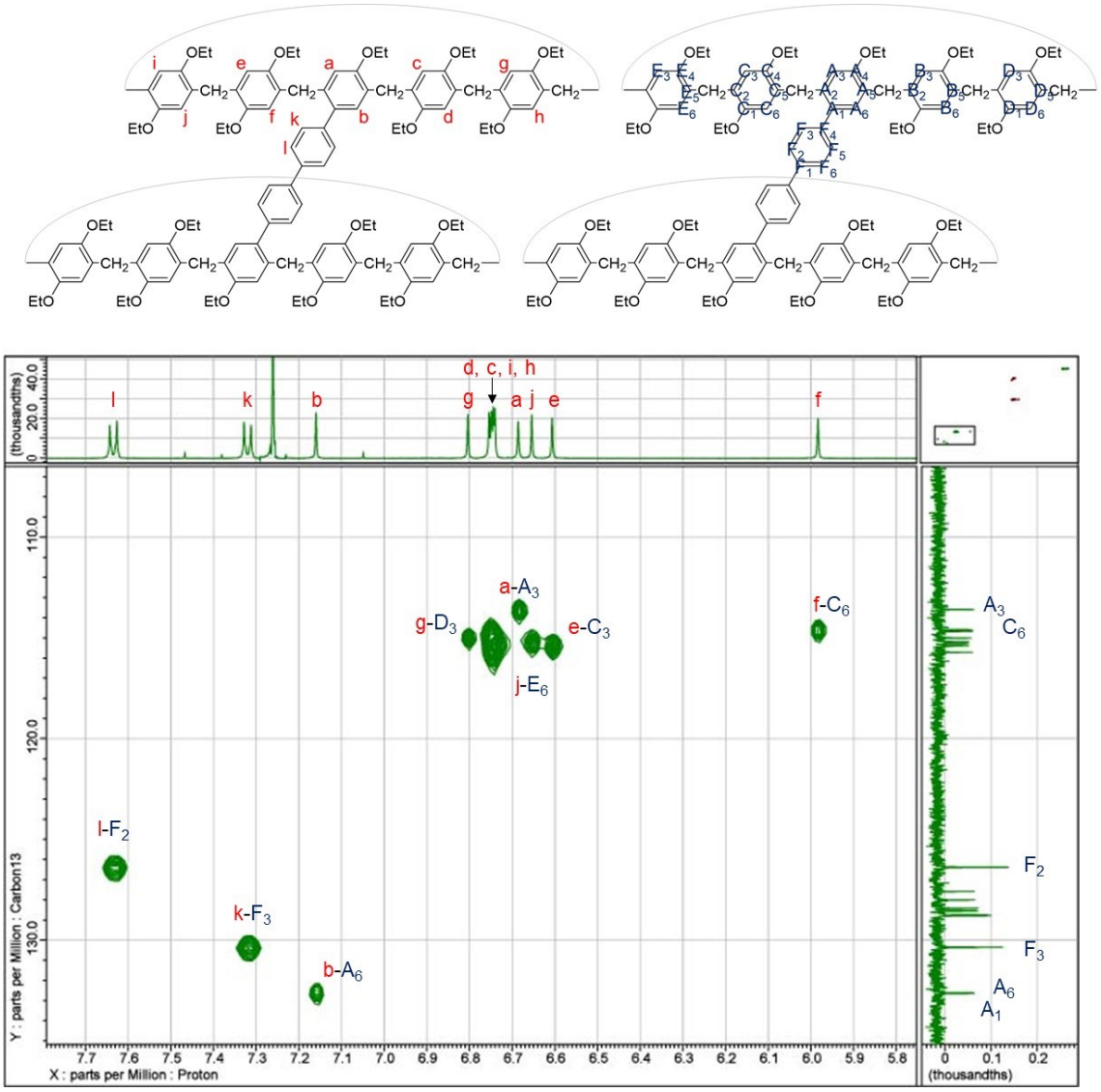

Figure S12. Partial HSQC correlations (500 MHz, $CDCl_3$, 295 K) of **BPh**.

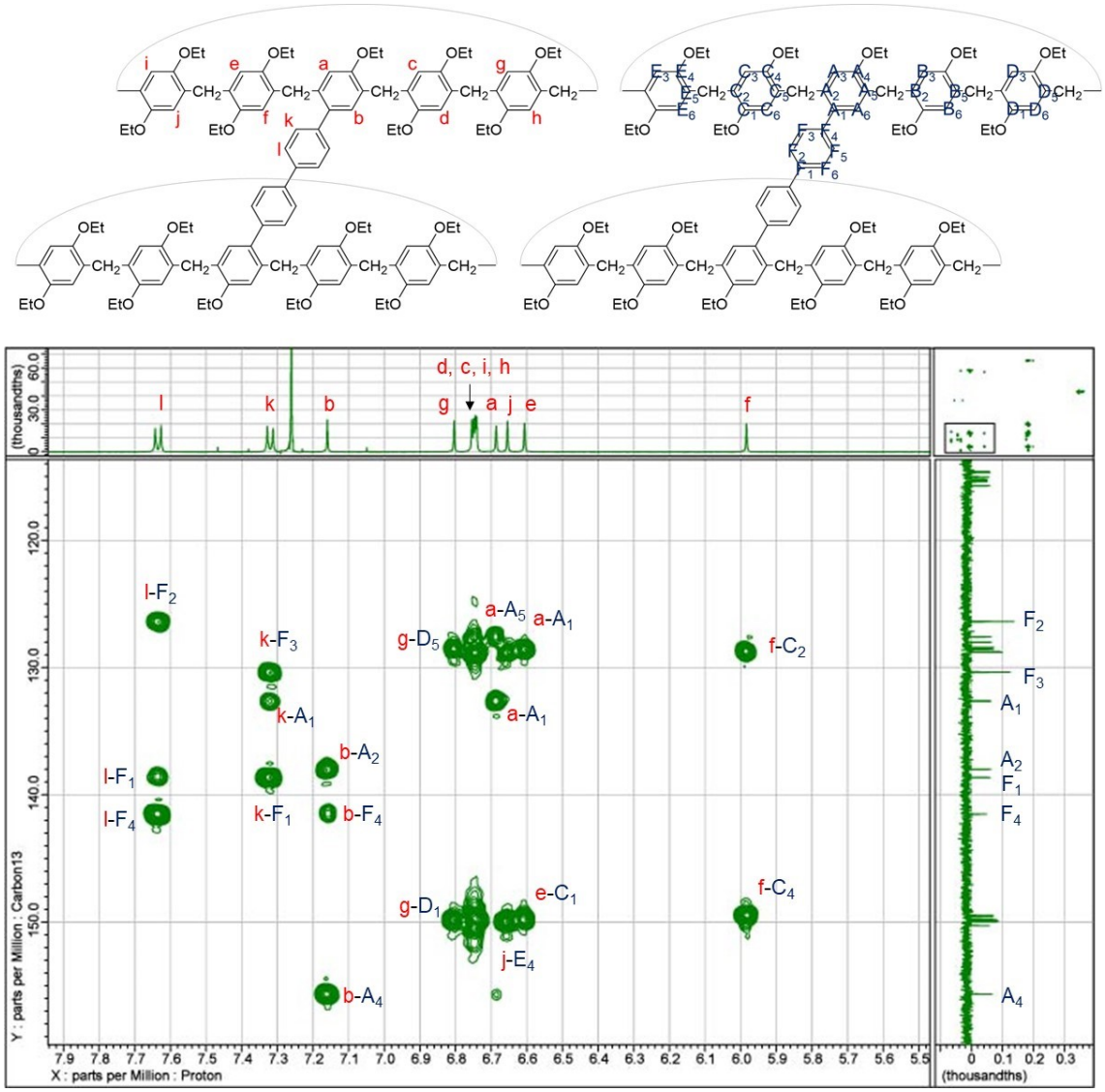

Figure S13. Partial HMBC correlations (500 MHz, $CDCl_3$, 295 K) of **BPh**.

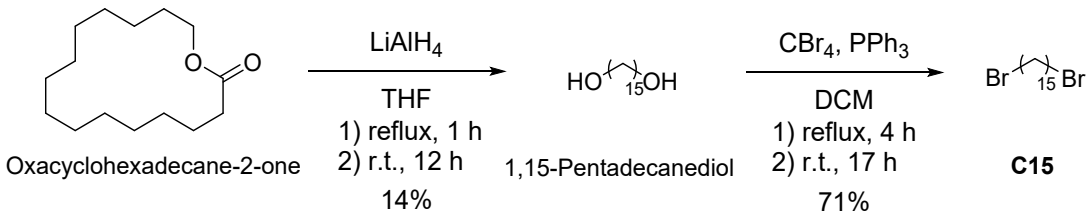

Scheme S4. Synthesis of **C15**.

C15 was synthesized according to the literature[S7] with slight modification. Under nitrogen atmosphere, $LiAlH_4$ (350 mg, 9.25 mmol) was suspended in dry THF (10 mL) at 0 °C. Then, oxacyclohexadecane-2-one (1.0 g, 4.2 mmol) in dry THF (5 mL) was slowly added into the mixture. After refluxing for 1 h, the reaction mixture was stirred at r.t. for 12 h. The reaction was quenched with H_2O and aqueous NaOH solution (2 M). After the insoluble part was filtered out, the filtrate was concentrated on a rotary evaporator. The residue was dissolved into hot ethyl acetate, and then, the insoluble part was filtered out. After removing the solvent, ethyl acetate was added into the residue again, and then, it was recrystallized to afford 1,15-pentadecanediol as a white solid (139 mg, 0.569 mmol, 14%). ^{1}H NMR ($CDCl_3$, 400 MHz, ppm): δ 3.67–3.61 (m, 12H), 1.61–1.53 (m, 4H), 1.39–1.20 (m, 22H). The spectroscopic data was identical to those reported in the literature.[S7]

1,15-Pentadecanediol (100 mg, 0.409 mmol) and CBr_4 (353 mg, 1.06 mmol) were dissolved into dry DCM (7 mL) at 0 °C, and then, PPh_3 (300 mg, 1.14 mmol) was slowly added. The mixture was refluxed for 4 h, and stirred at r.t. for 17 h. After methanol was added, the mixture was stirred for 10 min. The solvent was concentrated on a rotary evaporator. The residue was dissolved into DCM and the organic layer was washed with H_2O and brine. The organic layer was dried over anhydrous Na_2SO_4. After filtration, the filtrate was concentrated on a rotary evaporator. The residue was purified by silica gel column chromatography using DCM as an eluent to give **C15** as a white solid (107 mg, 0.290 mmol, 71%). ^{1}H NMR ($CDCl_3$, 400 MHz, ppm): δ 3.41 (s, 4H), 1.89–1.82 (m, 4H), 1.48–1.21 (m, 22H). The spectroscopic data was identical to those reported in the literature.[S7]

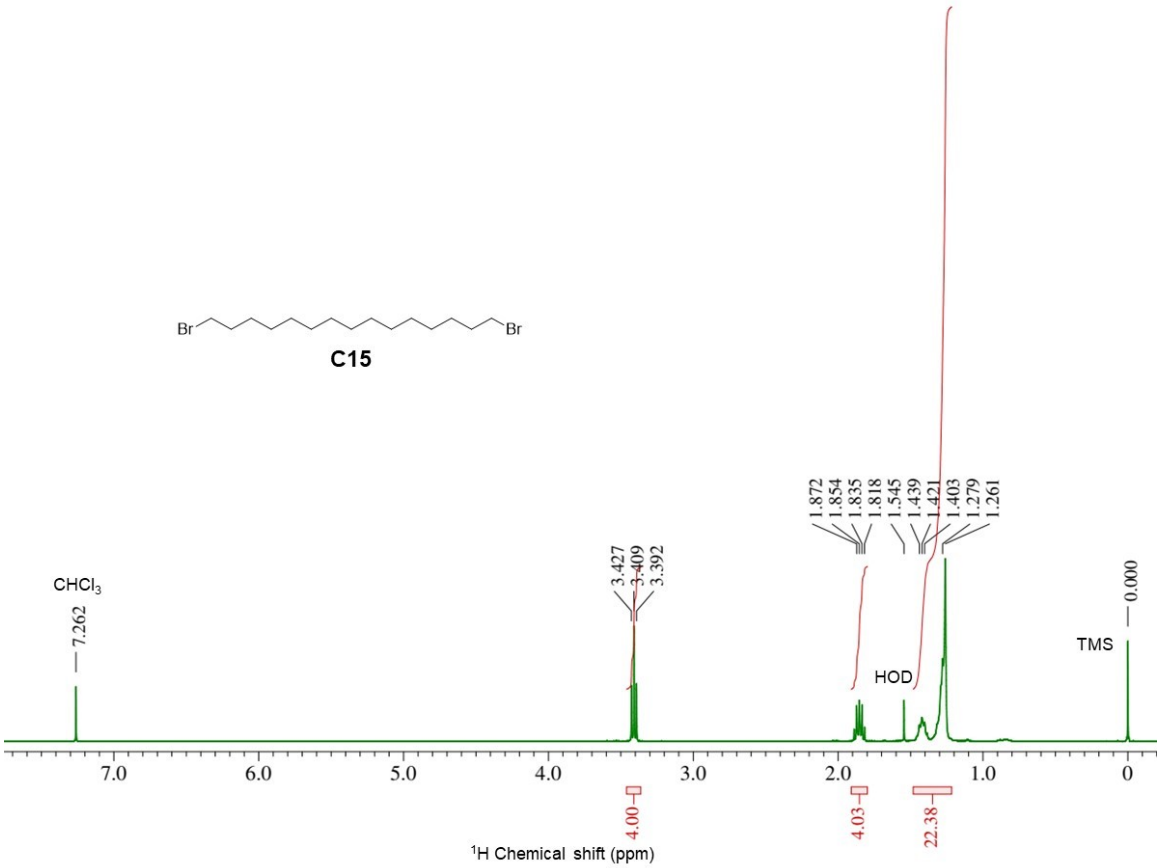

Figure S14. ^{1}H NMR spectrum (400 MHz, $CDCl_3$, 295 K) of **C15**.

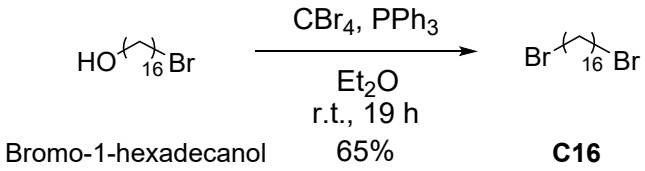

Scheme S5. Synthesis of **C16**.

C16 was synthesized according to the literature[S8] with slight modification. Bromo-1-hexadecanol (200 mg, 0.622 mmol) and CBr_4 (822 mg, 2.48 mmol) were dissolved into dry diethyl ether (6 mL), and then, PPh_3 (919 mg, 3.50 mmol) was slowly added. The mixture was stirred at r.t. for 19 h. After filtration, the filtrate was concentrated on a rotary evaporator. The residue was dissolved into DCM and the organic layer was washed with H_2O and brine. The organic layer was dried over anhydrous Na_2SO_4. After filtration, the filtrate was concentrated on a rotary evaporator. The residue was purified by silica gel column chromatography using DCM as an eluent to give **C16** as white a solid (155 mg, 0.403 mmol, 65%). ^{1}H NMR ($CDCl_3$, 400 MHz, ppm): δ 3.41 (t, 4H), 1.85 (m, 4H), 1.48–1.24 (m, 24H). The spectroscopic data was identical to those reported in the literature.[S8]

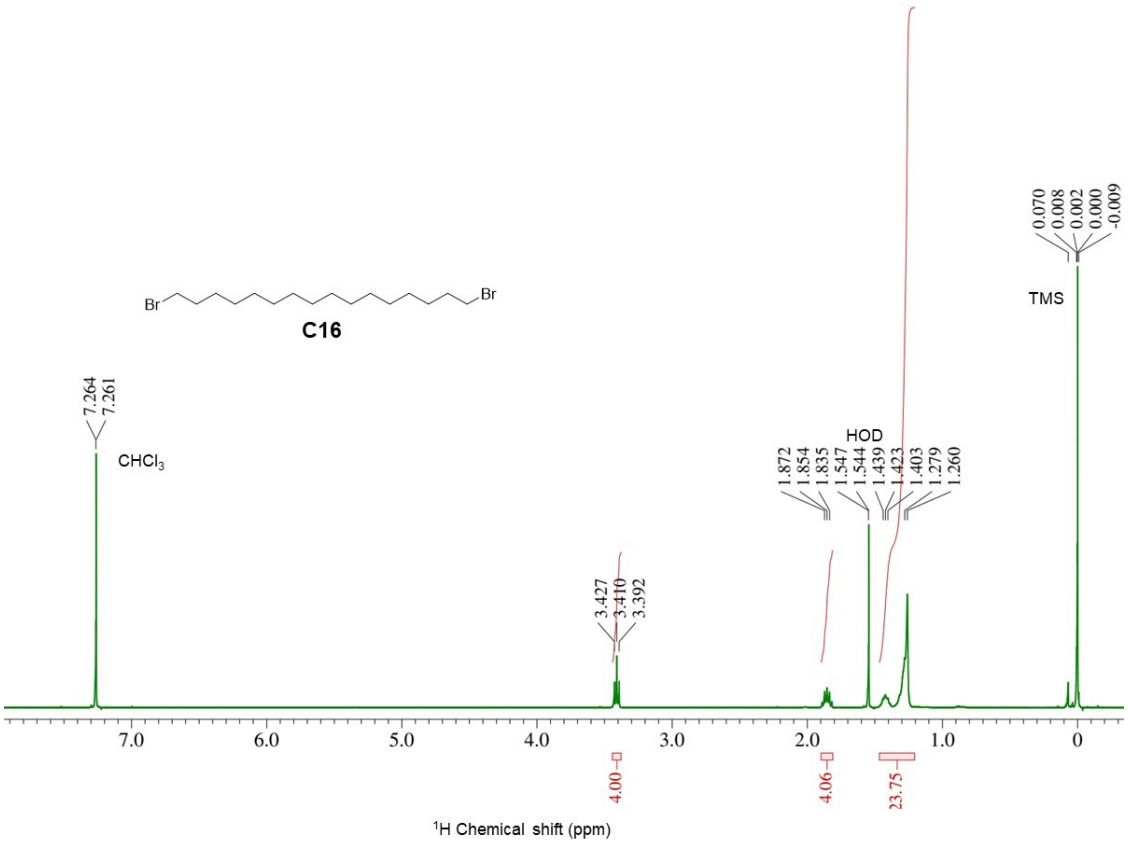

Figure S15. ^{1}H NMR spectrum (400 MHz, $CDCl_3$, 295 K) of **C16**.

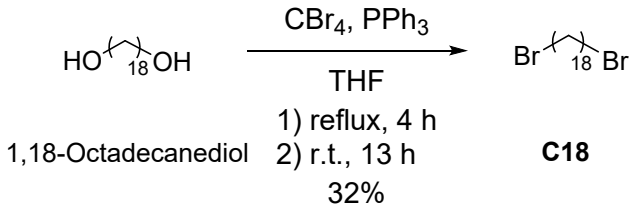

Scheme S6. Synthesis of **C18**.

C18 was synthesized according to the literature[S9] with slight modification. 1,18-Octadecanediol (100 mg, 0.349 mmol) and CBr_4 (290 mg, 0.875 mmol) were dissolved into dry THF (10 mL), and then, PPh_3 (230 mg, 0.878 mmol) was slowly added to the mixture. After refluxing for 4 h, the mixture was stirred for 13 h. After the residue was filtered, the filtrate was concentrated on a rotary evaporator. The residue was dissolved into DCM and the organic layer was washed with H_2O and brine. The organic layer was dried over anhydrous Na_2SO_4. After filtration, the filtrate was concentrated on a rotary evaporator. The residue was purified by silica gel column chromatography using a mixture of *n*-hexane and DCM (1/1, *v*/*v*) as an eluent to give **C18** as a white solid (46 mg, 0.11 mmol, 32%). ^{1}H NMR ($CDCl_3$, 500 MHz, ppm): δ 3.41 (t, 4H), 1.85 (m, 4H), 1.44–1.22 (m, 28H). The spectroscopic data was identical to the literature.[S9]

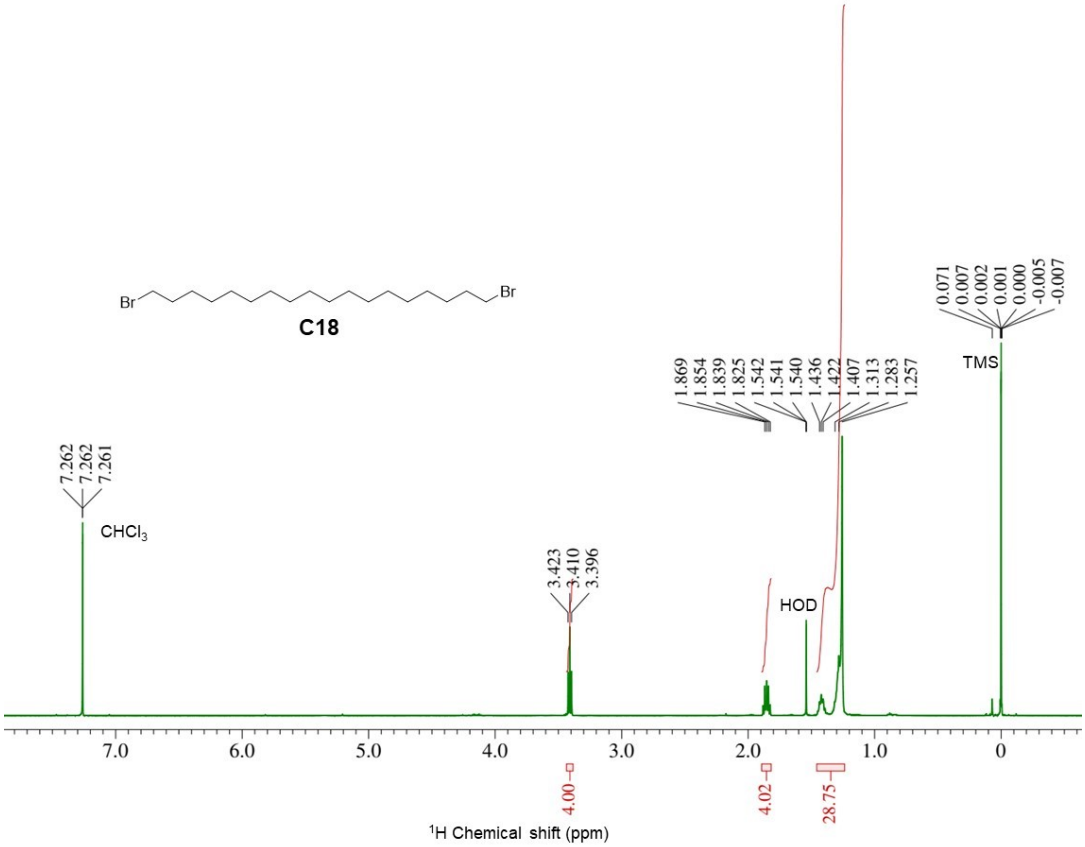

Figure S16. ^{1}H NMR spectrum (400 MHz, $CDCl_3$, 295 K) of **C18**.

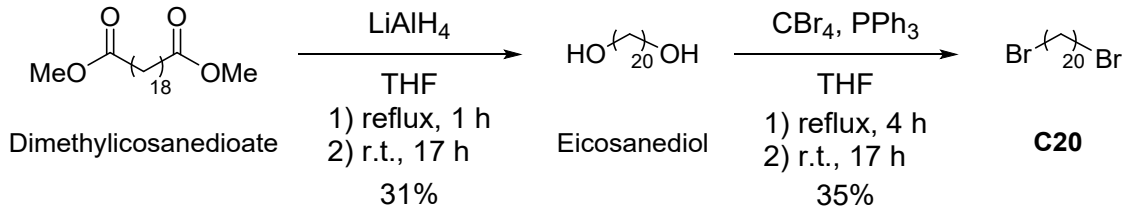

Scheme S7. Synthesis of **C20**.

C20 was synthesized according to the literature[S10,11] with slight modification. Under nitrogen atmosphere, $LiAlH_4$ (256 mg, 6.75 mmol) was suspended in dry THF (30 mL) at 0 °C. Then, 1,20-dimethylicosanedioate (1.0 g, 2.7 mmol) in dry THF (15 mL) was slowly added to the mixture. After refluxing for 1 h, the reaction mixture was stirred at r.t. for 17 h. The reaction was quenched with H_2O and aqueous NaOH solution (2 M). The mixture was filtered and washed with THF. The filtrate was concentrated on a rotary evaporator. The residue was washed with H_2O, then to afford eicosanediol as a white solid (259 mg, 0.823 mmol, 31%). ^{1}H NMR ($CDCl_3$, 600 MHz, ppm): δ 3.82 (s, 4H), 1.59–1.54 (m, 4H), 1.36–1.20 (m, 32H). The spectroscopic data was identical to the literature.[S9]

Eicosanediol (250 mg, 0.795 mmol) and CBr_4 (659 mg, 1.99 mmol) were dissolved into dry THF (15 mL) at 0 °C, and then, PPh_3 (522 mg, 1.99 mmol) was slowly added to the mixture. After refluxing for 4 h, the mixture was stirred at r.t. for 17 h. The residue was filtered. After the filtrate was concentrated on a rotary evaporator, the residue was dissolved into DCM and the organic layer was washed with H_2O and brine. The organic layer was dried over anhydrous Na_2SO_4. After filtration, the filtrate was concentrated on a rotary evaporator. The residue was washed with ethanol and H_2O (2/3, *v*/*v*), then purified by silica gel column chromatography using a mixture of *n*-hexane and DCM (2/1, *v*/*v*) as an eluent to give **C20** as a white solid (122 mg, 0.276 mmol, 35%). ^{1}H NMR ($CDCl_3$, 400 MHz, ppm): δ 3.41 (t, 4H), 1.85 (m, 4H), 1.46–1.21 (m, 32H). The spectroscopic data was identical to the literature.[S9]

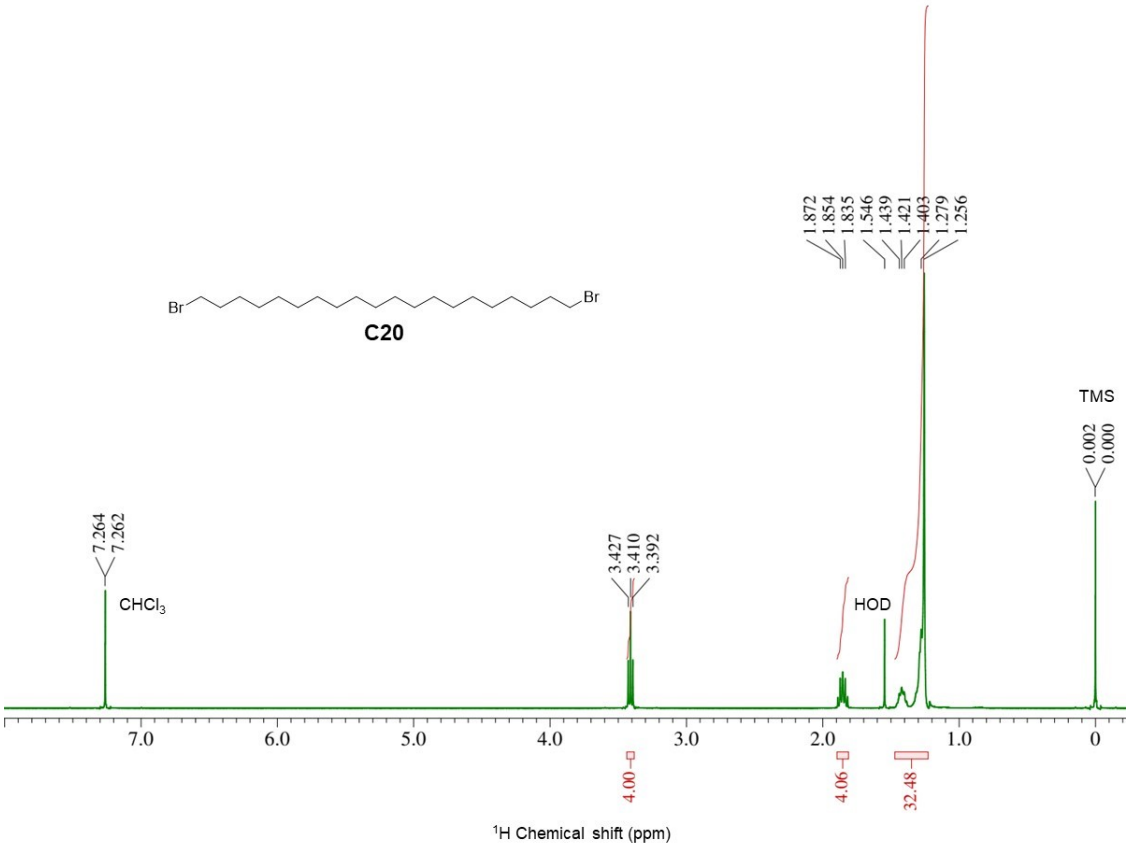

Figure S17. ^{1}H NMR spectrum (400 MHz, $CDCl_3$, 295 K) of **C20**.

Table S1. The association constants and thermodynamic parameters for the host–guest complexation of **1** with **C2**–**C7** ($CDCl_3$, 295 K)

Guest	K_a (M^{-1})
C2	$(6.9\pm0.3)\times10^2$
C3[a]	$(3.0\pm0.2)\times10^2$
C4[a]	$(4.9\pm0.3)\times10^3$
C5[a]	$(1.4\pm0.1)\times10^3$
C6	$(1.9\pm0.1)\times10^3$
C7	$(3.6\pm0.1)\times10^2$

[a]Reported K_as obtained at 298 K.[S12]

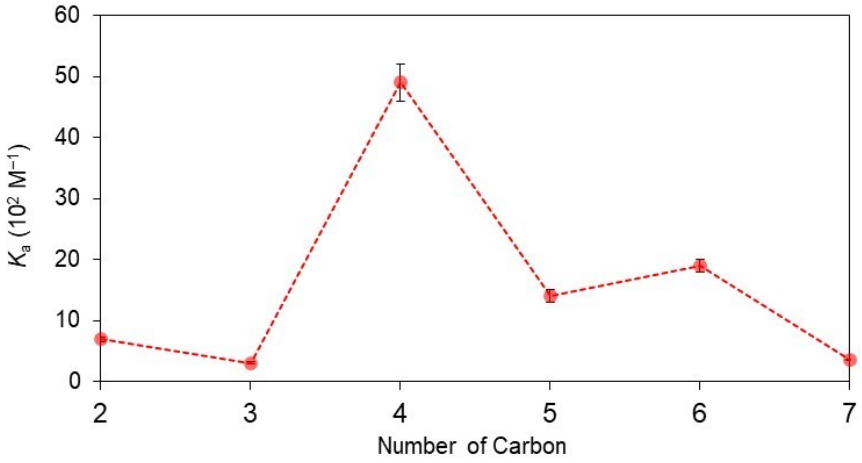

Figure S18. Plot of association constants of **1** ($CDCl_3$, 295 K) for α,ω-dibromoalkanes **C2**–**C7**.

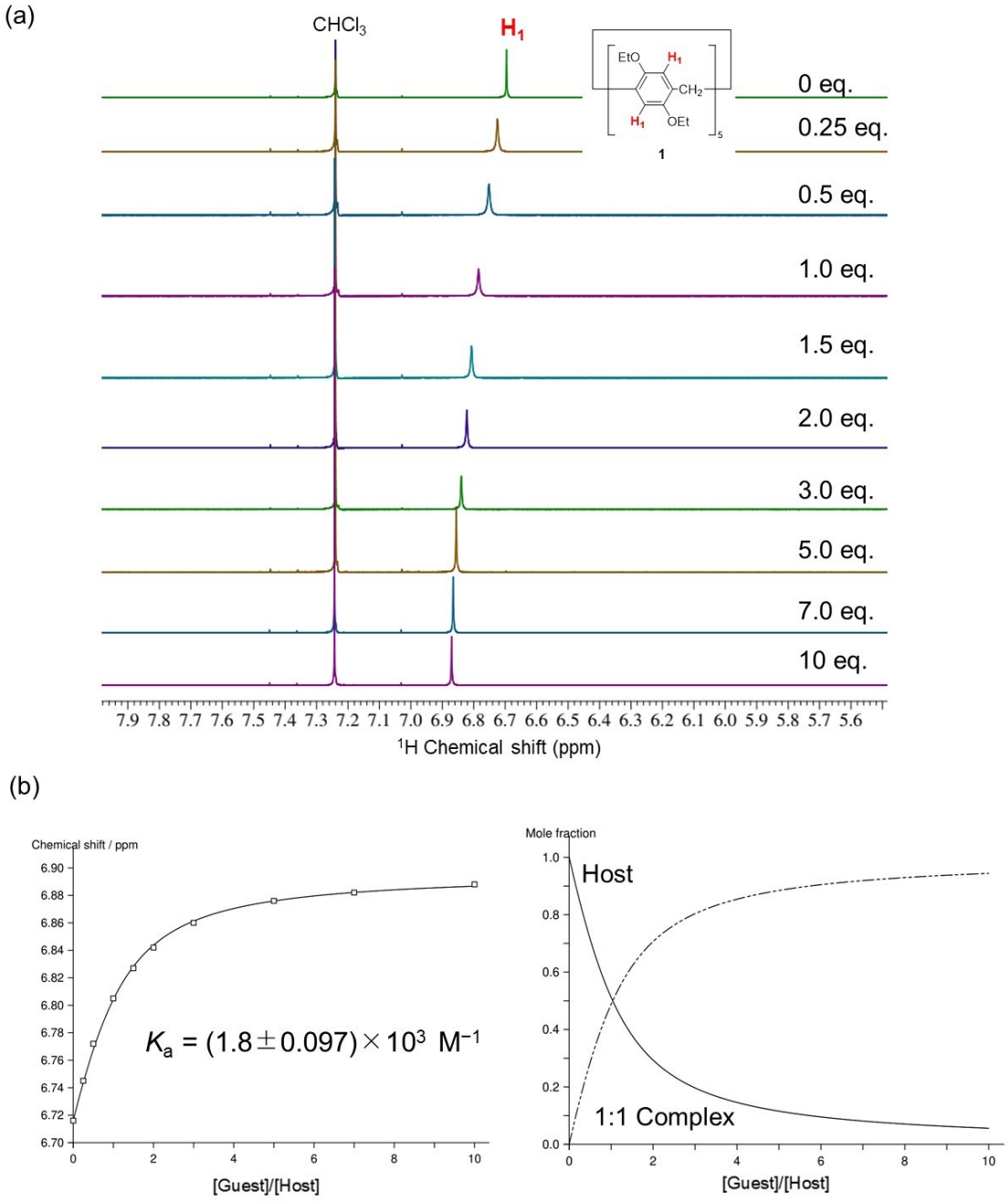

Figure S19. (a) Partial ^{1}H NMR spectra (500 MHz, $CDCl_3$, 295 K) of **1** (1.0 mM) upon addition of **C6** (0–10 eq.). (b) The non-linear curve fitting and the mole fraction of the species for the titration experiment in (a) based on the chemical shift of H_1.

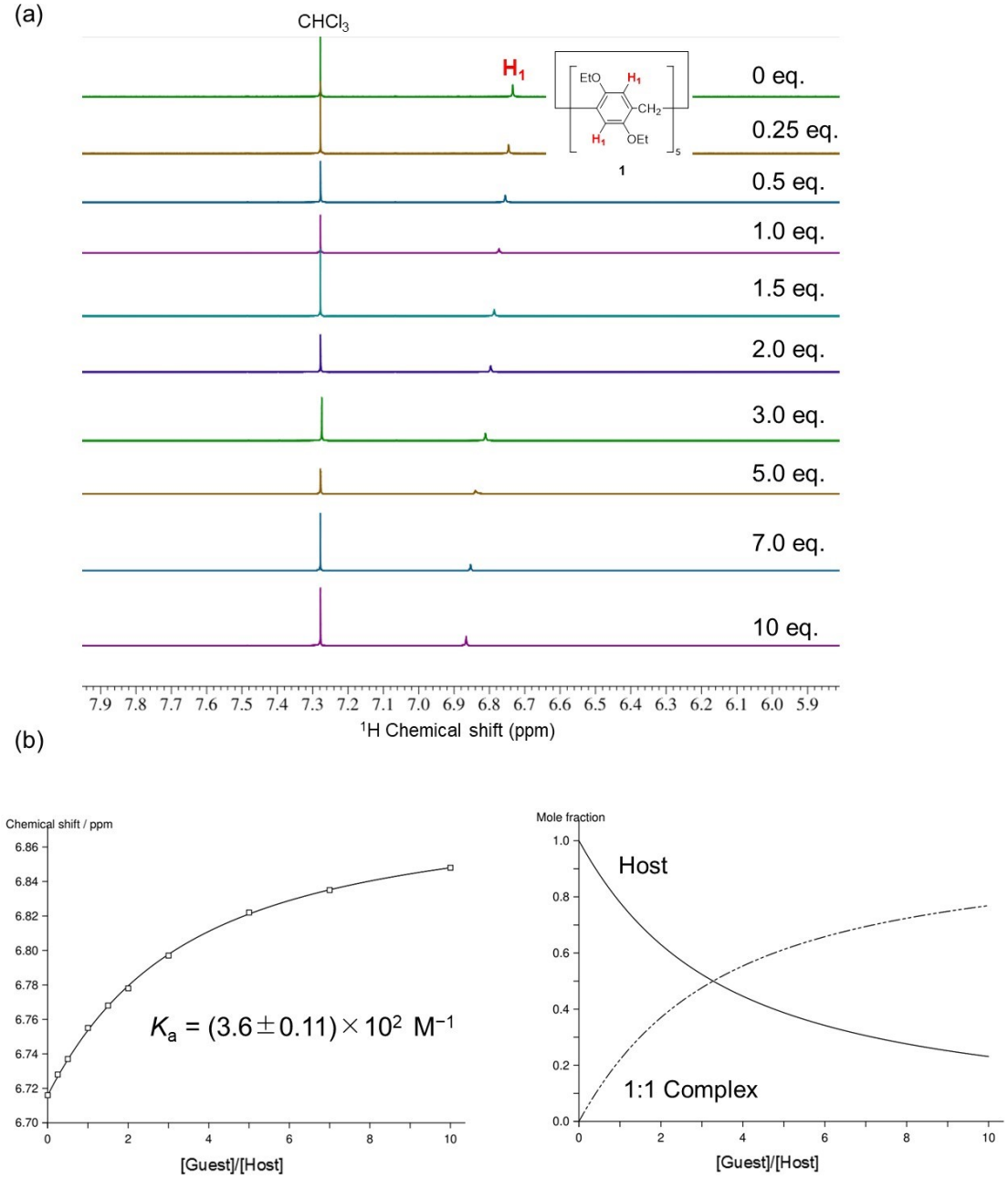

Figure S20. (a) Partial ^{1}H NMR spectra (500 MHz, $CDCl_3$, 295 K) of **1** (1.0 mM) upon addition of **C7** (0–10 eq.). (b) The non-linear curve fitting and the mole fraction of the species for the titration experiment in (a) based on the chemical shift of H_1.

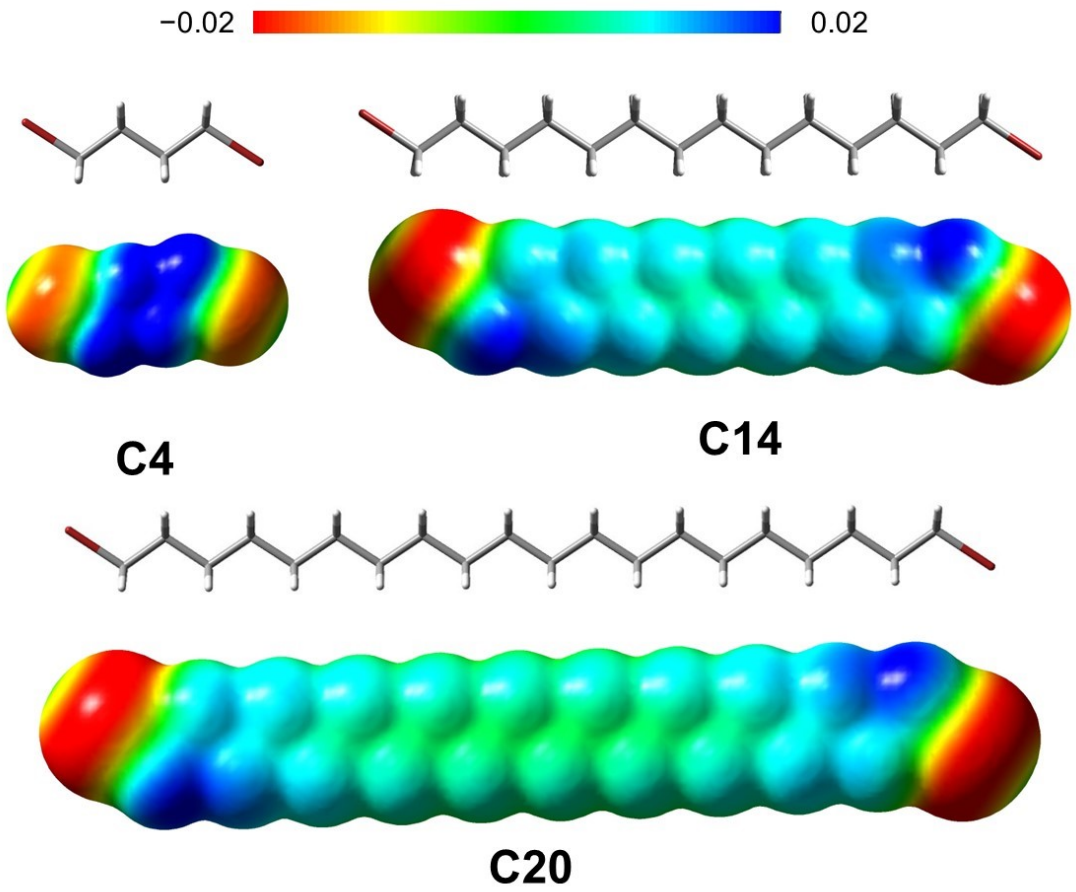

Figure S21. Electrostatic potential maps of **C4**, **C14** and **C20** (DFT calculation at the M06-2X/6-31G(d,p) level of theory).

Table S2. Crystallographic data and structural refinements for **Ph** and **BPh**

Compounds	**Ph**	**BPh**
Formula	$C_{112}H_{134}O_{18}$+2(C_6H_{14})	$C_{118}H_{138}O_{18}$+2(C_6H_{14})
Solvent	toluene/*n*-hexane	$CHCl_3$/*n*-hexane
MW	1768.29	1844.38
T/K	143	143
Crystal system	triclinic	monoclinic
Space group	*P*-1	$P2_1/n$
a/Å	12.062(5)	12.587(9)
b/Å	21.595(9)	20.924(14)
c/Å	23.1024(10)	22.900(15)
α/°	95.788(7)	90
β/°	92.174(7)	90.935(10)
γ/°	99.902(8)	90
V/Å^3	5888(3)	6030.38
Z	2	2
ρ/g cm^{-3}	1.118	1.111
R_1	0.1395	0.1200
wR_2	0.3702	0.2819
GOF	1.052	1.157
F(000)	2146	2180
Crystal size/mm^3	0.40× 0.10× 0.05	0.30 × 0.30× 0.21
θ range for data collection/°	3.007–27.530	3.053–27.411
Index ranges	−13 ≤ *h* ≤ 15, −28 ≤ *k* ≤ 28, −27 ≤ *l* ≤ 30	−16 ≤ *h* ≤ 13, −27 ≤ *k* ≤ 27, −28 ≤ *l* ≤ 29
CCDC number	2409580	2409578

Ph:

PROBLEM: PLAT910_ALERT_3_B Missing # of FCF Reflection(s) Below Theta(Min). 38 Note

RESPONSE: The unit cell is reasonable large and these low angle reflections are probably missing due to the beamstop.

BPh:

PROBLEM: PLAT910_ALERT_3_B Missing # of FCF Reflection(s) Below Theta(Min). 17 Note

RESPONSE: The unit cell is reasonable large and these low angle reflections are probably missing due to the beamstop.

ESI Note 1

At r.t., the two conformations (*connected* and *unconnected* conformations) rapidly interconvert each other through the rotation or flipping of the benzene rings in the solutions. No defined conformers were observed in ^{1}H NMR spectrum of **BPh** at 293 K, whereas H_f proton peak of **BPh** was split into two at 193 K (Figure S22), suggesting the possibility of the coexistence of *connected* and *unconnected* conformations at low temperature due to the restriction of the molecular motions. On the other hand, no peak splitting was observed for H_f of **Ph** even at 193 K (Figure S23). This is probably because the equilibrium biased into *unconnected* conformation due to the steric repulsion in the *connected* conformation of **Ph**.

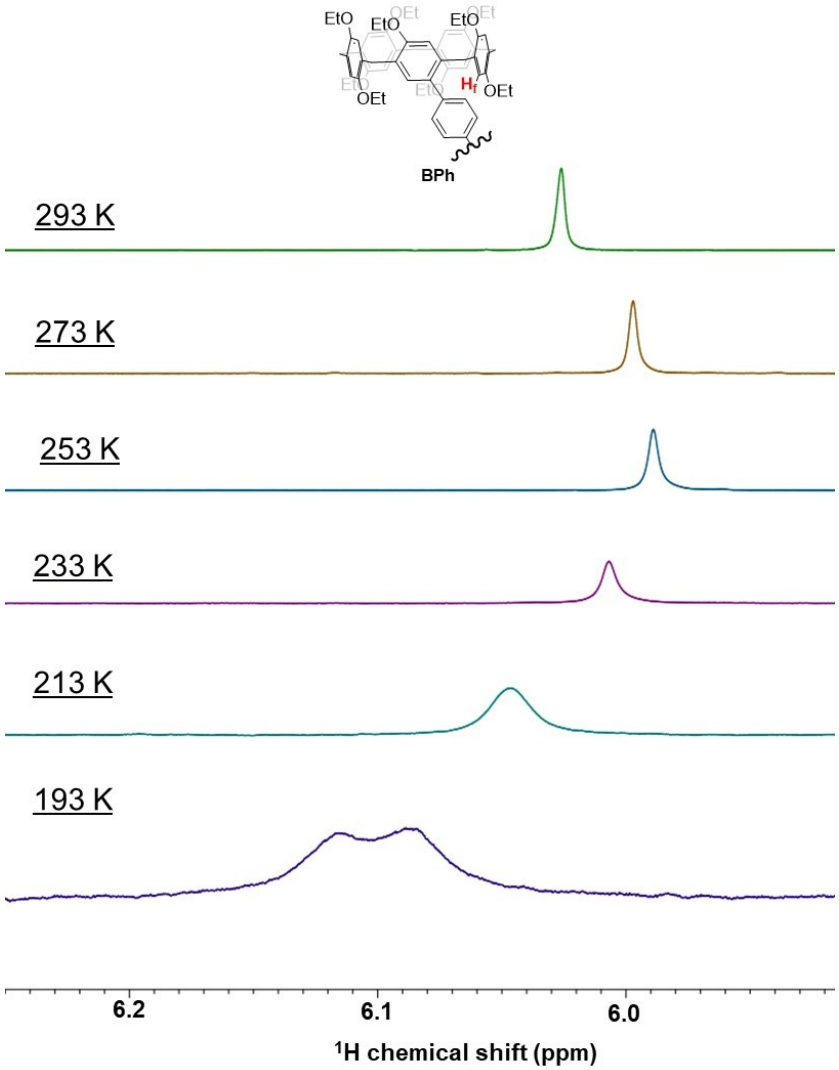

Figure S22. Partial variable-temperature ^{1}H NMR spectra (toluene-d_8, 500 MHz) of **BPh**.

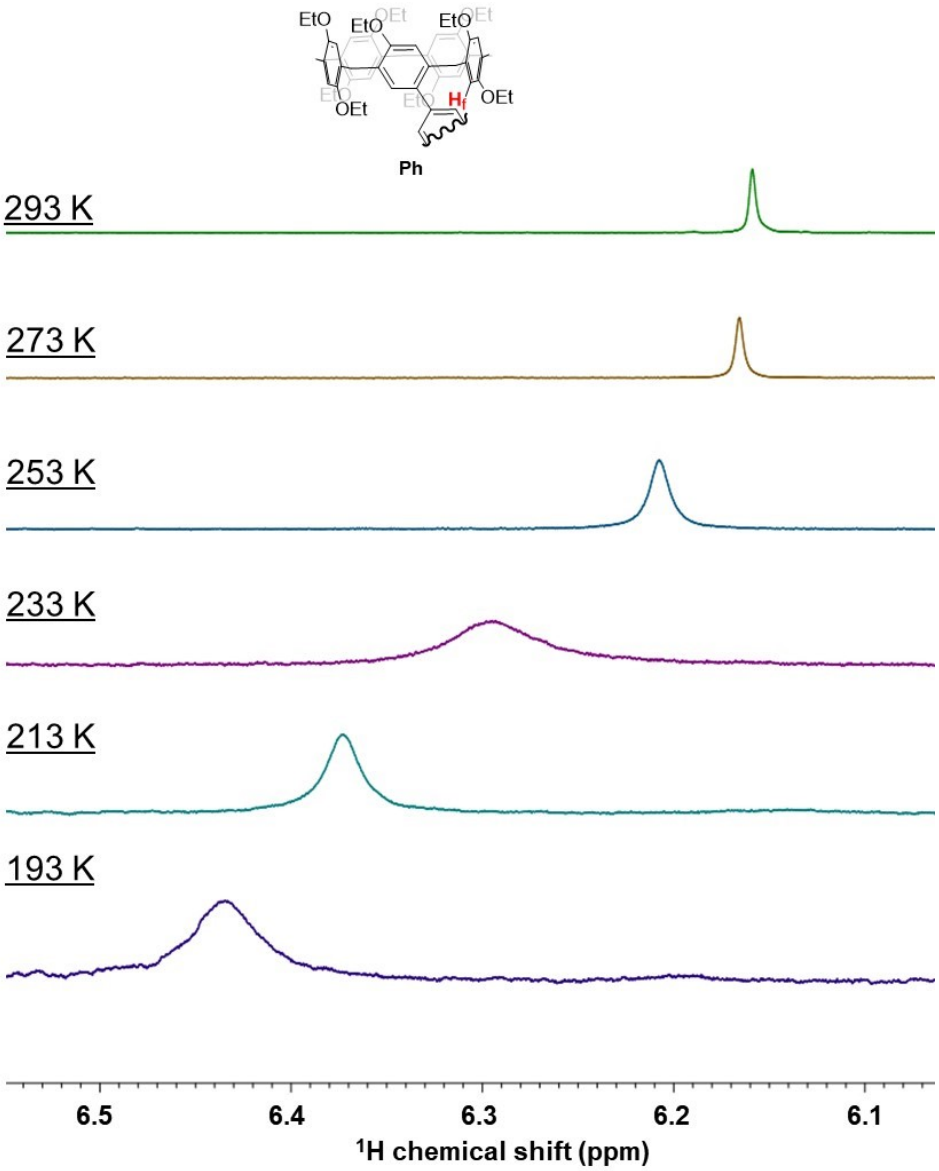

Figure S23. Partial variable-temperature ^{1}H NMR spectra (toluene-d_8, 500 MHz) of **Ph**.

ESI Note 2

While **Ph** is a heterochiral dimer, **BPh** molecules exist as either all-*pR* or all-*pS* homochiral dimers in the crystals. The unit cell of **BPh** consists of two all-*pR* and two all-*pS* homochiral dimers, forming racemic crystals (Figure S24). The orientations of all alkoxybenzenes in each cavity must align to minimize steric hindrance from the linkers. When the two cavities are located on opposite sides, this alingment effect results in the heterochiral configuration of **Ph** (Figure S25a). Conversely, when the cavities are on the same side, **BPh** acts as homochiral dimer(Figure S25b).

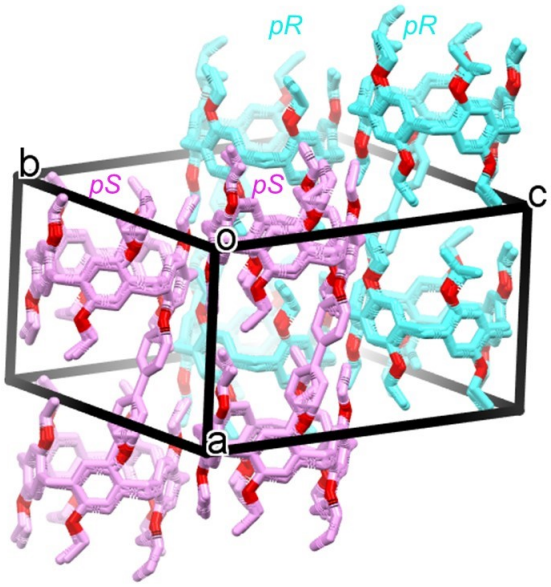

Figure S24. Packing structure of **BPh** and the unit cell consisting of two all-*pR* and two all-*pS* homochiral dimers. The static disorder structures are also visualized.

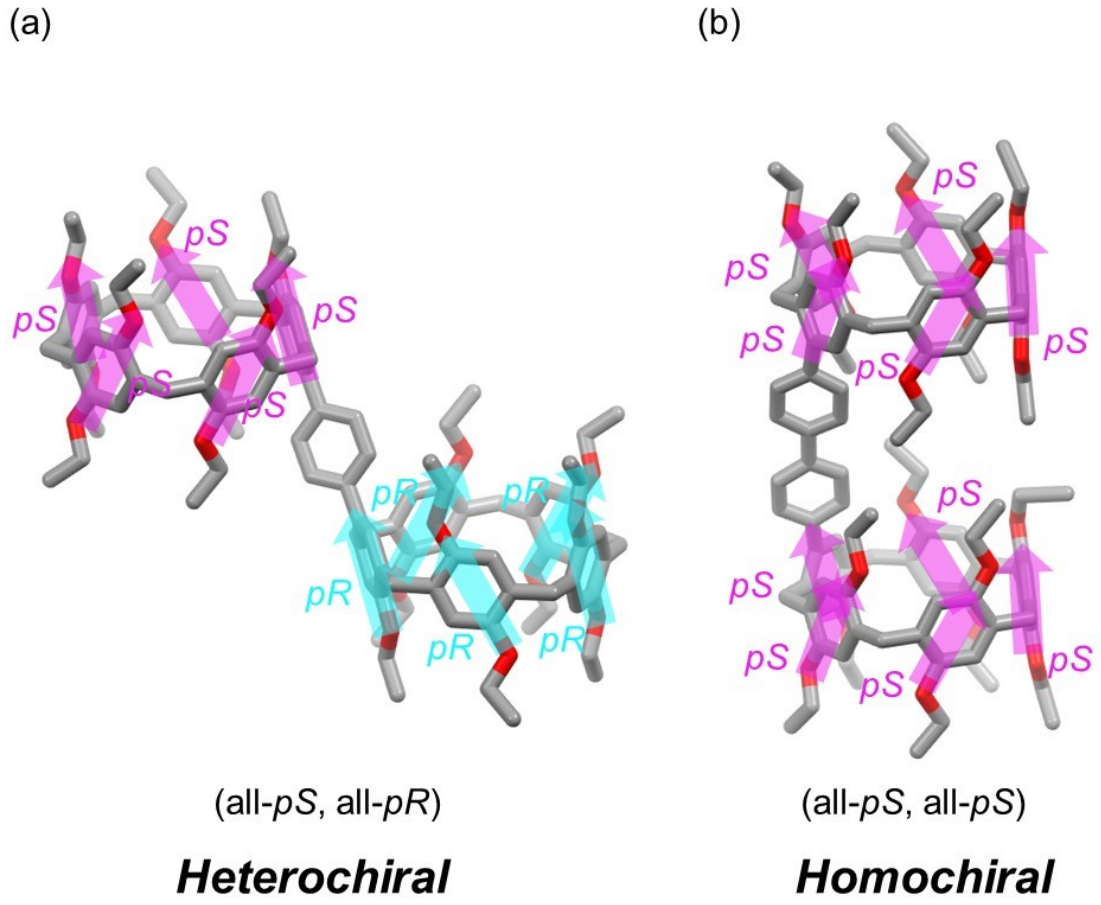

Figure S25. Single crystal structures of (a) **Ph** and (b) **BPh** illustrating the planar chirality of pillar[5]arene cavities.

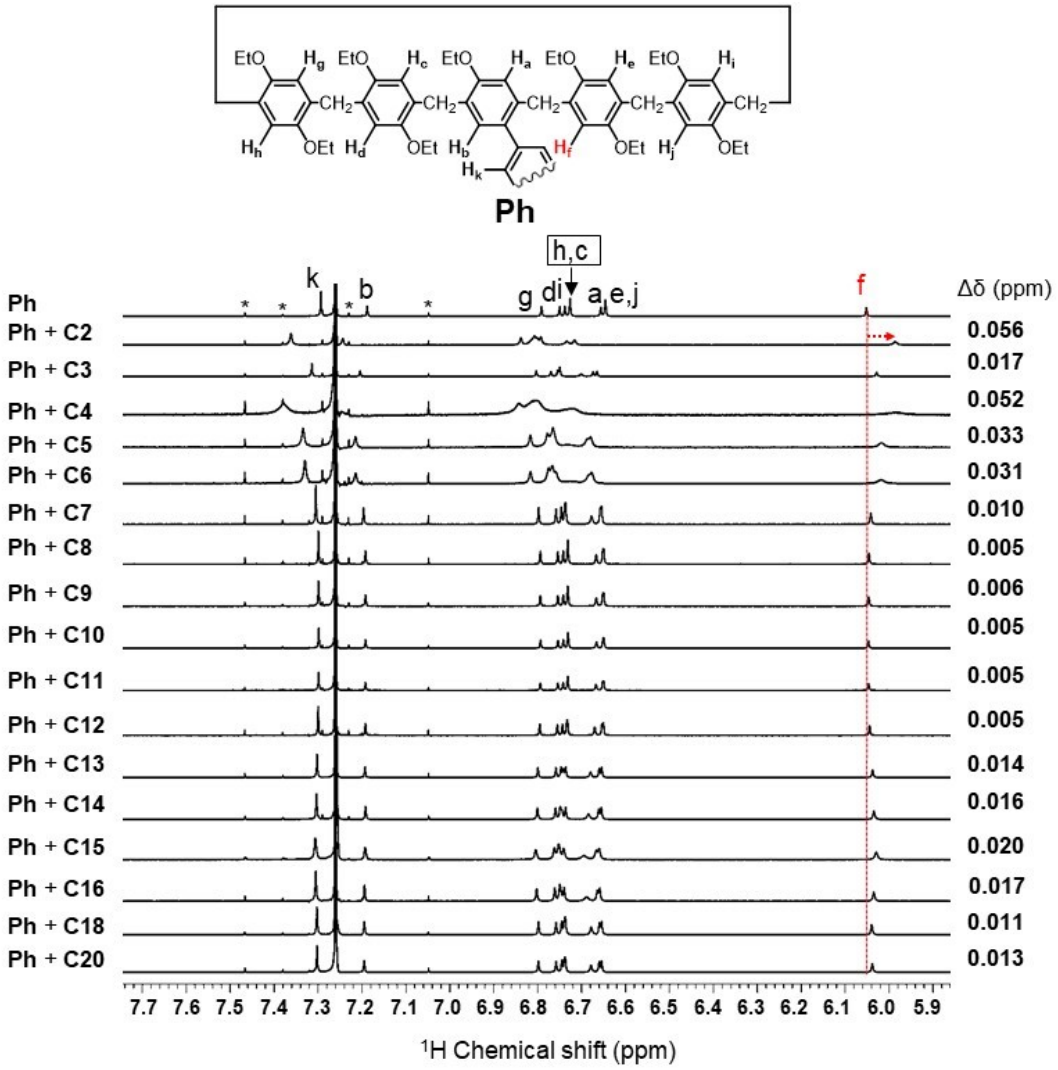

Figure S26. ^{1}H NMR spectra (500 MHz, $CDCl_3$, 295 K) of **Ph** (0.50 mM) with **C2**–**C16**, **C18** and **C20** (0.50 mM). Asterisks mean spinning sidebands or ^{13}C satellites of chloroform peak.

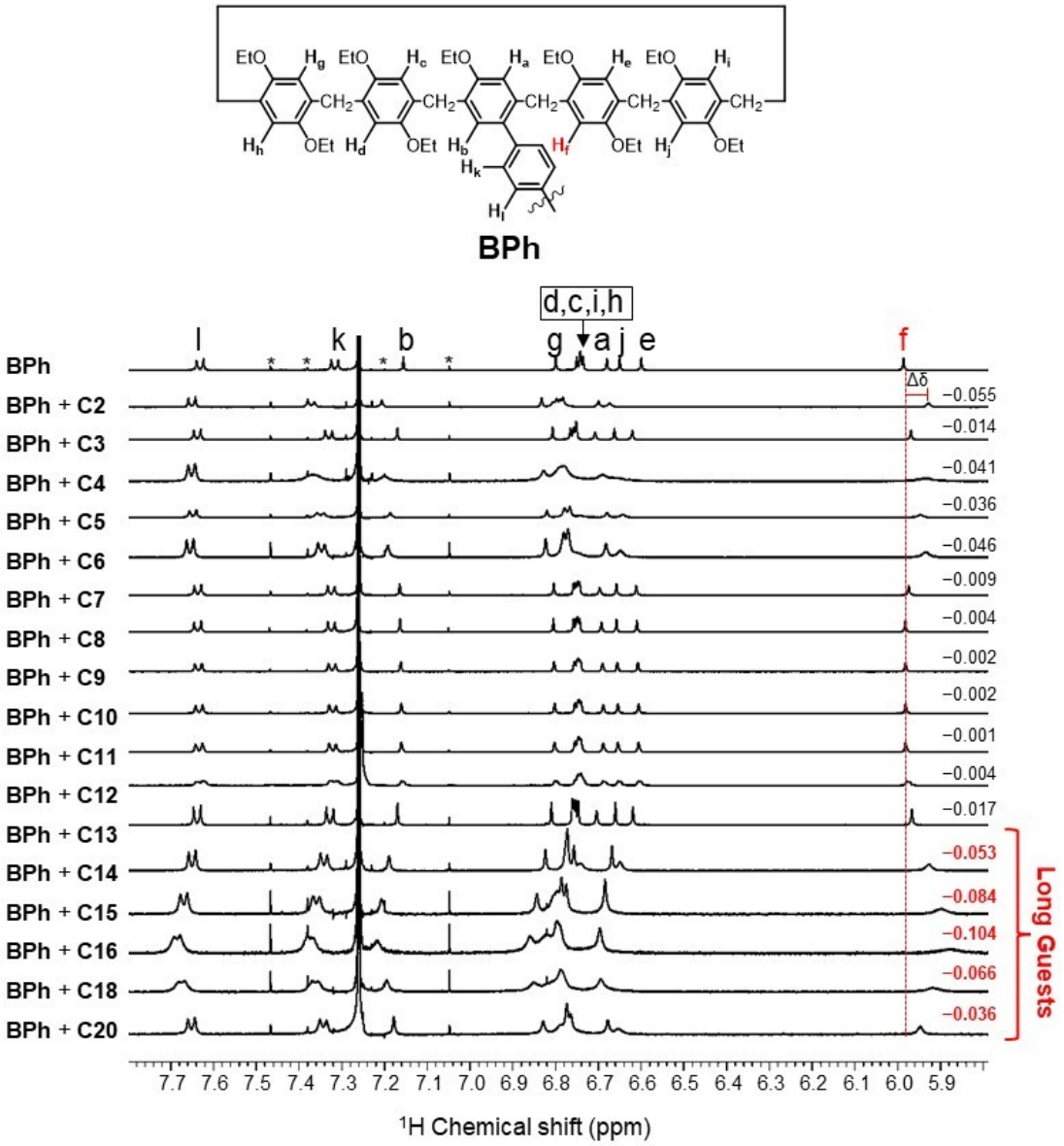

Figure S27. ^{1}H NMR spectra (500 MHz, $CDCl_3$, 295 K) of **BPh** (0.50 mM) with **C2**–**C16**, **C18** and **C20** (0.50 mM). Asterisks mean spinning sidebands or ^{13}C satellites of chloroform peak.

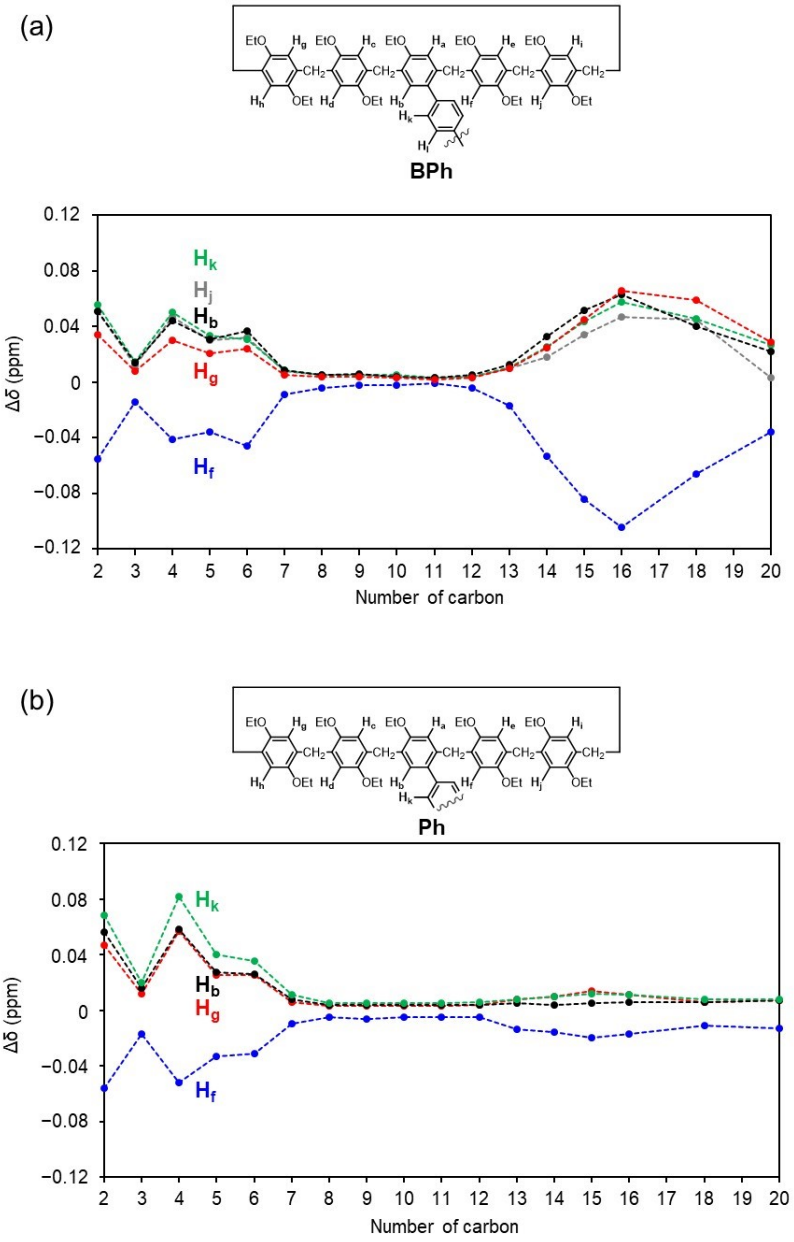

Figure S28. Plots of chemical-shift changes (Δδs) for the aromatic protons of (a) **BPh** and (b) **Ph** (0.50 mM) with 1.0 eq. of α,ω-dibromoalkanes (**C2**–**C16**, **C18**, and **C20**).

ESI Note 3

Guest selection

To understand the host–guest properties of **1**, **Ph**, and **BPh**, we selected *α*,*ω*-dibromoalkanes as guest molecules because a wide range of chain lengths are commercially available, allowing for a systematic investigation of chain-length-dependent binding behavior. In contrast, other halogenated alkanes and alkene derivatives are only available for limited chain lengths, and some have not been reported or are difficult to synthesize. For another choice, we selected alkane diols because they are also commercially available. We examined the host–guest behavior of **BPh** toward alkane-α,ω-diols with chain lengths of C2 and C14 (**C2OH** and **C14OH**, respectively). However, the observed peak shifts were too small to accurately determine the association constants (Figures S29 and S30). Therefore, we used *α*,*ω*-dibromoalkanes for the systematic investigation of chain-length-dependent binding behavior.

Chain-length-dependent bindings of **1**, **Ph** and **BPh**

We determined the association constants (K_a) of short (**C2**) and long (**C14**) guests with **1**, **Ph**, and **BPh** (Figures S31–S36). In the case of the short guest (**C2**), the K_as of **Ph** and **BPh** were either comparable to or lower than that of **1** (Table S3). Considering that **Ph** and **BPh** have two cavities, the dimers should statistically exhibit a larger binding constant. The decreased host–guest complexation ability of the dimers can be explained by steric hindrance from its rigid linker moieties, which reduces the cavity size of pillar[5]arene. Furthermore, the close proximity of the two cavities might hinder host–guest complexation with shorter guests because **BPh** can adopt a *connected* conformation. In contrast, the reversed trend was observed for K_as for long guest (**C14**); K_as of **1** and **Ph** for **C14** guest were also almost the same, whereas the K_a of **BPh** increased. These results support that **BPh** cooperatively binds one **C14** guest in the *connected* conformation.

The stoichiometries of the complexes between dimers and **C2** and **C14** guests were determined to be 1:1 by Job's plots (Figure S37). However, given the relatively large binding constant of **Ph** for **C2** ($(6.9\pm0.6)\times10^2$ M^{-1}), a second binding event was expected to occur, which might be undetectable due to the detection limit of Job's plots.[S13] To confirm that, we performed an additional titration experiment of **Ph** and **BPh** with 1,2-dicyanoethane. The host–guest complexation of pillar[5]arene with 1,2-dicyanoethane exhibited slow chemical exchange on the NMR time scale. In ^{1}H NMR titration spectra, the peak of phenyl group was divided into three peaks upon the addition of 1,2-dicyanoethane, suggesting the formation of 1:2 complex in addition to free host and 1:1 complex (Figure S38). In contrast, the peak of **BPh** was divided into two peaks, suggesting that the formation of only 1:1 complex. This can be also explained by the *connected* conformation of **BPh**; the steric hindrance from an already included guest may prevent the host–guest complexation within another cavity.

Alkyl-linked pillar[5]arene dimer

We performed geometry optimization of the ethyl-linked pillar[5]arene dimer (**Et**), which contains a flexible ethyl linker with the same host–host distance as that in the phenyl-linked dimer (**Ph**). For comparison, we optimized the host–guest complexes of **Et** and **Ph** with the **C12** guest (Figure S39). However, significant steric hindrance was observed for both **C12**@**Et** and **C12**@**Ph**, as indicated by the outward bending of some ethoxy groups (Figure S39). Given that **Ph** could not adopt the *connected* conformation due to steric hindrance between the two cavities, **Et** is expected to behave similarly, even though it possesses a more flexible ethyl linker. These results suggest that the short host–host distance, rather than linker rigidity, is the dominant factor preventing the formation of the *connected* conformation.

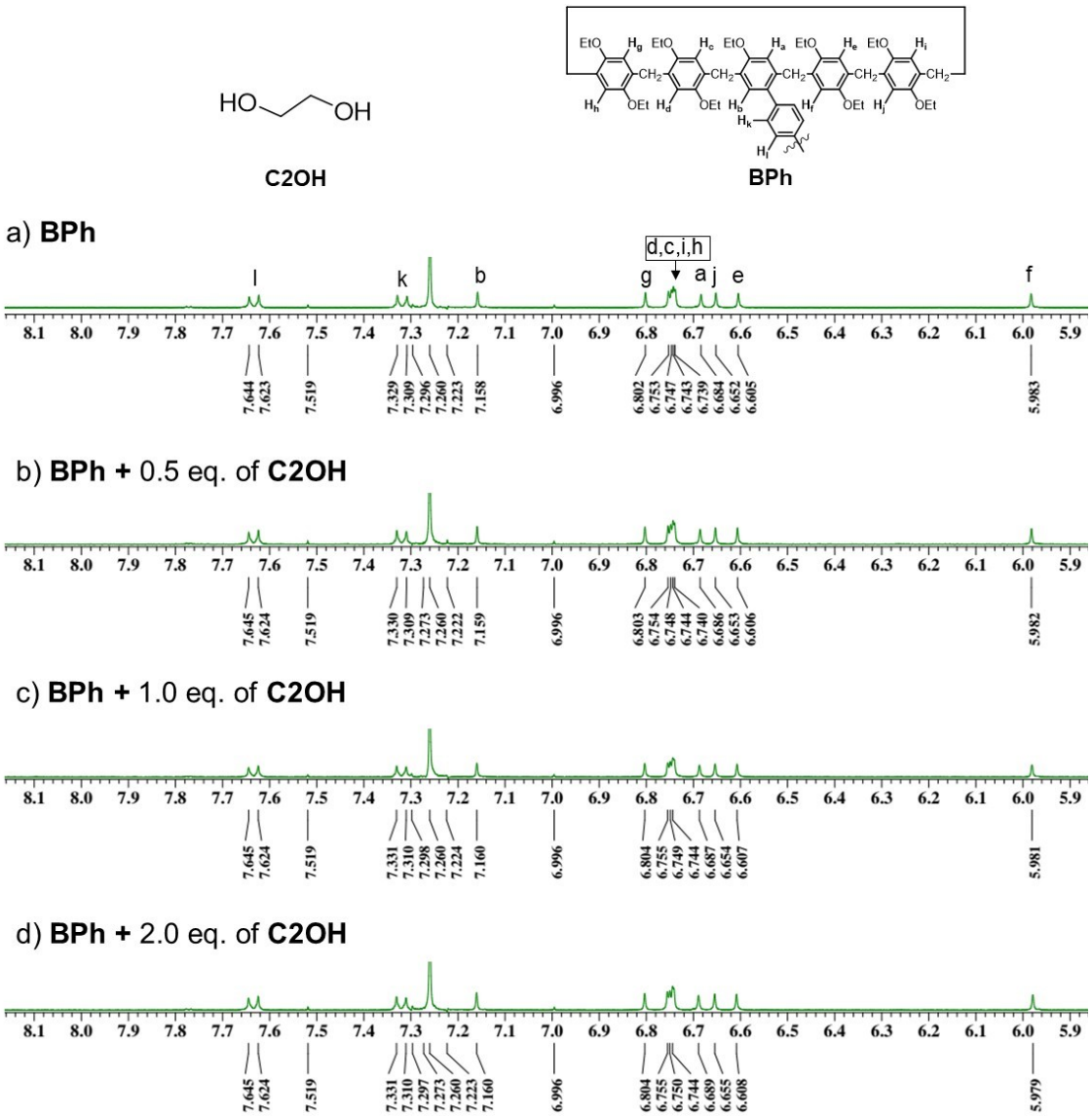

Figure S29. Partial ^{1}H NMR spectra (400 MHz, $CDCl_3$, 295 K) of **BPh** (1.0 mM) upon addition of **C2OH** (0–2.0 eq.).

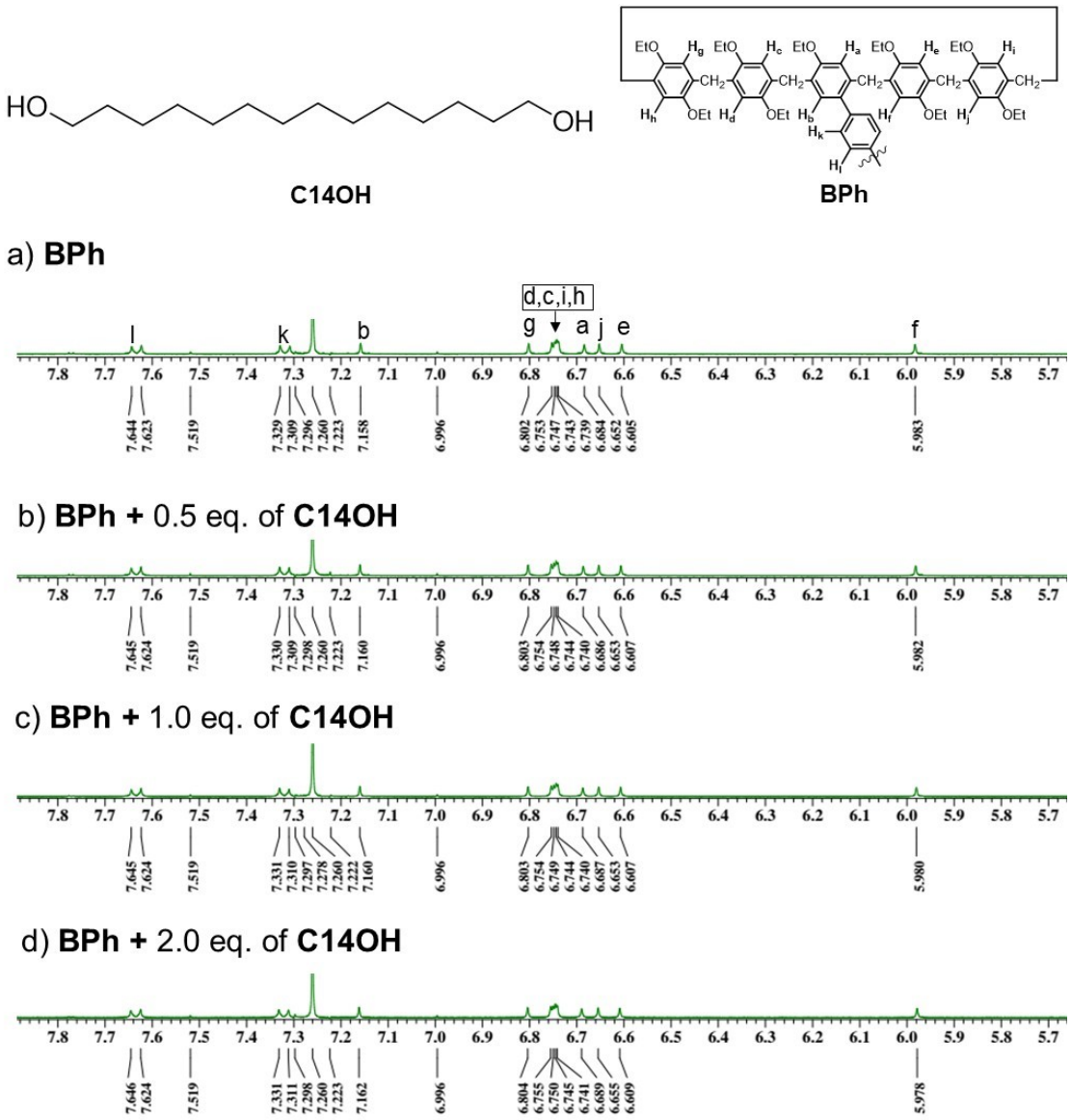

Figure S30. Partial ^{1}H NMR spectra (400 MHz, $CDCl_3$, 295 K) of **BPh** (1.0 mM) upon addition of **C14OH** (0–2.0 eq.).

Table S3. The association constants K_as (M^{-1}) of **1**, **Ph**, and **BPh** with **C2** and **C14** (1.0 mM, $CDCl_3$, 295 K)

	1	**Ph**	**BPh**
C2	$(6.9\pm0.3)\times10^2$	$(6.9\pm0.6)\times10^2$	$(3.0\pm0.2)\times10^2$
C14	$(9.6\pm0.13)\times10^1$	$(1.6\pm0.0)\times10^2$	$(4.4\pm0.3)\times10^2$

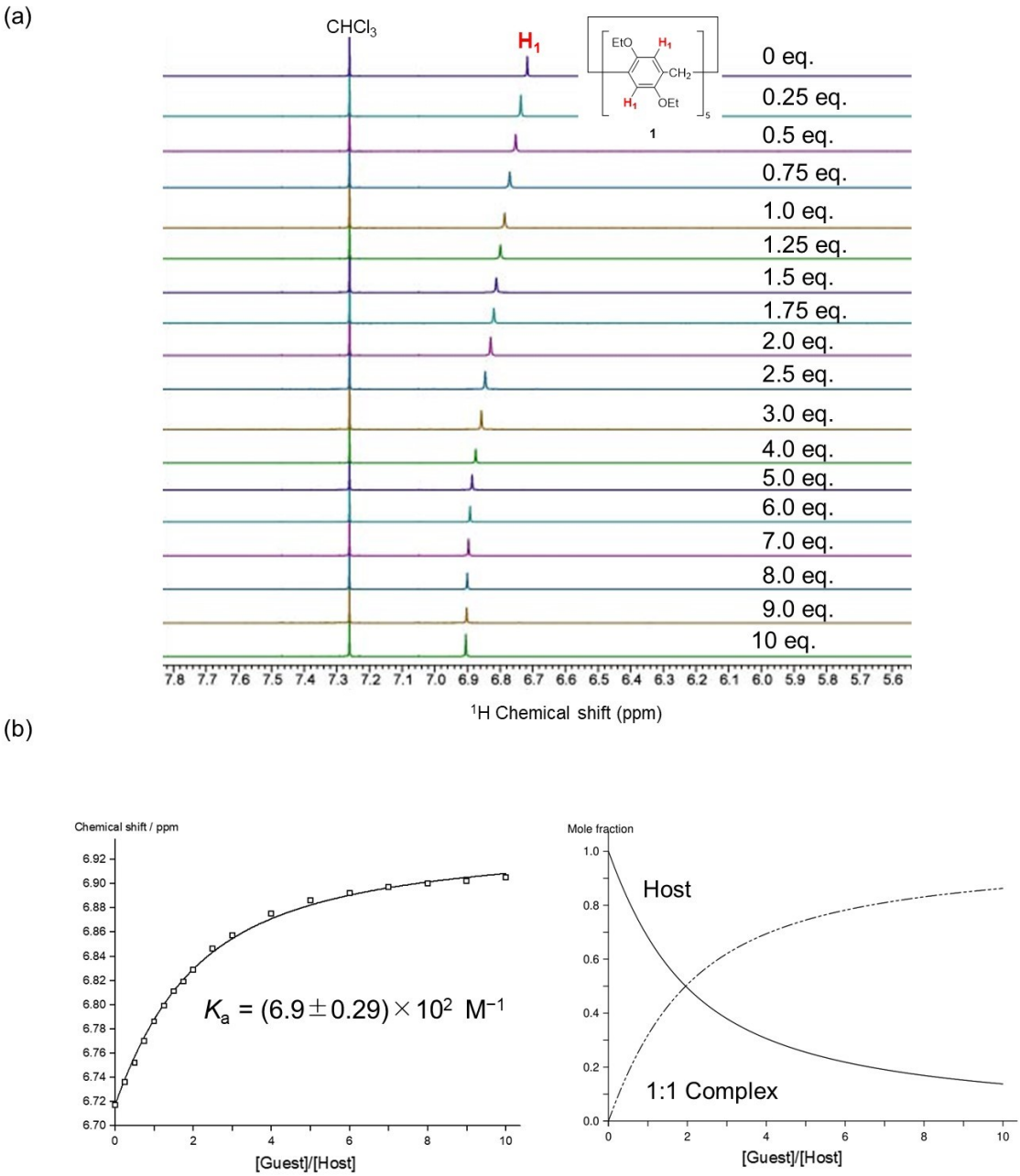

Figure S31. (a) Partial ^{1}H NMR spectra (500 MHz, $CDCl_3$, 295 K) of **1** (1.0 mM) upon addition of **C2** (0–10 eq.). (b) The non-linear curve fitting and the mole fraction of the species for the titration experiment in (a) based on the chemical shift of H_1.

(a)

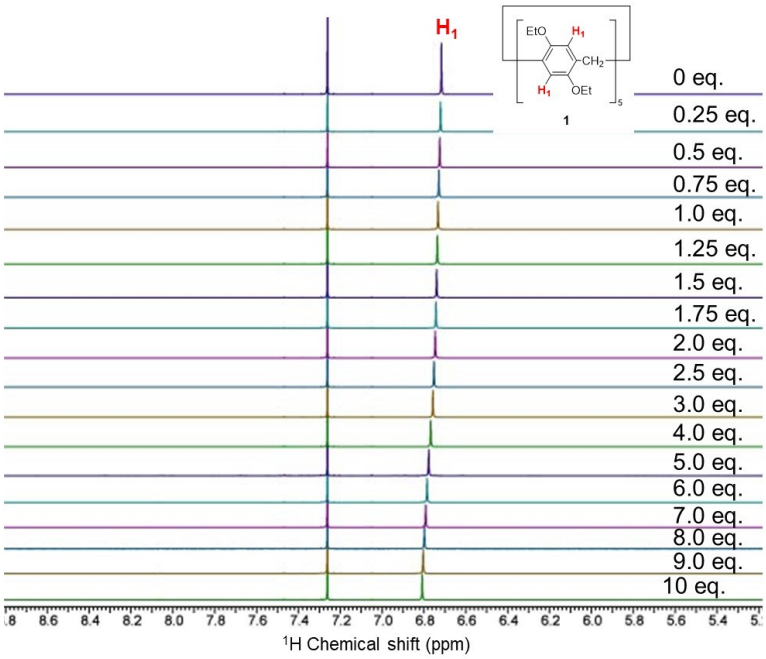

(b)

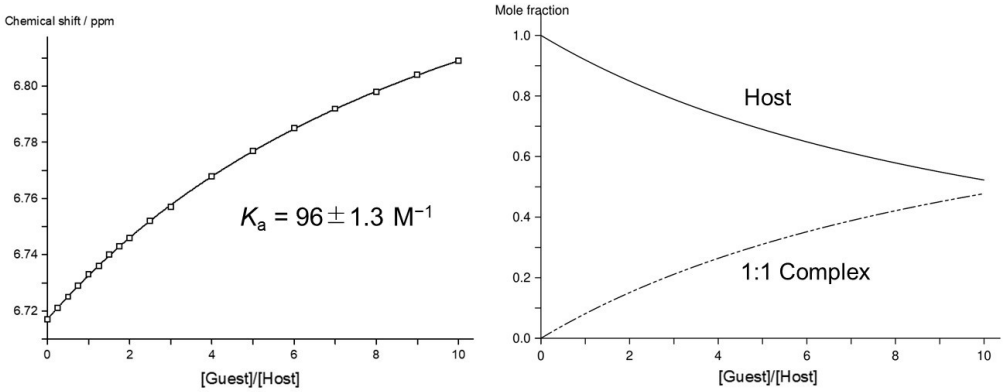

Figure S32. (a) Partial ^{1}H NMR spectra (500 MHz, $CDCl_3$, 295 K) of **1** (1.0 mM) upon addition of **C14** (0–10 eq.). (b) The non-linear curve fitting and the mole fraction of the species for the titration experiment in (a) based on the chemical shift of H_1.

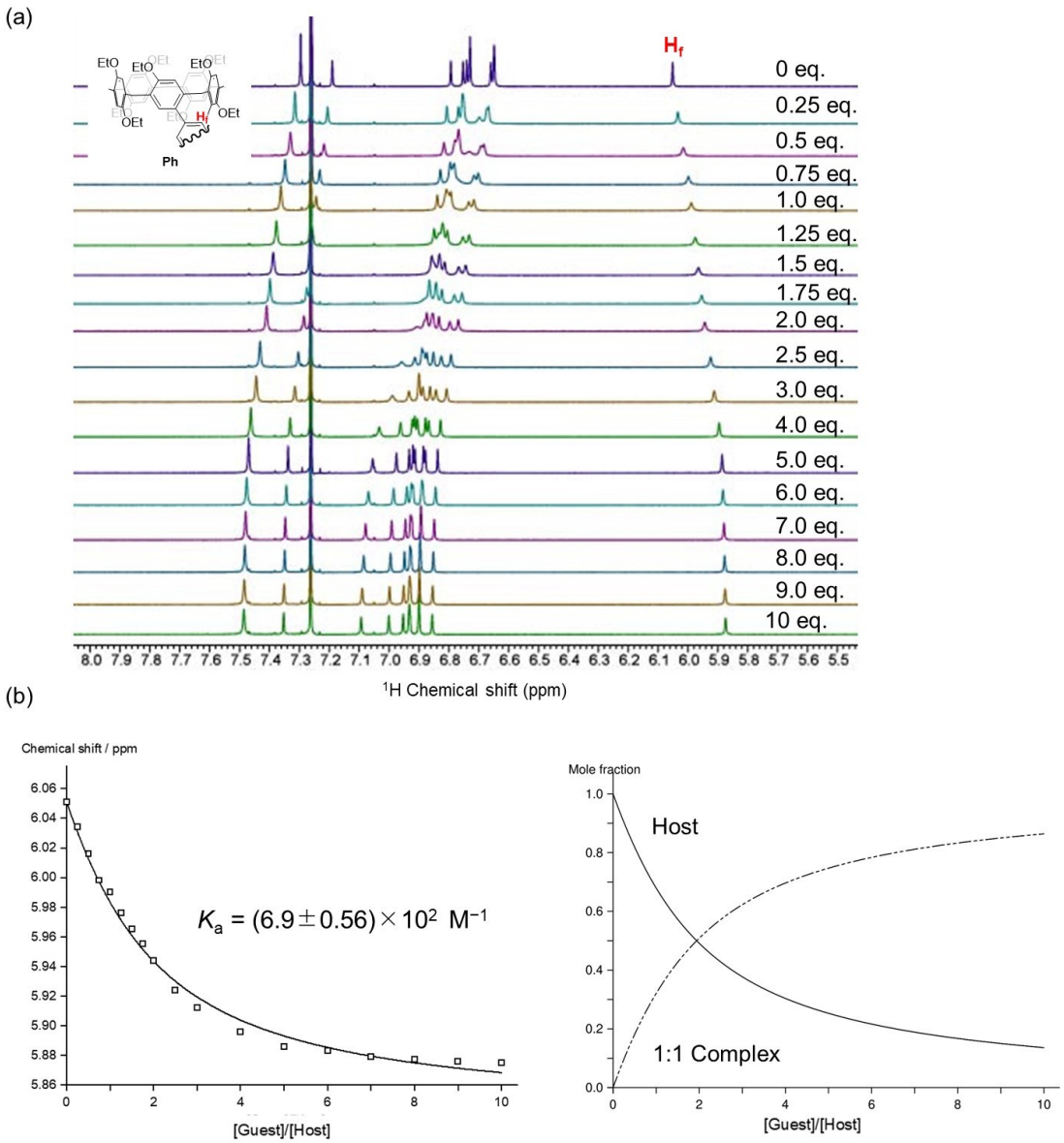

Figure S33. (a) Partial ^{1}H NMR spectra (500 MHz, $CDCl_3$, 295 K) of **Ph** (1.0 mM) upon addition of **C2** (0–10 eq.). (b) The non-linear curve fitting and the mole fraction of the species for the titration experiment in (a) based on the chemical shift of H_f.

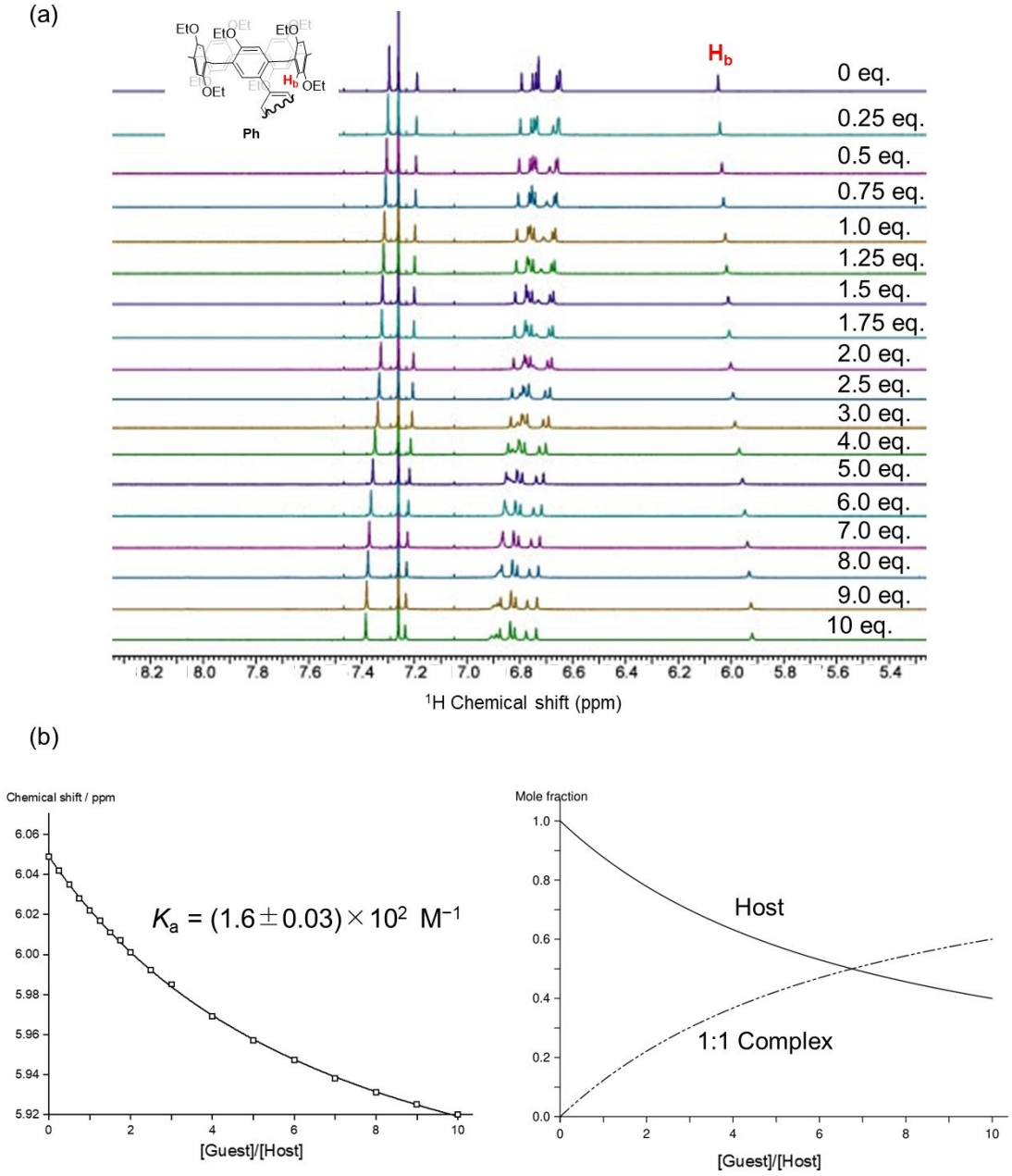

Figure S34. (a) Partial ^{1}H NMR spectra (500 MHz, $CDCl_3$, 295 K) of **Ph** (1.0 mM) upon addition of **C14** (0–10 eq.). (b) The non-linear curve fitting and the mole fraction of the species for the titration experiment in (a) based on the chemical shift of H_f.

(a)

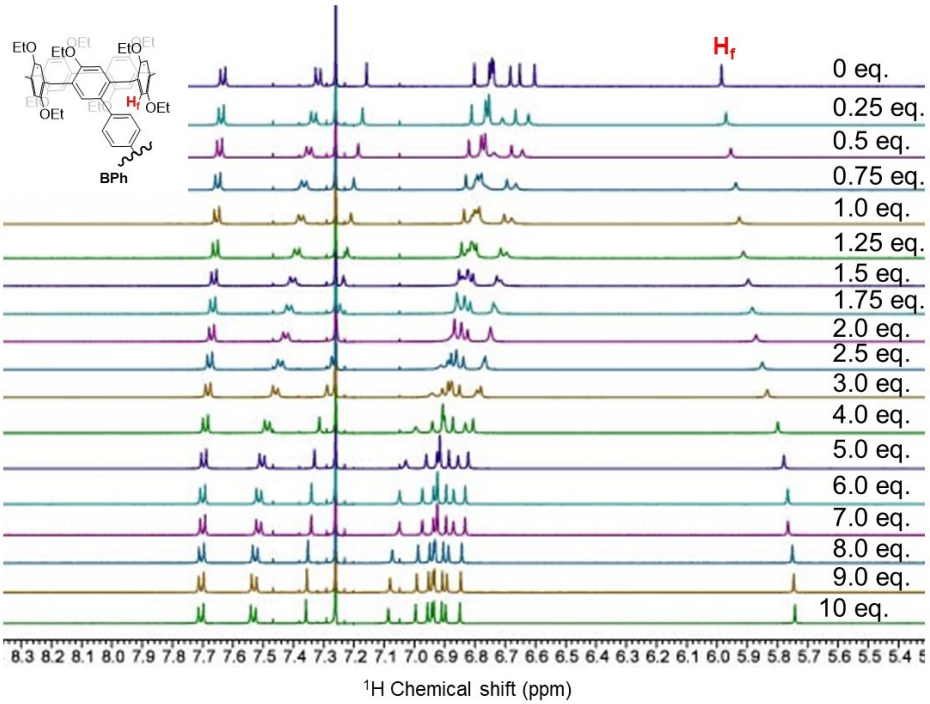

(b)

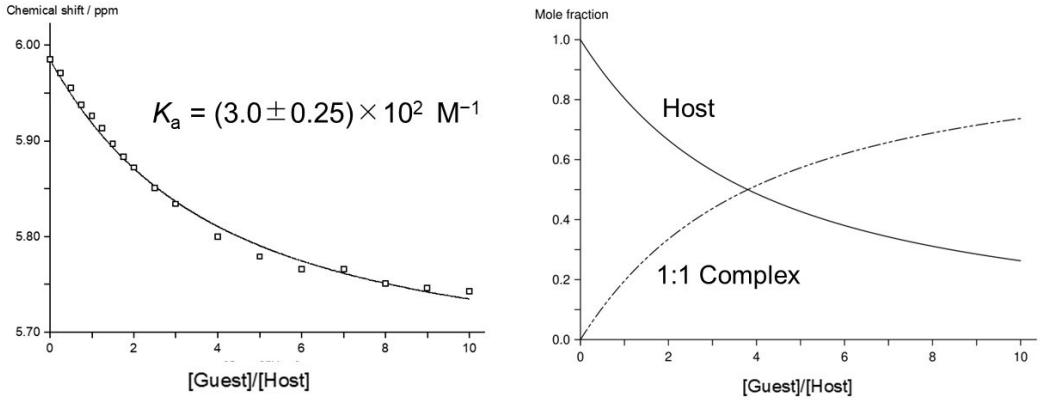

Figure S35. (a) Partial ^{1}H NMR spectra (500 MHz, $CDCl_3$, 295 K) of **BPh** (1.0 mM) upon addition of **C2** (0–10 eq.). (b) The non-linear curve fitting and the mole fraction of the species for the titration experiment in (a) based on the chemical shift of H_f.

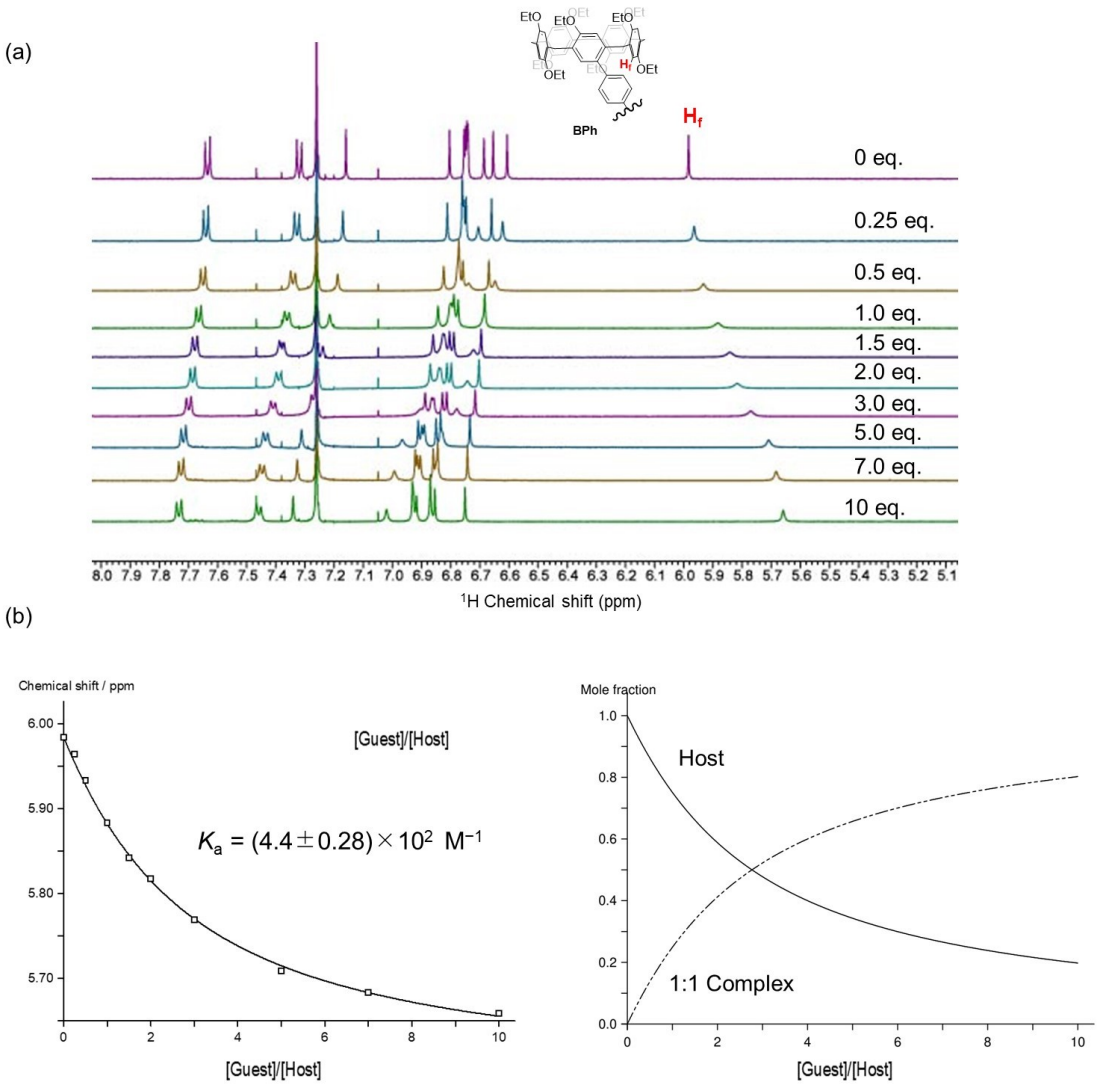

Figure S36. (a) Partial ^{1}H NMR spectra (500 MHz, $CDCl_3$, 295 K) of **BPh** (1.0 mM) upon addition of **C14** (0–10 eq.). (b) The non-linear curve fitting and the mole fraction of the species for the titration experiment in (a) based on the chemical shift of H_f.

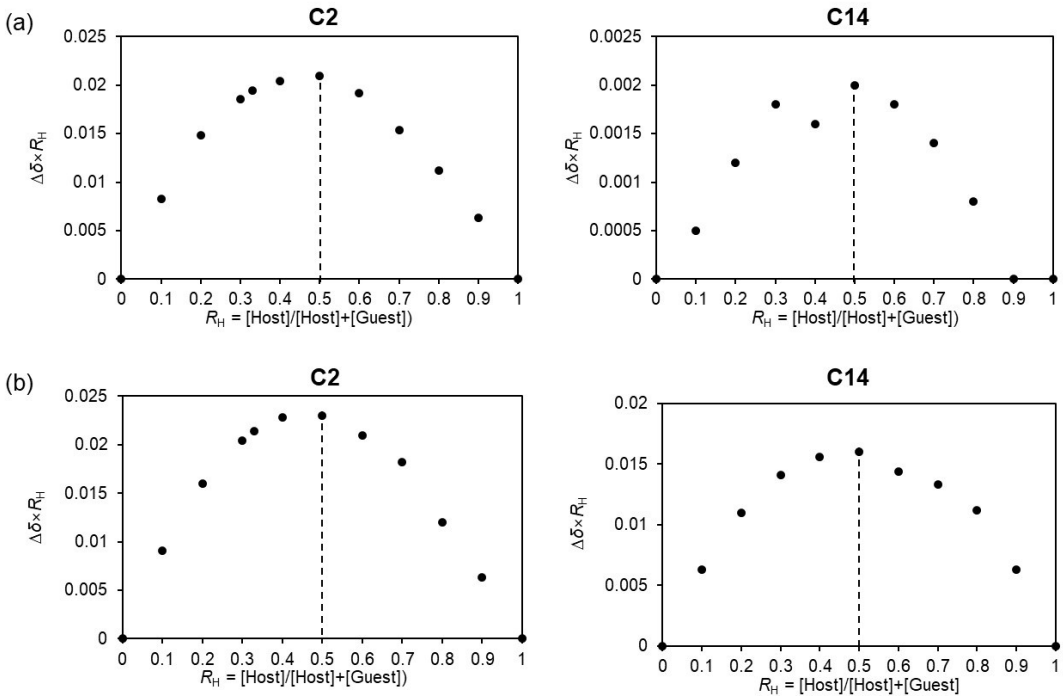

Figure S37. Job's plot experiments for (a) **Ph** with **C2** and **C14** and (b) **BPh** with **C2** and **C14** ([Host]+[Guest] = 1.0 mM, 500 MHz, $CDCl_3$, 295 K).

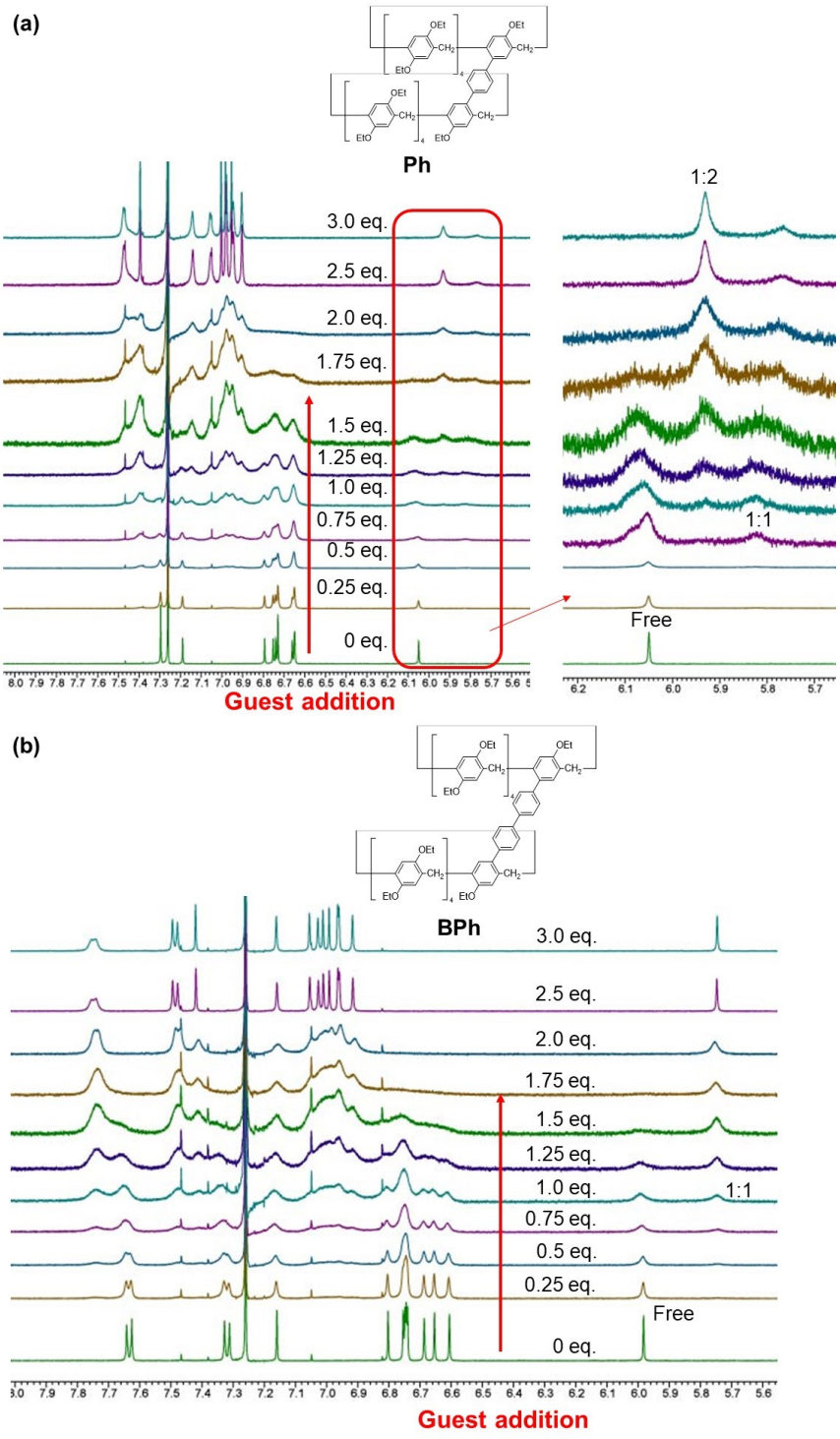

Figure S38. Partial ^{1}H NMR spectra (500 MHz, $CDCl_3$, 295 K) of (a) **Ph** and (b) **BPh** (1.0 mM) upon addition of 1,2-dicyanoethane (0–3.0 eq.).

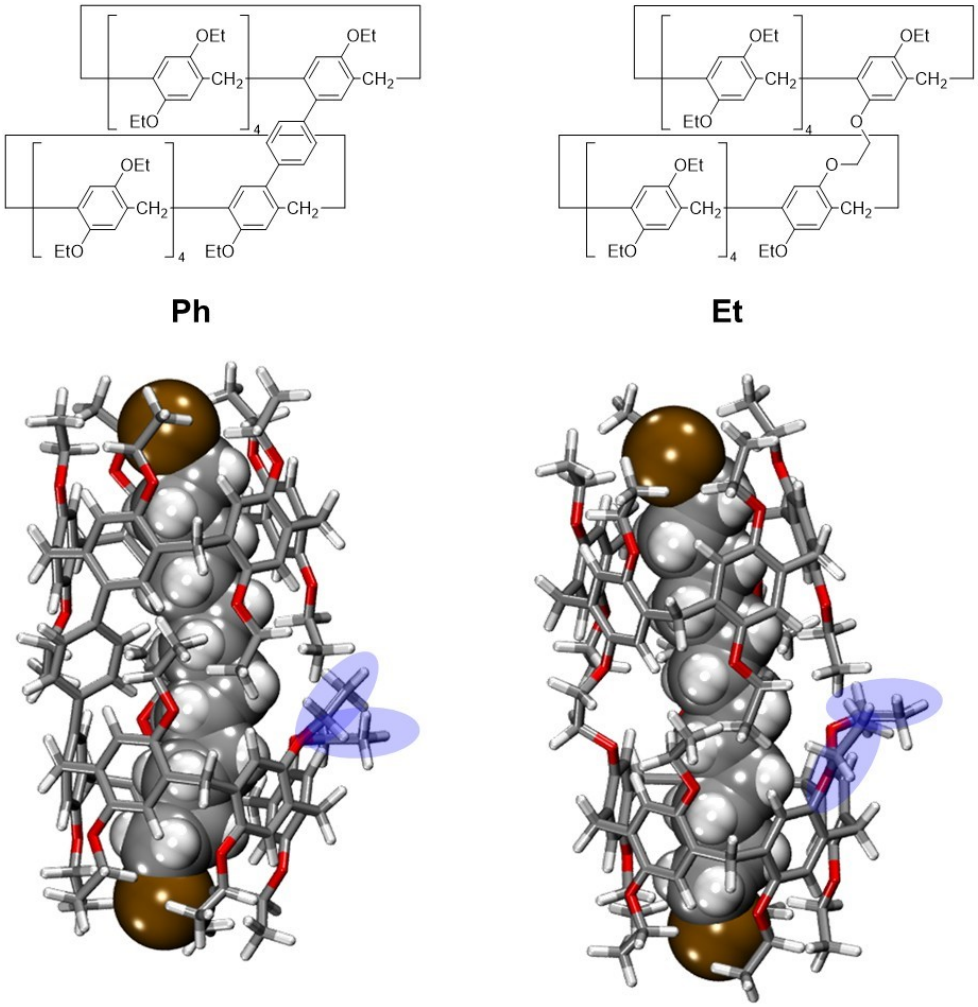

Figure S39. Optimized geometries of host–guest complexes of a) **C12@Ph** and b) **C12@Et** calculated at the M06-2X/6-31G(d,p) level of theory. The outward bending of ethoxy groups highlighted in blue circles means steric hindrance.

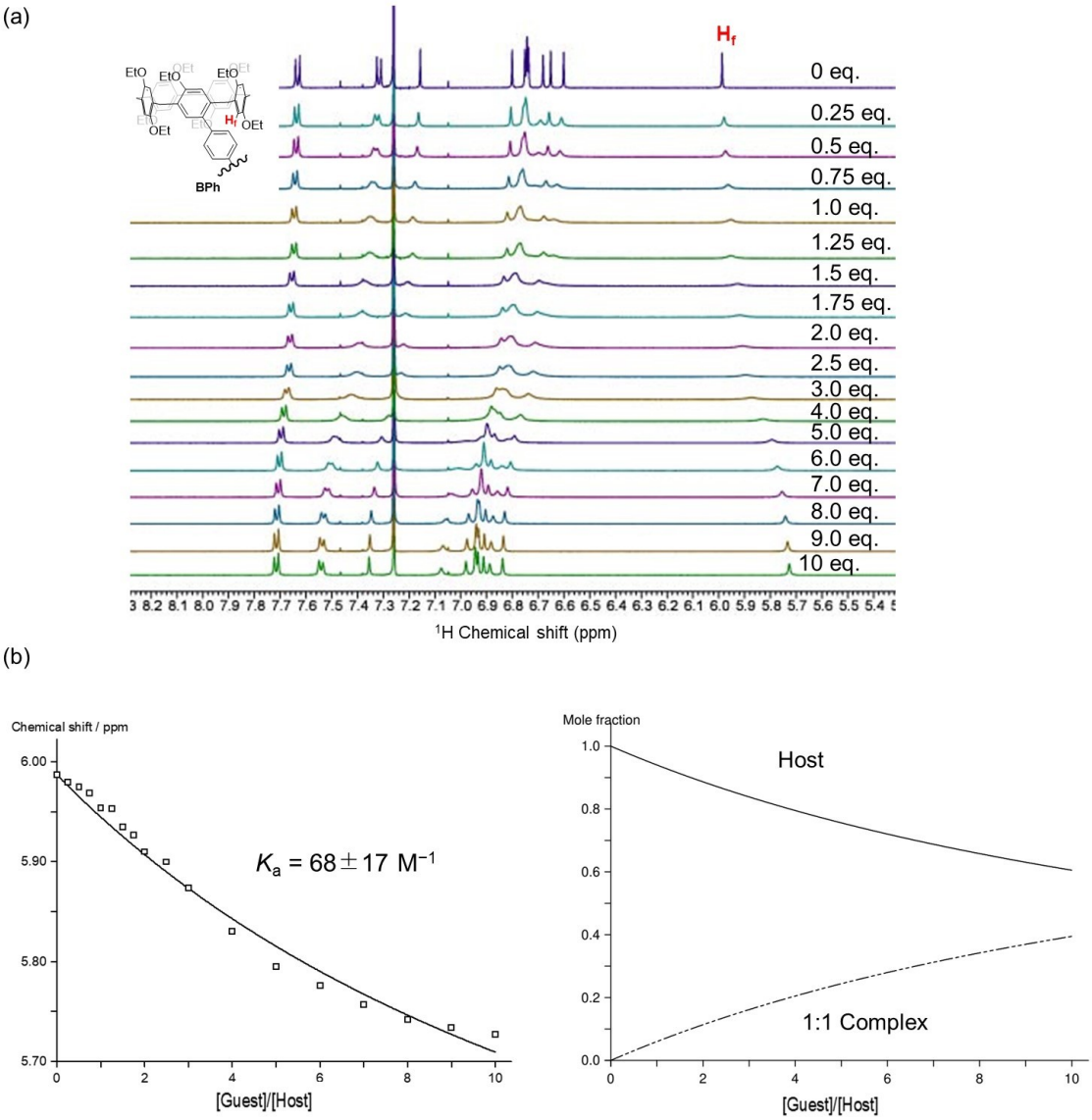

Figure S40. (a) Partial ^{1}H NMR spectra (500 MHz, $CDCl_3$, 295 K) of **BPh** (1.0 mM) upon addition of **C4** (0–10 eq.). (b) The non-linear curve fitting and the mole fraction of the species for the titration experiment in (a) based on the chemical shift of H_f.

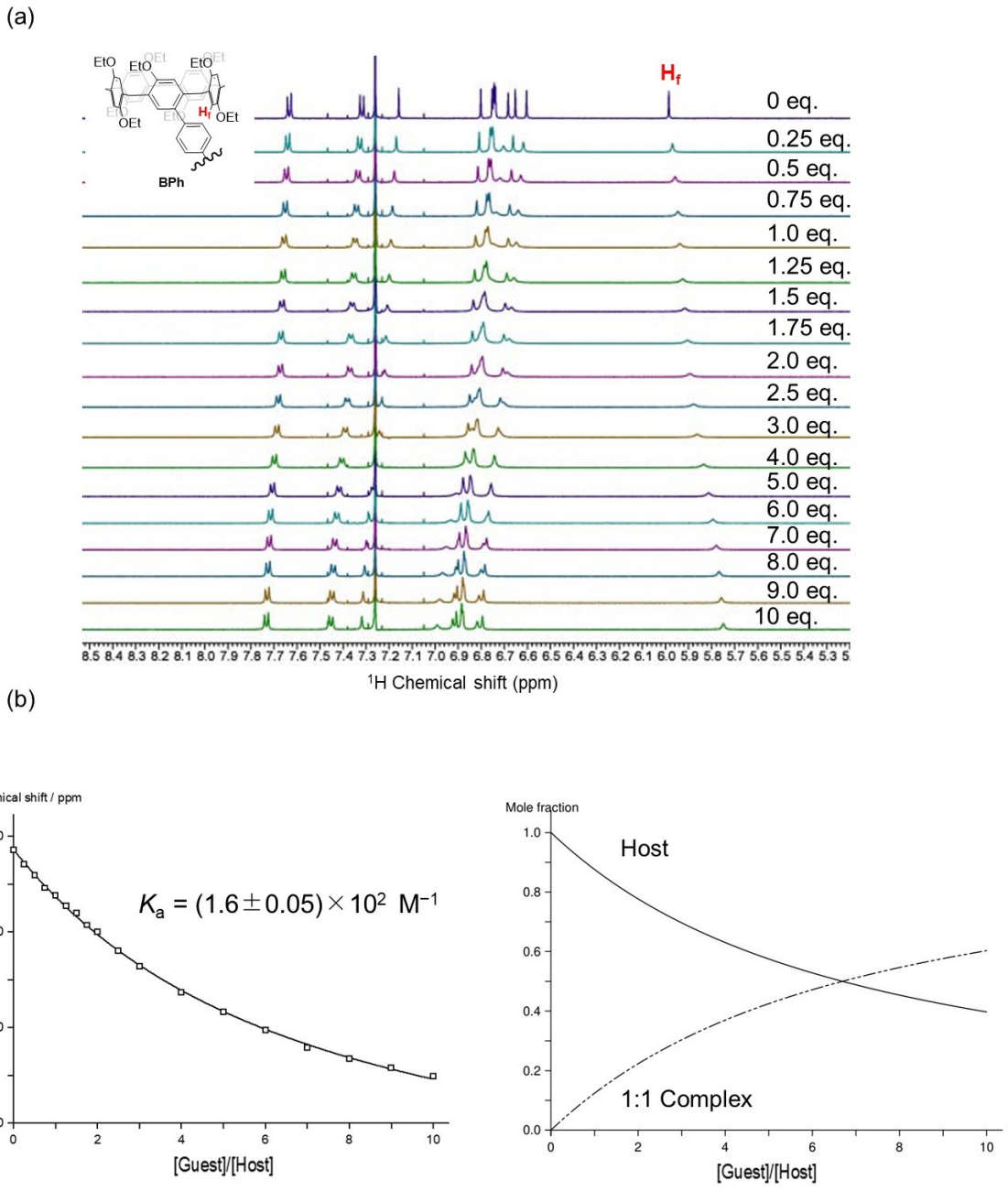

Figure S41. (a) Partial ^{1}H NMR spectra (500 MHz, $CDCl_3$, 295 K) of **BPh** (1.0 mM) upon addition of **C6** (0–10 eq.). (b) The non-linear curve fitting and the mole fraction of the species for the titration experiment in (a) based on the chemical shift of H_f.

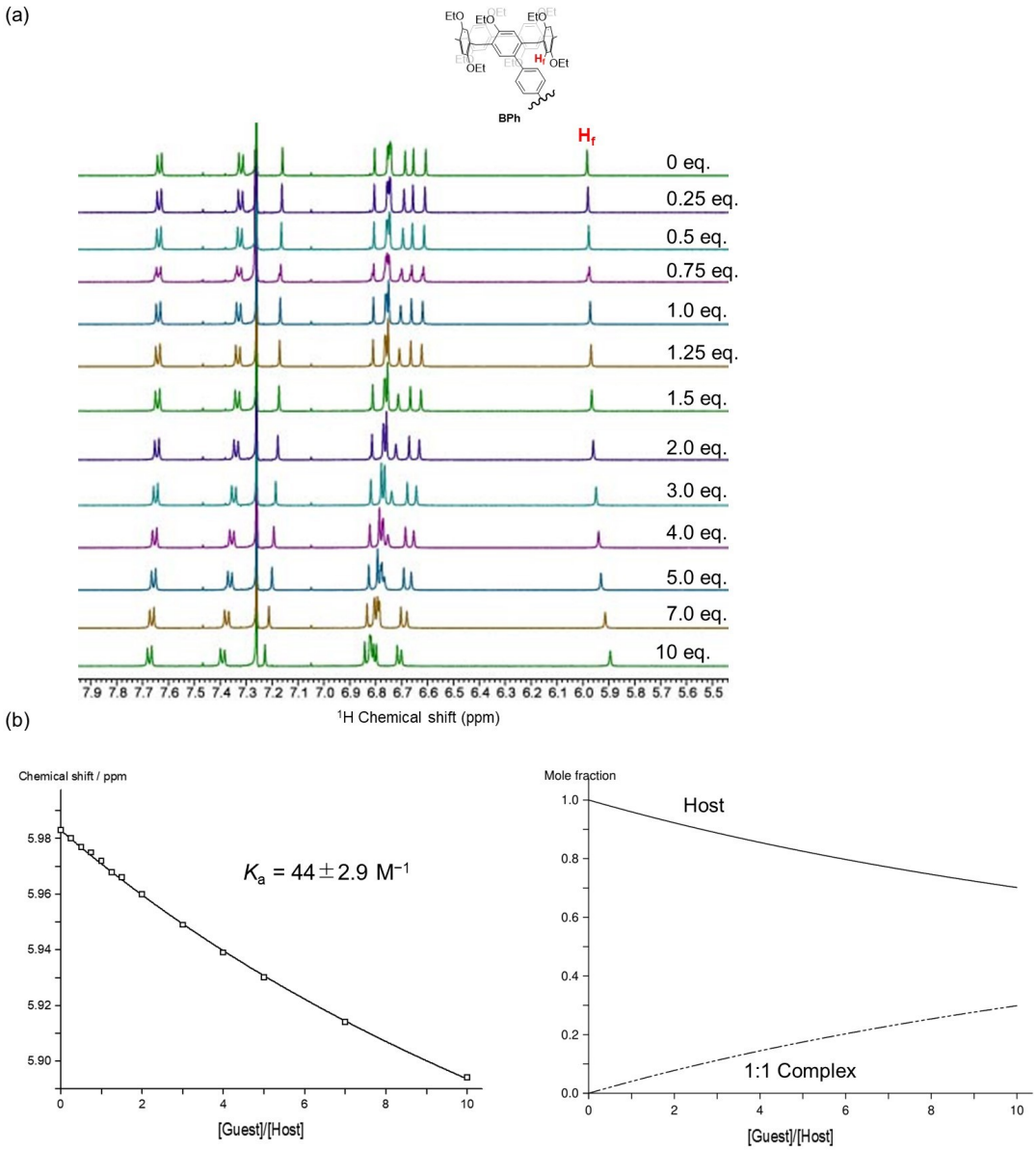

Figure S42. (a) Partial ^{1}H NMR spectra (500 MHz, $CDCl_3$, 295 K of **BPh** (1.0 mM) upon addition of **C8** (0–10 eq.). (b) The non-linear curve fitting and the mole fraction of the species for the titration experiment in (a) based on the chemical shift of H_f.

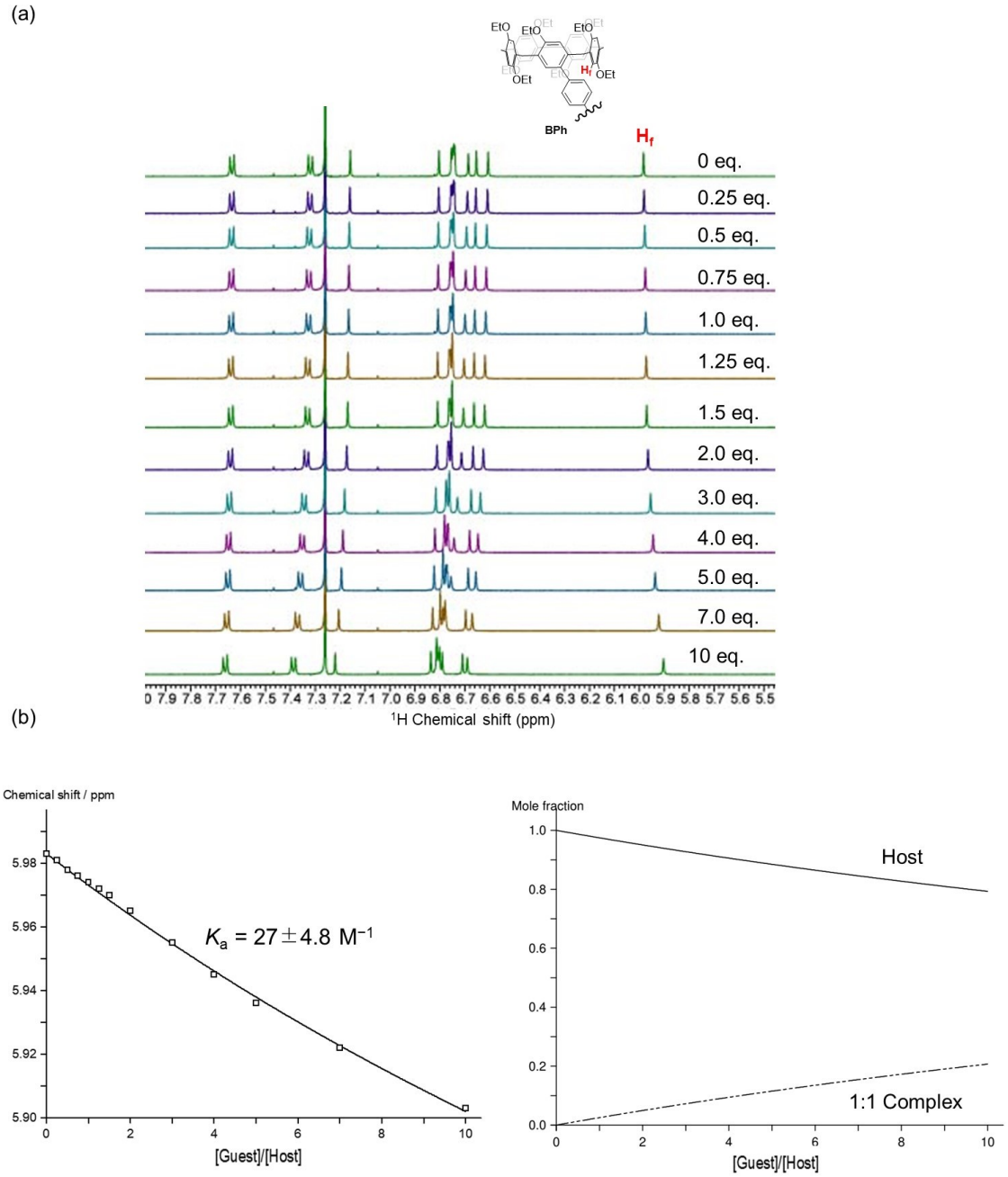

Figure S43. (a) Partial ^{1}H NMR spectra (500 MHz, $CDCl_3$, 295 K) of **BPh** (1.0 mM) upon addition of **C10** (0–10 eq.). (b) The non-linear curve fitting and the mole fraction of the species for the titration experiment in (a) based on the chemical shift of H_f.

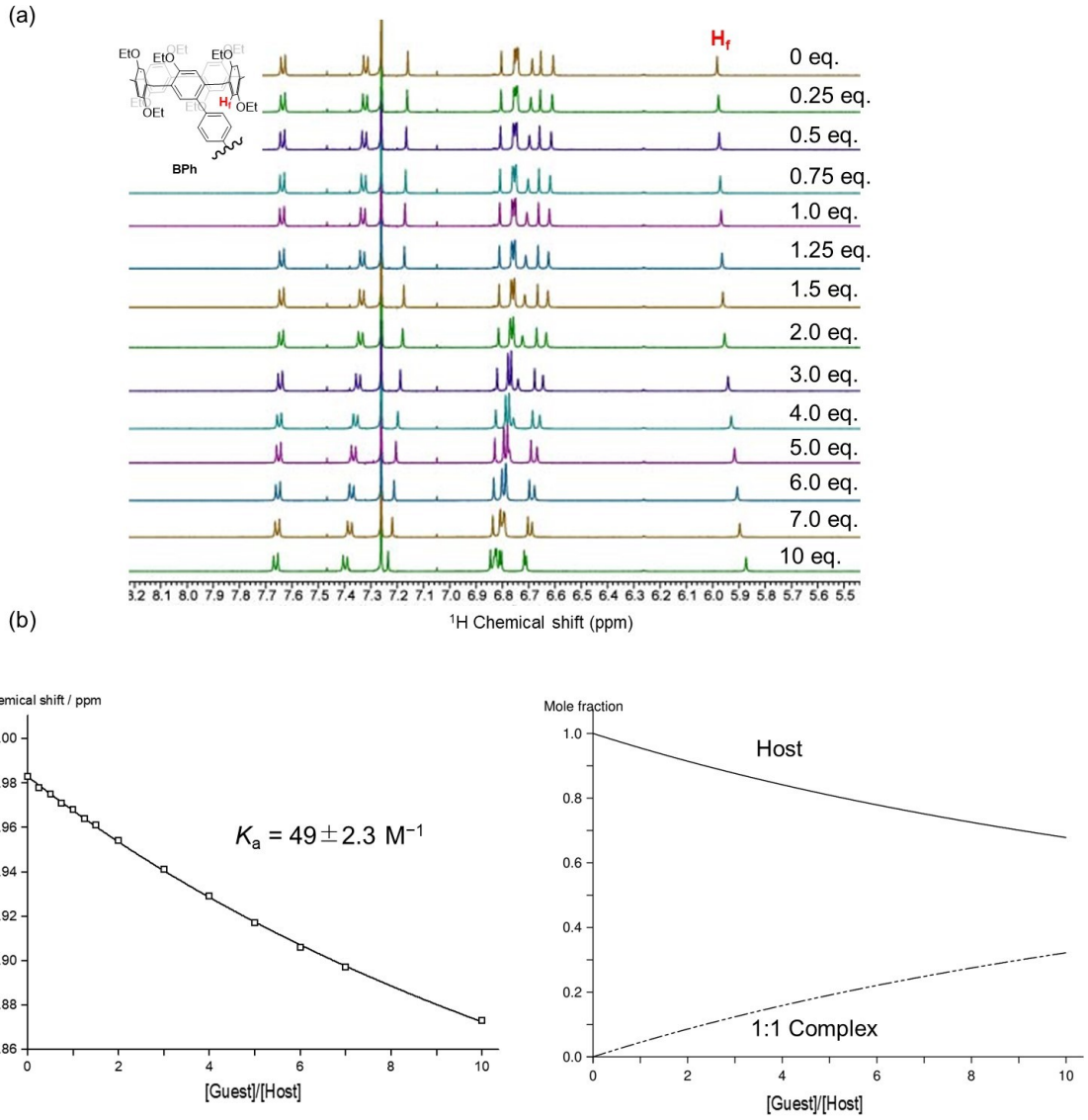

Figure S44. (a) Partial ^{1}H NMR spectra (500 MHz, $CDCl_3$, 295 K) of **BPh** (1.0 mM) upon addition of **C12** (0–10 eq.). (b) The non-linear curve fitting and the mole fraction of the species for the titration experiment in (a) based on the chemical shift of H_f.

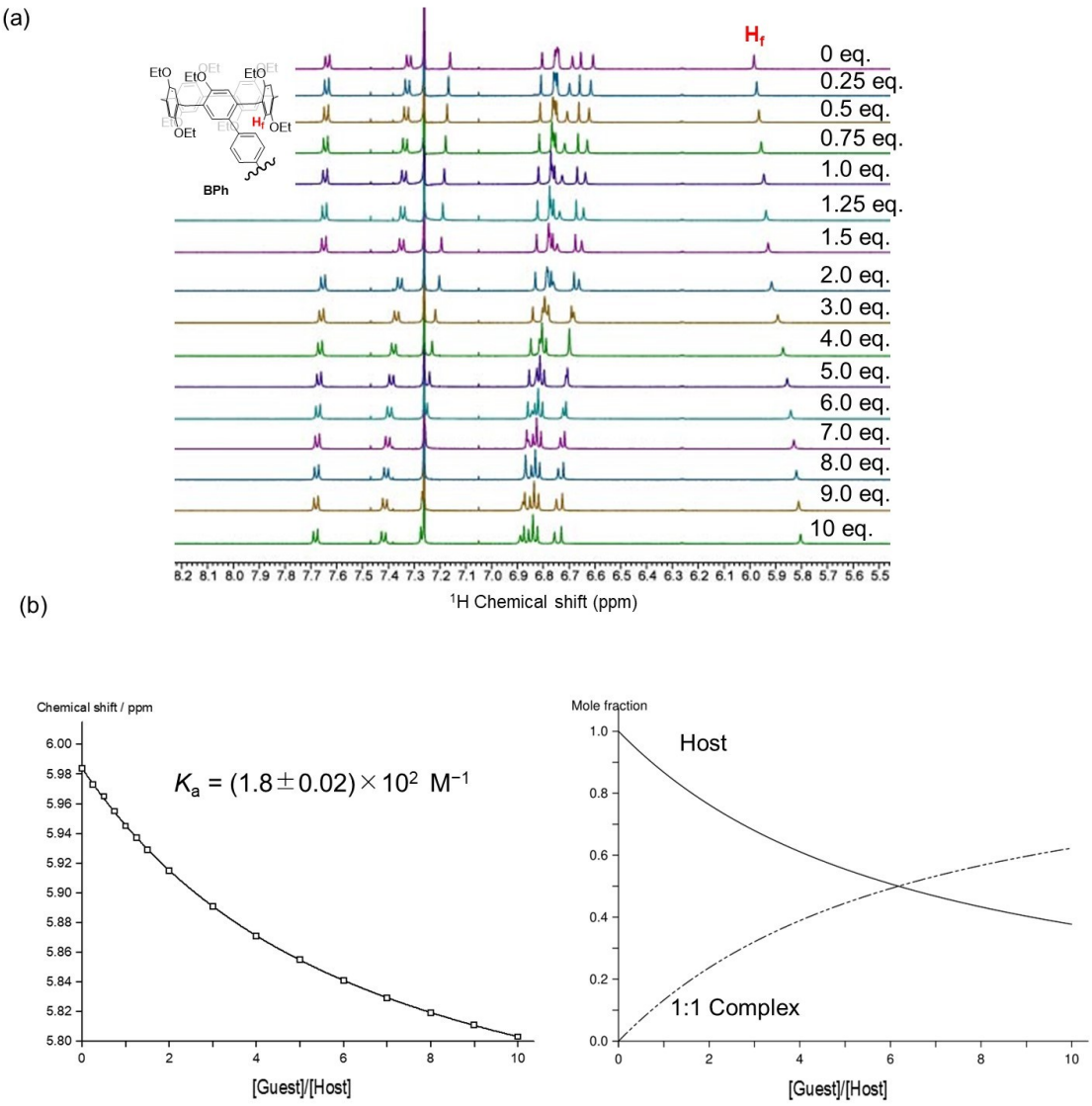

Figure S45. (a) Partial ^{1}H NMR spectra (500 MHz, $CDCl_3$, 295 K) of **BPh** (1.0 mM) upon addition of **C13** (0–10 eq.). (b) The non-linear curve fitting and the mole fraction of the species for the titration experiment in (a) based on the chemical shift of H_f.

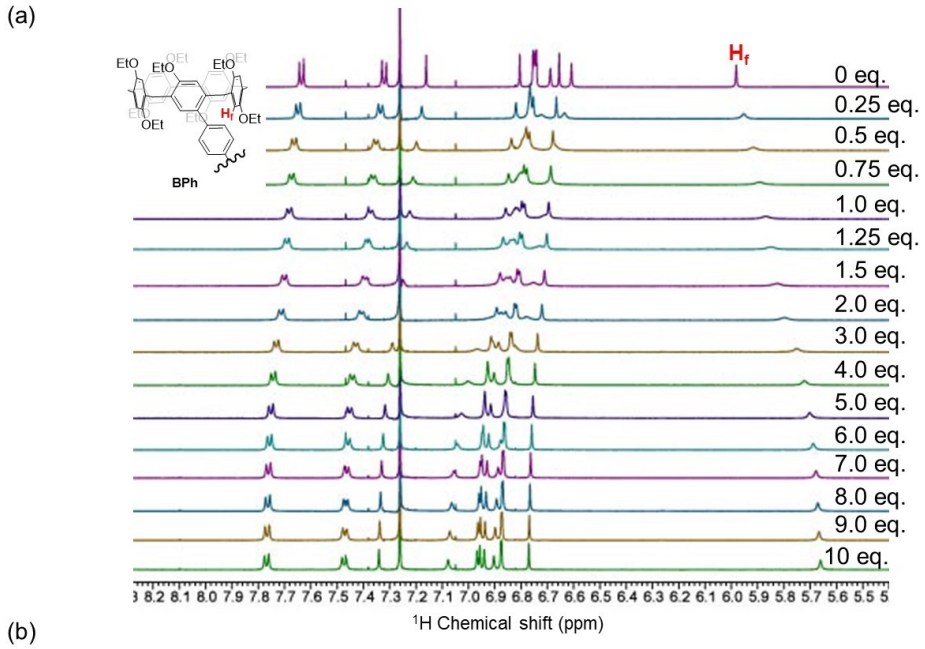

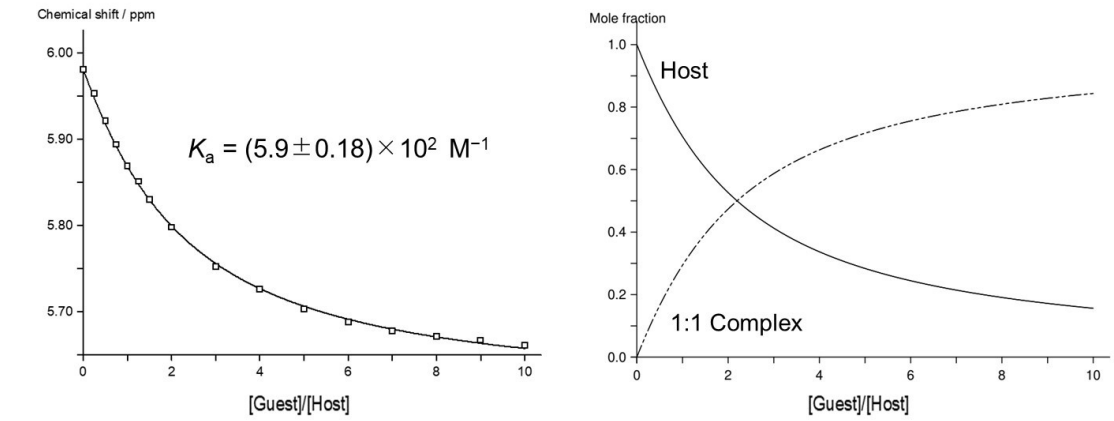

Figure S46. (a) Partial ^{1}H NMR spectra (500 MHz, $CDCl_3$, 295 K) of **BPh** (1.0 mM) upon addition of **C15** (0–10 eq.). (b) The non-linear curve fitting and the mole fraction of the species for the titration experiment in (a) based on the chemical shift of H_f.

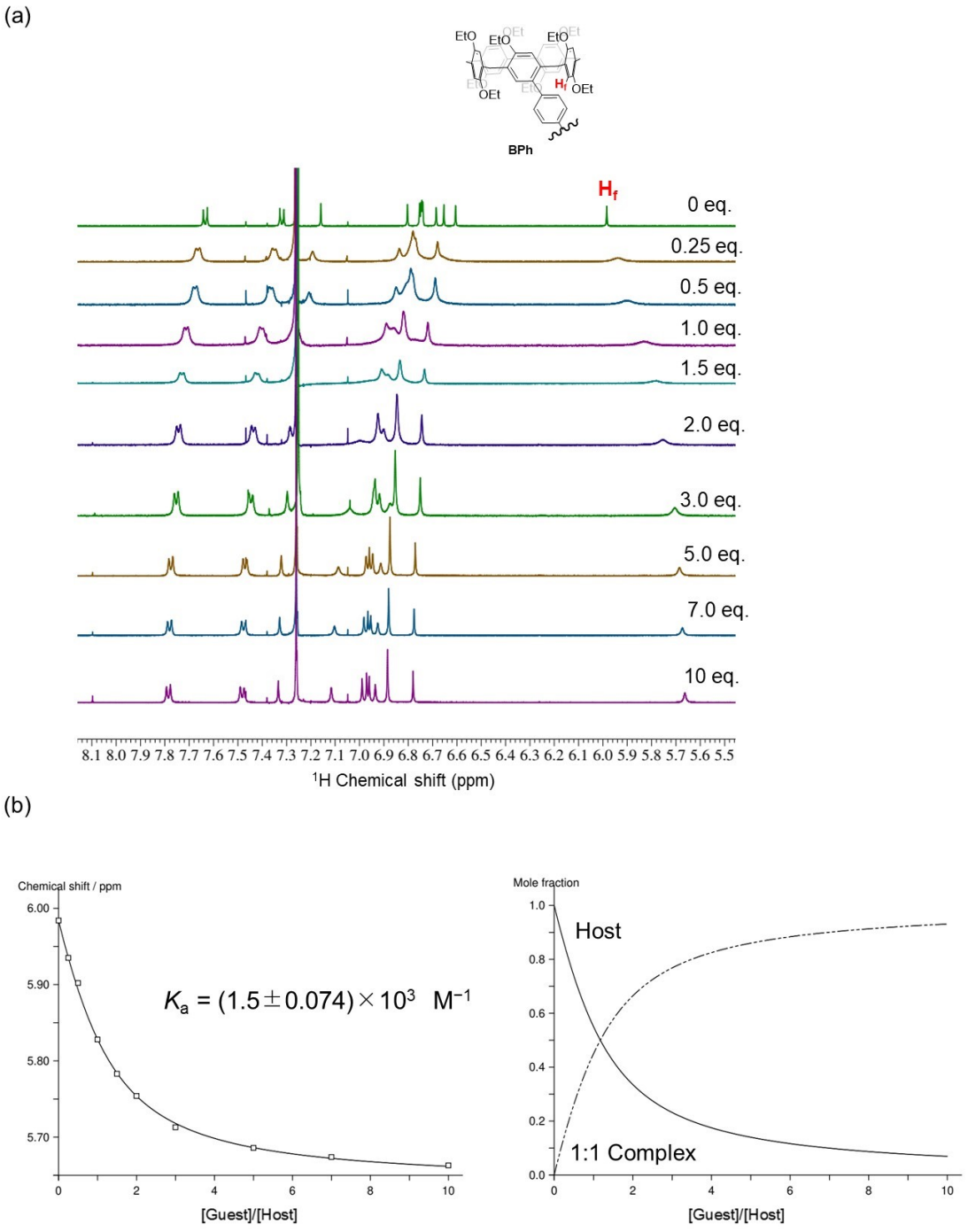

Figure S47. (a) Partial ^{1}H NMR spectra (500 MHz, $CDCl_3$, 295 K) of **BPh** (1.0 mM) upon addition of **C16** (0–10 eq.). (b) The non-linear curve fitting and the mole fraction of the species for the titration experiment in (a) based on the chemical shift of H_f.

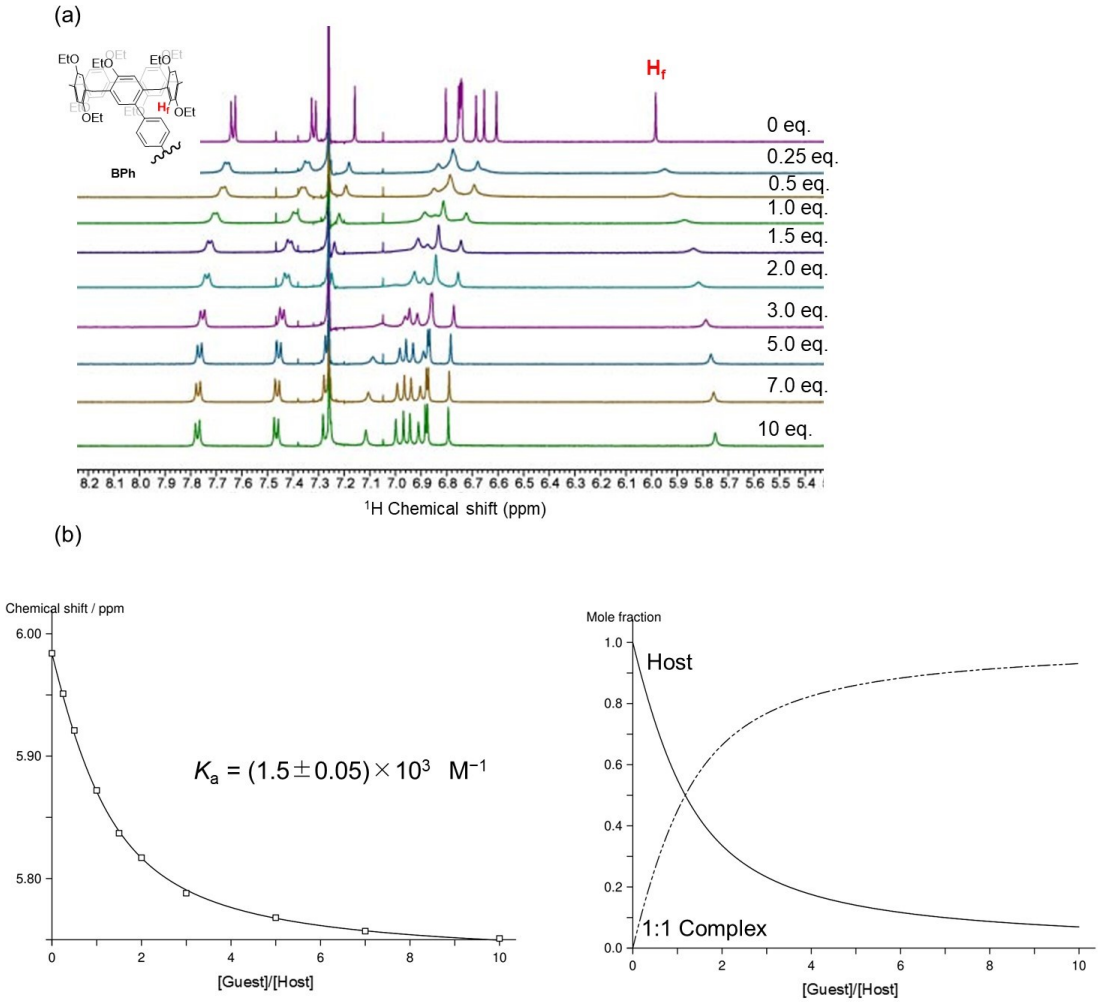

Figure S48. (a) Partial ^{1}H NMR spectra (500 MHz, $CDCl_3$, 295 K) of **BPh** (1.0 mM) upon addition of **C18** (0–10 eq.). (b) The non-linear curve fitting and the mole fraction of the species for the titration experiment in (a) based on the chemical shift of H_f.

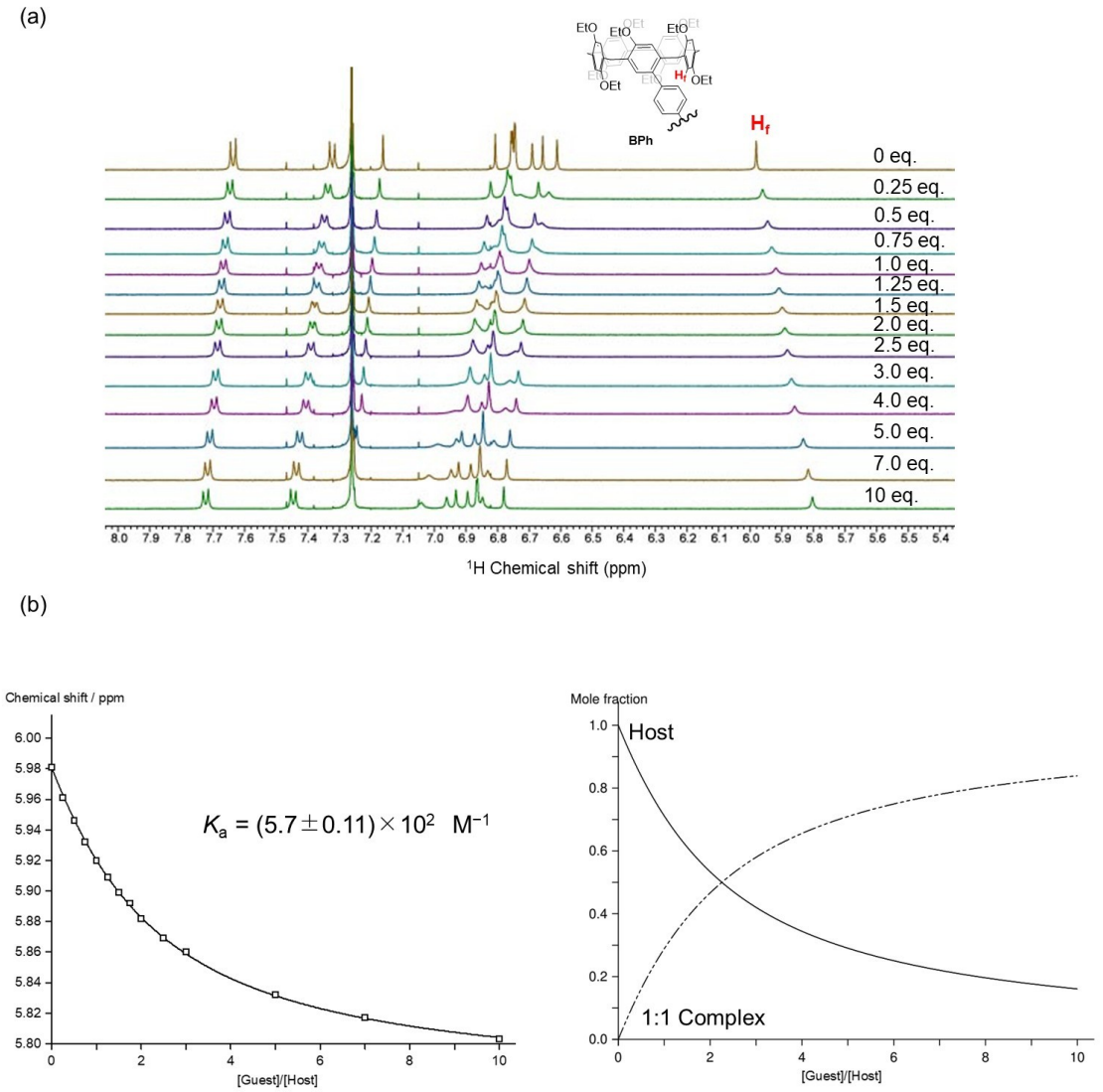

Figure S49. (a) Partial ^{1}H NMR spectra (500 MHz, $CDCl_3$, 295 K) of **BPh** (1.0 mM) upon addition of **C20** (0–10 eq.). (b) The non-linear curve fitting and the mole fraction of the species for the titration experiment in (a) based on the chemical shift of H_f.

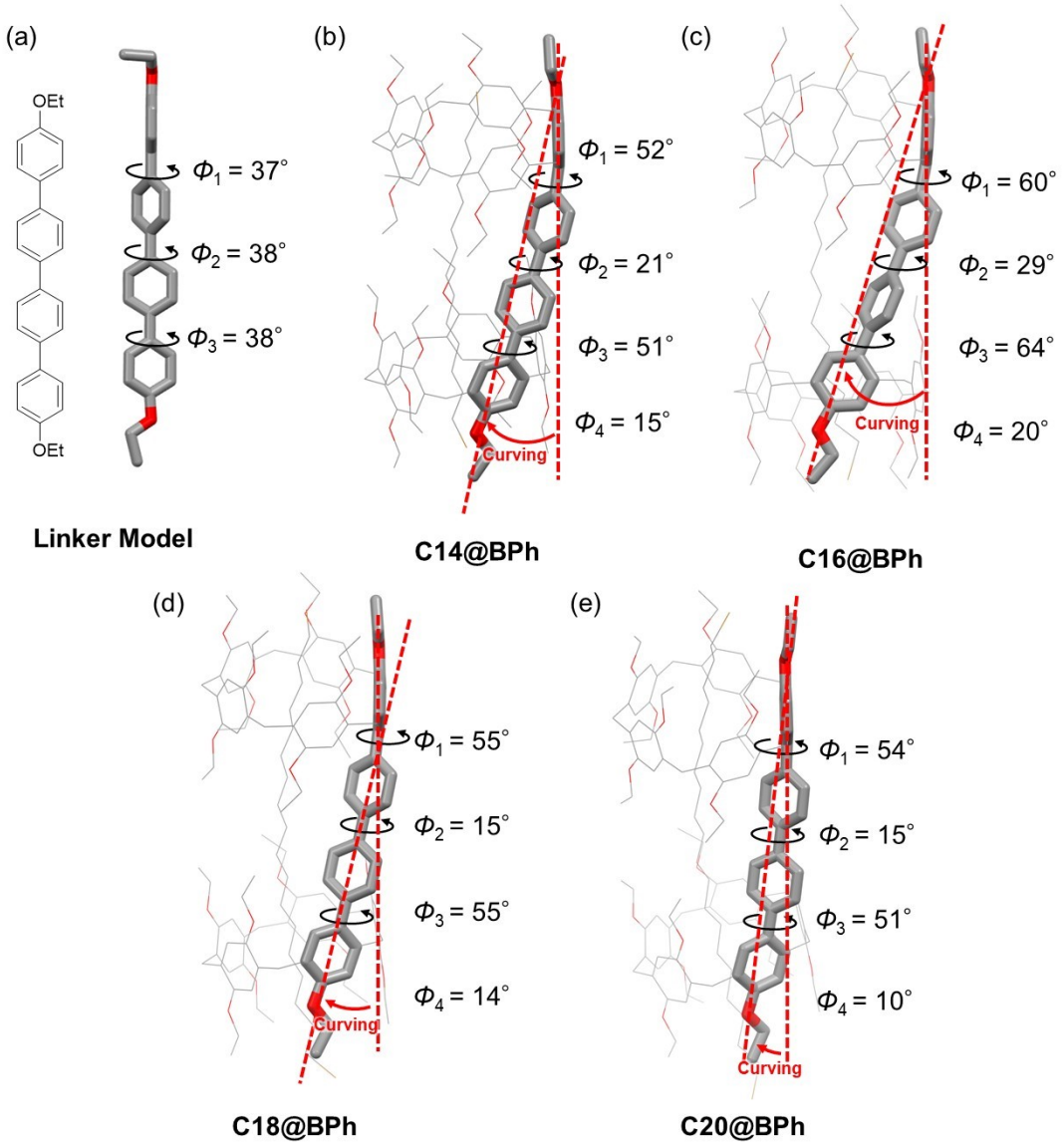

Figure S50. The optimized geometries of (a) **Linker Model**, (b) **C14@BPh**, (c) **C16@BPh**, (d) **C18@BPh**, and (e) **C20@BPh** illustrating the curving and twisting of the linker moieties. The geometry of **Linker Model** was optimized at the M06-2X/6-31G(d,p) level of theory.

ESI Note 4

ESI-MS spectrometry for **C14@BPh**, **C16@BPh**, **C18@BPh**, and **C20@BPh**.

We performed ESI-MS spectrometry for **C14@BPh**, **C16@BPh**, **C18@BPh**, and **C20@BPh** (Figure S51). However, no peaks corresponding to the host–guest complexes were observed. This is likely due to the relatively weak binding affinity of **BPh**, combined with possible dethreading of the guest molecules during the ionization process.

^{1}H NMR analysis of host–guest complex structures of **BPh**

The host–guest complex structures of **C14@BPh**, **C16@BPh**, **C18@BPh**, and **C20@BPh** were analyzed by ^{1}H NMR at 233 K to reduce guest molecular motion. Although the proton peaks near the central parts of guest molecules could not be assigned due to the limitation of sensitivity, most of the proton signals of guests in the host–guest complexes were successfully assigned by ^{1}H–^{1}H COSY spectroscopy (Figures S52–S59). These measurements provided insights into the guest conformations during the host–guest complexations. Upon complexation with **C14**, proton signals of **C14** showed upfield shifts due to shielding from the pillar[5]arene cavities (Figure S60). Similar peak shift trends were observed for **C16**, **C18**, and **C20** complexes (Figures S61–S63). Furthermore, as the length of the guest increased, the proton signals at the α and β positions shifted downfield, whereas those at the γ, δ, and ε positions exhibited upfield shifts (Figure S64). This trend can be explained by considering that the α and β protons, located at the terminal regions, become less shielded with increasing guest length because of the protruding from the host cavity. In contrast, the γ, δ, and ε protons, which are positioned closer to the central part of the guest molecules, tend to experience enhanced shielding from the host cavity, resulting in increased upfield shifts. Therefore, we concluded that the guests adopted linearly-extended conformations, as suggested by DFT calculations.

On the other hand, another set of peaks of **C18** and **C20** was observed below 0 ppm (indicated by black arrows in Figures S62 and S63). These peaks are likely due to an incomplete host–guest complex structure, where one of the cavities of **BPh** solely captured **C18** and **C20** because the system did not reach equilibrium upon the addition of 5.0 eq. of **C18** and **C20**. As another possibility, the small peaks may arise from the formation of supramolecular polymers. We were unable to identify these small peaks due to their low sensitivity in the DOSY measurements at 233 K. Nevertheless, the peak intensities of this minor component are significantly lower than those of 1:1 complex under this concentration.

Cooperative binding of **BPh** for shorter guests

For longer guests (≥**C14**), **BPh** exhibits length-adaptive binding by adjusting the relative positions of its two cavities and accommodating the curved conformation of the alkane chain (Figure S65b,c). This allows the most electropositive hydrogen atoms of the guest to approach the electronegative

oxygen atoms of the host. In contrast, cooperative binding of a shorter guest would require the two cavities to bend inward, which is sterically hindered by the ethoxy groups (Figure S65a). As a result, length-adaptive binding has not been observed for shorter guests. Indeed, in the optimized structure of **C6@BPh**, cooperative binding involving two cavities was not suggested, even though **C6** had been initially placed across the two cavities prior to geometry optimization; only one cavity was involved in capturing the **C6** guest.

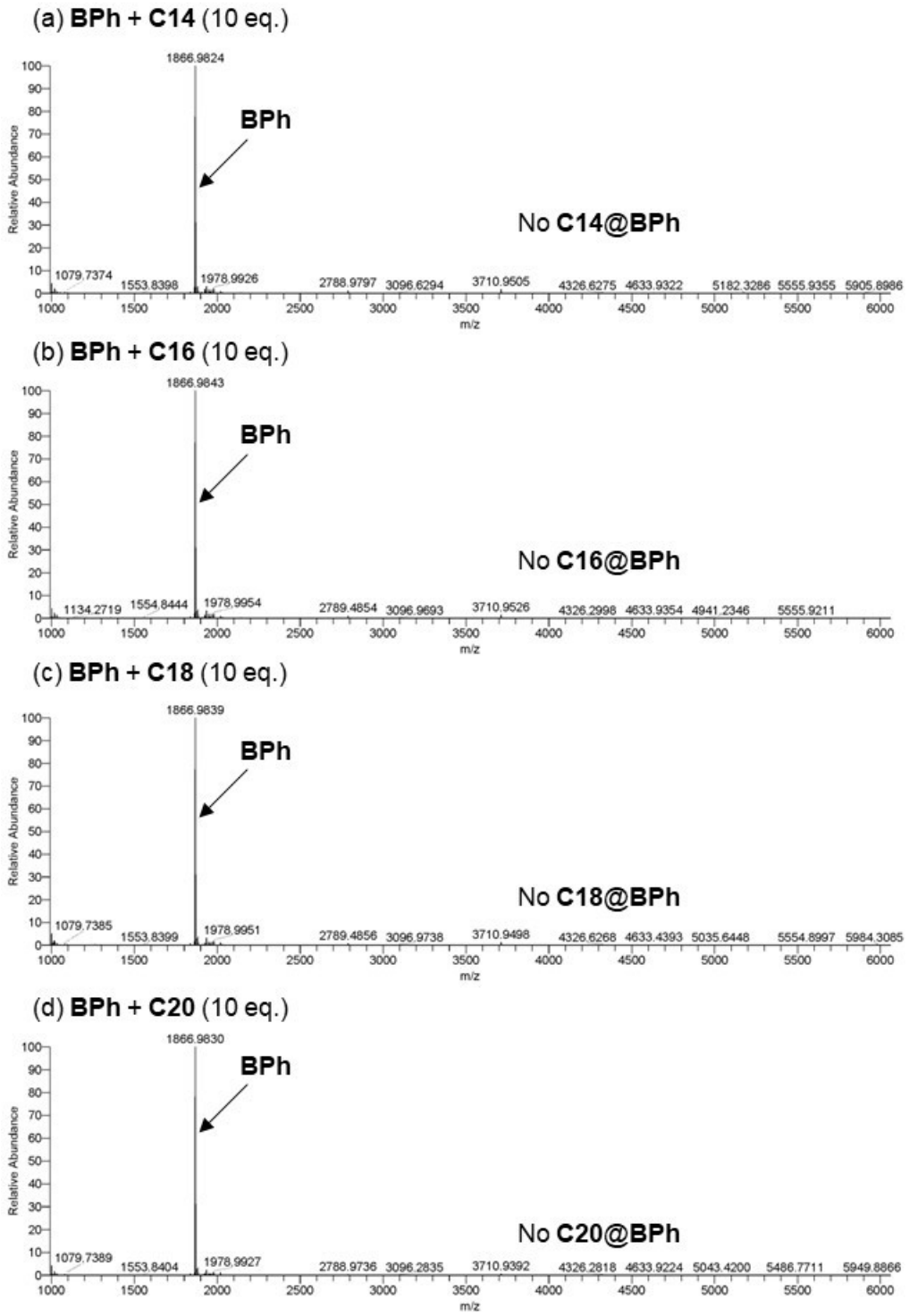

Figure S51. ESI-MS spectra of **BPh** with 10 eq. of (a) **C14**, (b) **C16**, (c) **C18**, and (d) **C20**.

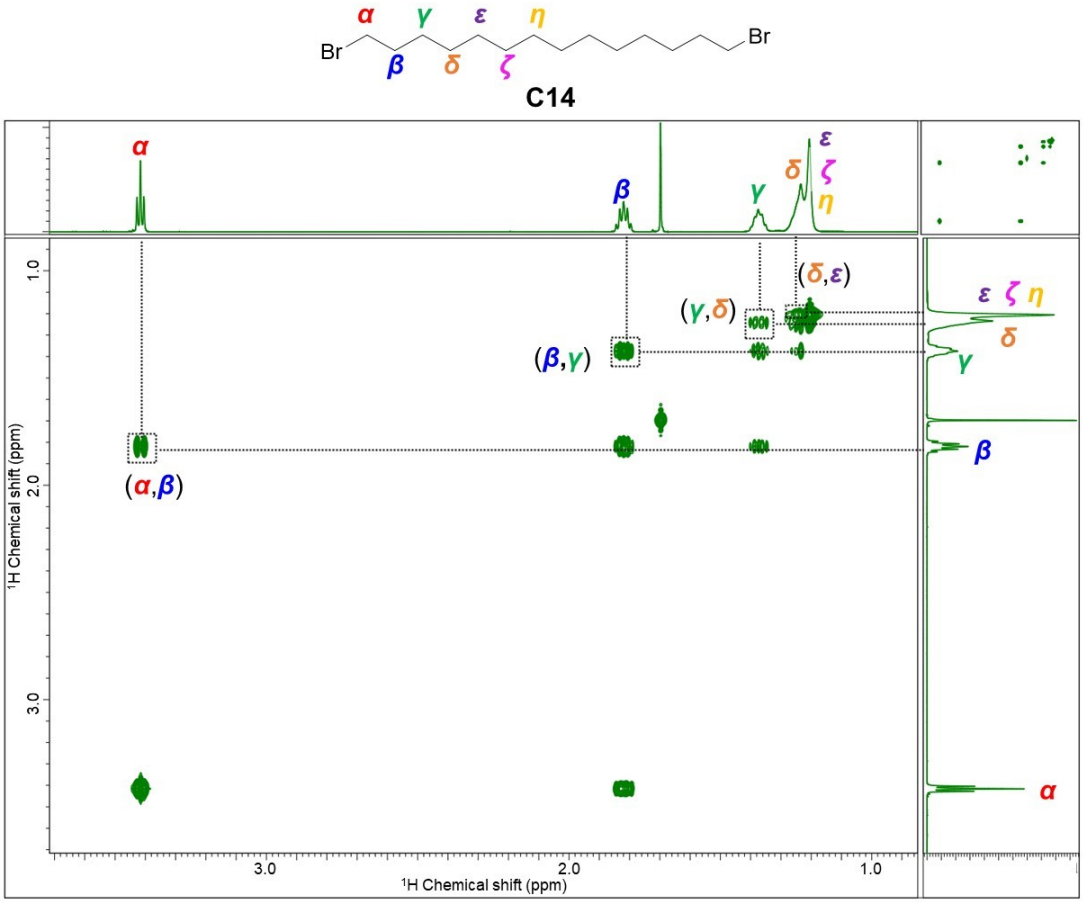

Figure S52. Partial ^{1}H–^{1}H COSY NMR (600 MHz, $CDCl_3$, 233 K) spectrum of **C14** (5.0 mM).

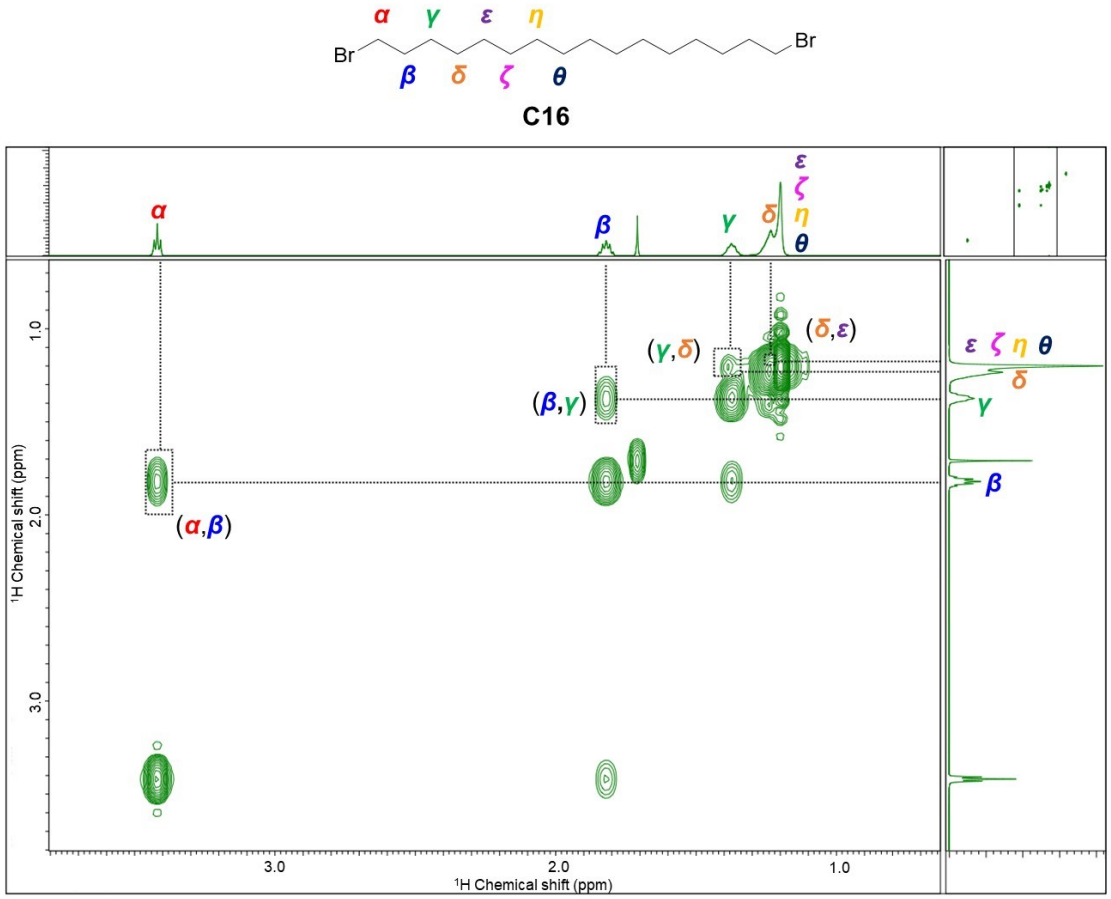

Figure S53. Partial ^{1}H–^{1}H COSY NMR (600 MHz, $CDCl_3$, 233 K) spectrum of **C16** (5.0 mM).

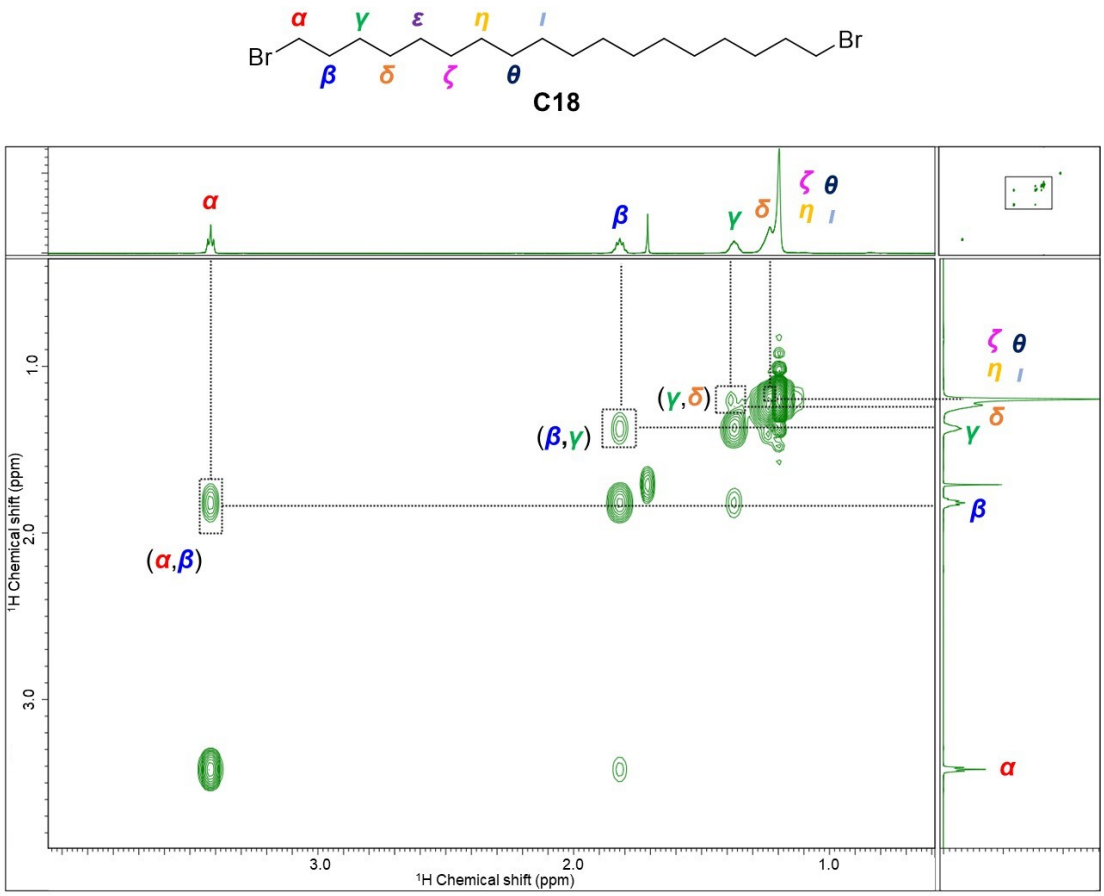

Figure S54. Partial ^{1}H–^{1}H COSY NMR (600 MHz, $CDCl_3$, 233 K) spectrum of **C18** (5.0 mM).

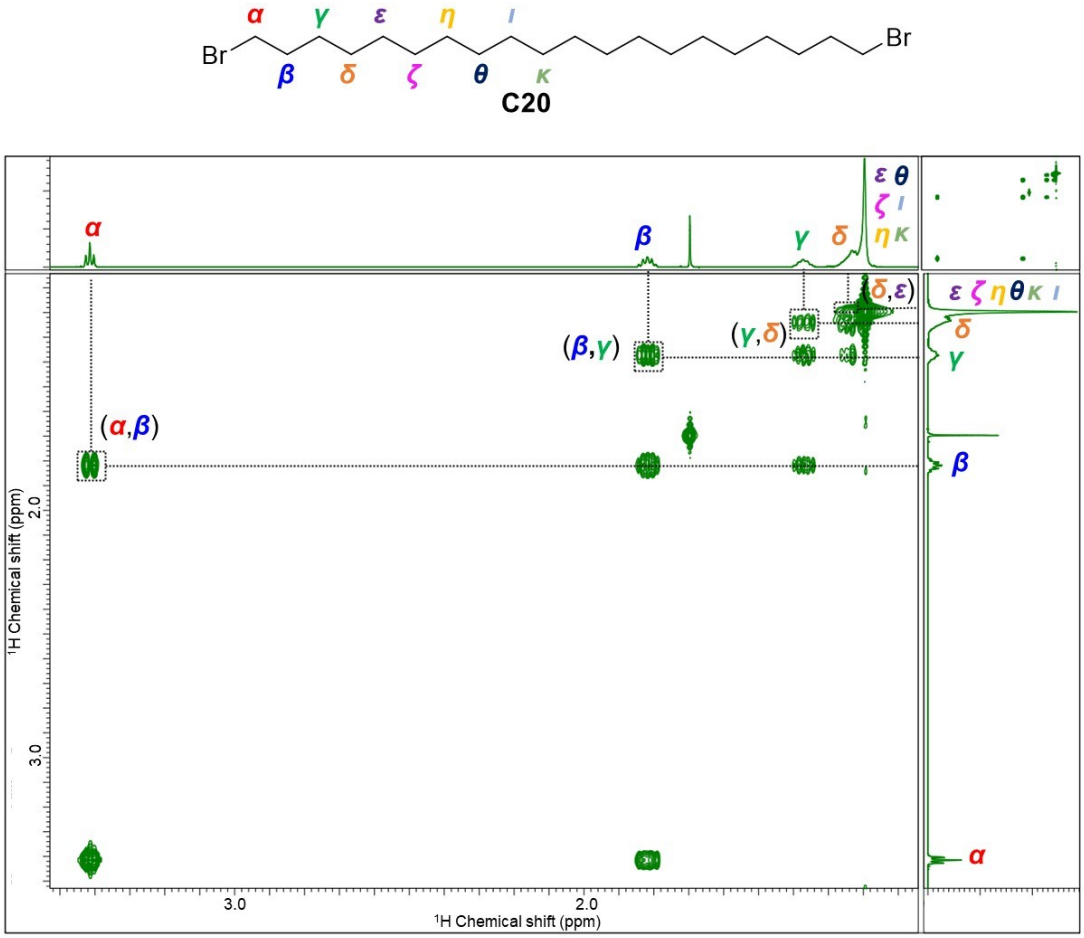

Figure S55. Partial ^{1}H–^{1}H COSY NMR (600 MHz, $CDCl_3$, 233 K) spectrum of **C20** (5.0 mM).

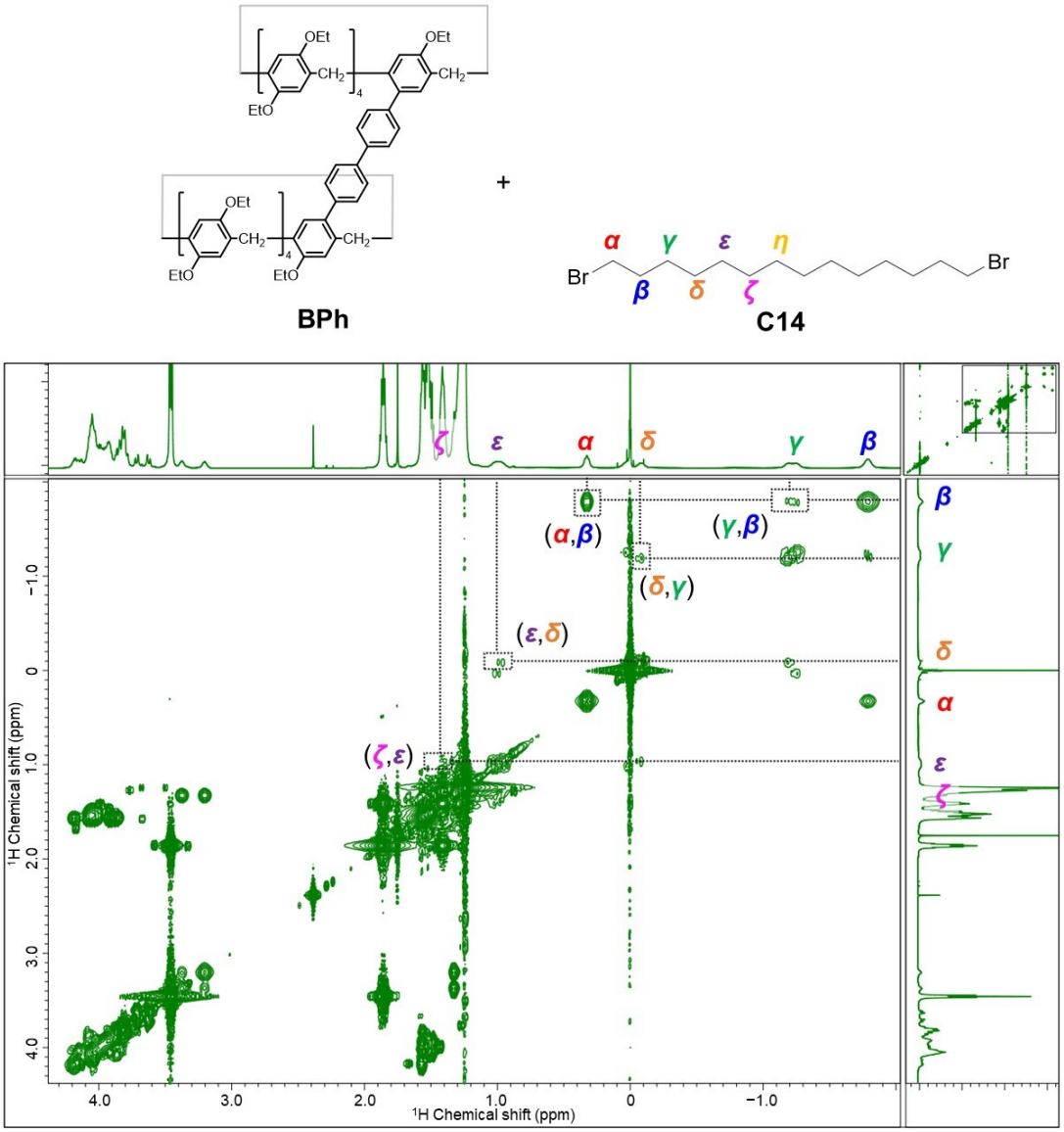

Figure S56. Partial ^{1}H–^{1}H COSY NMR (600 MHz, $CDCl_3$, 233 K) spectrum of **BPh** (1.0 mM) with the addition of 5.0 eq. of **C14**.

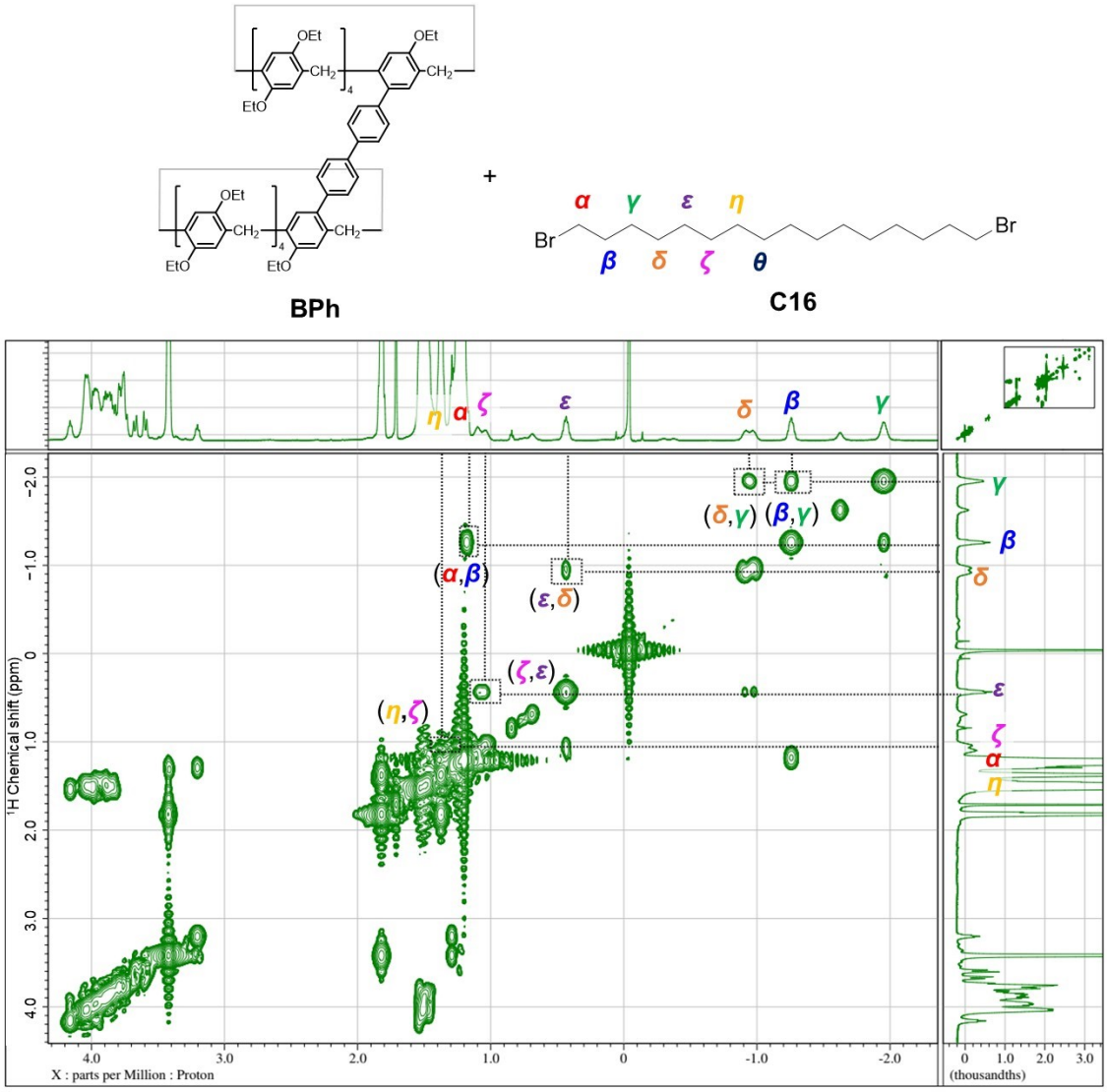

Figure S57. Partial ^{1}H–^{1}H COSY NMR (600 MHz, $CDCl_3$, 233 K) spectrum of **BPh** (1.0 mM) with the addition of 5.0 eq. of **C16**.

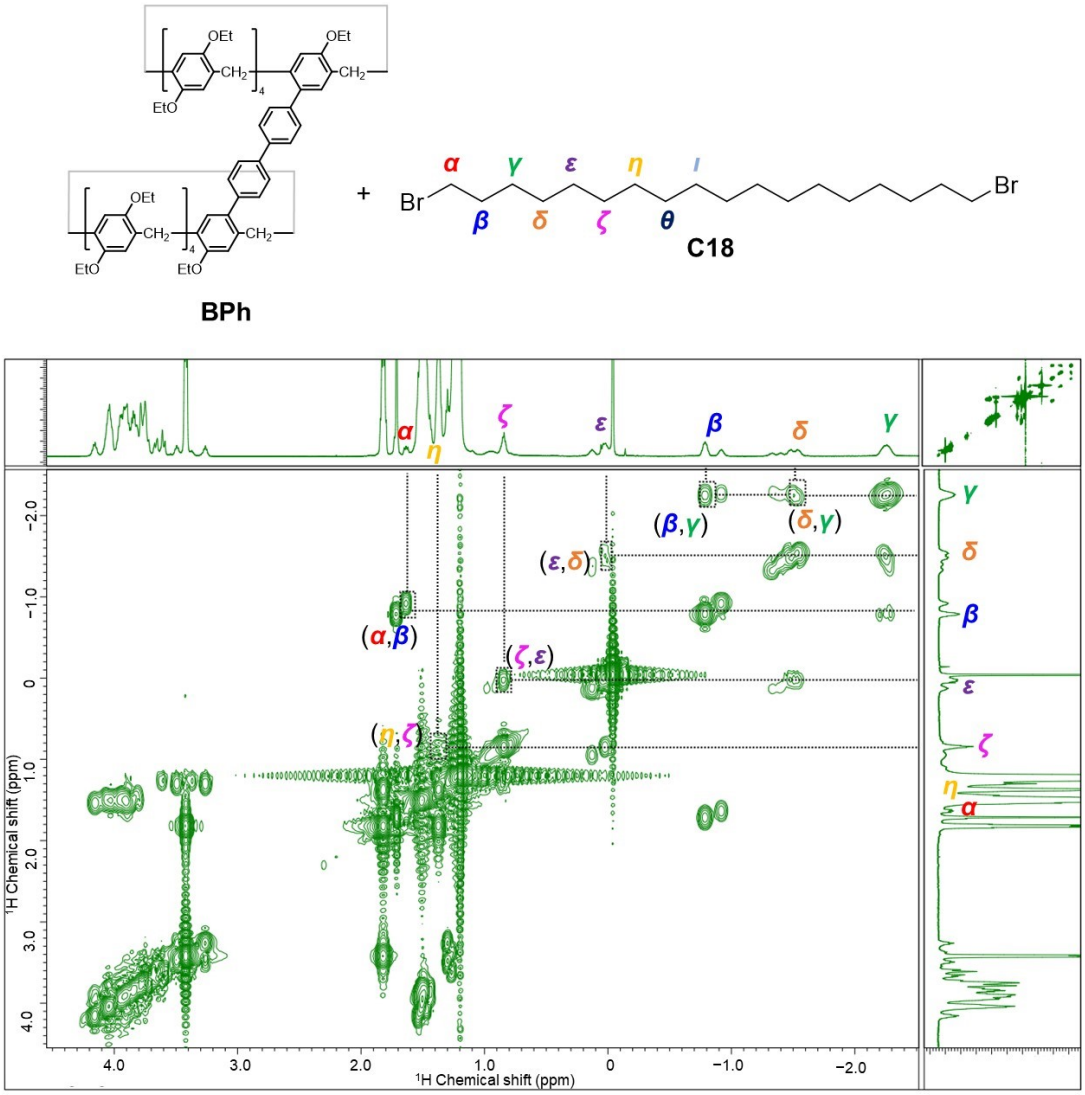

Figure S58. Partial ^{1}H–^{1}H COSY NMR (600 MHz, $CDCl_3$, 233 K) spectrum of **BPh** (1.0 mM) with the addition of 5.0 eq. of **C18**.

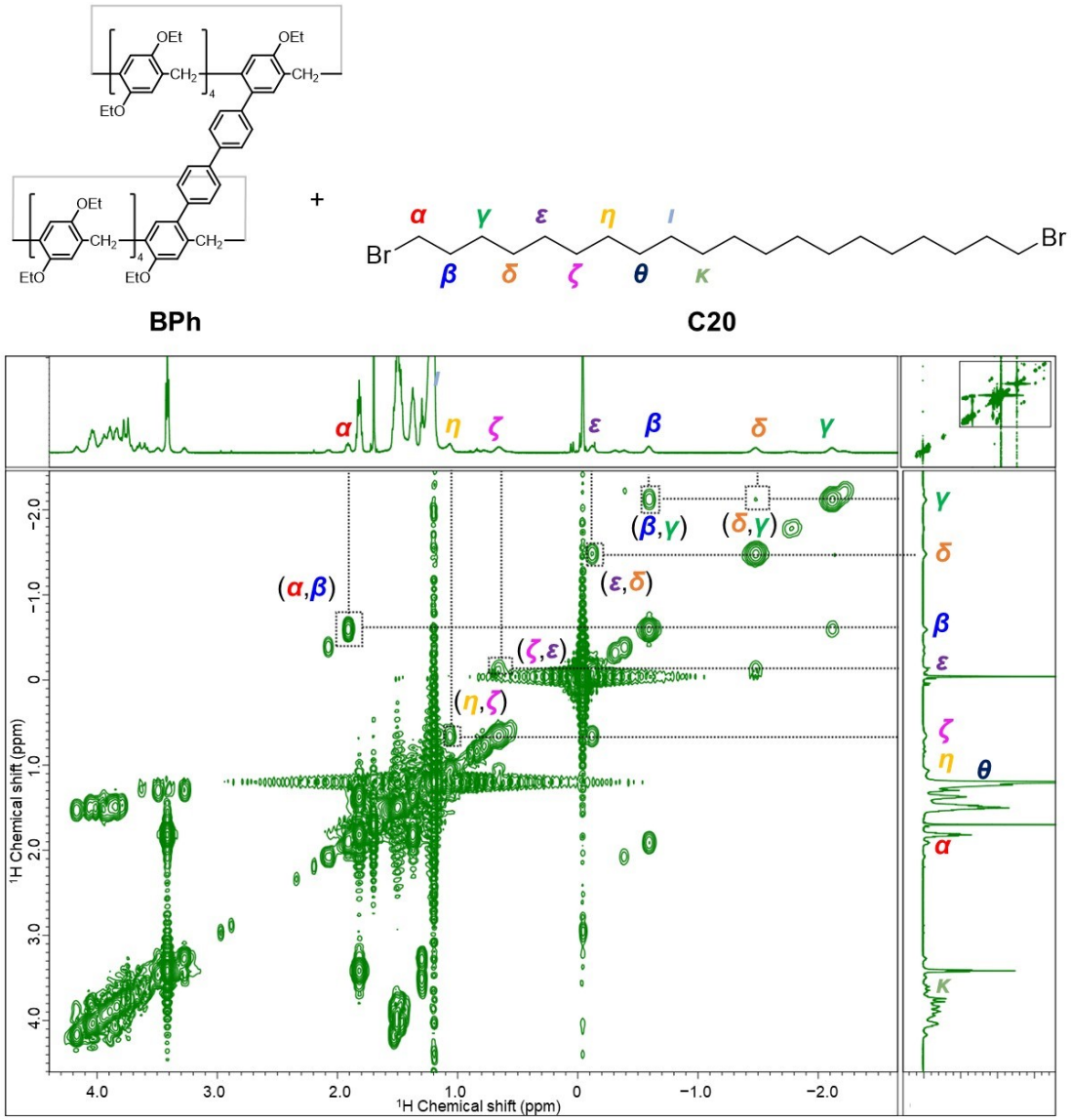

Figure S59. Partial ^{1}H–^{1}H COSY NMR (600 MHz, $CDCl_3$, 233 K) spectrum of **BPh** (1.0 mM) with the addition of 5.0 eq. of **C20**.

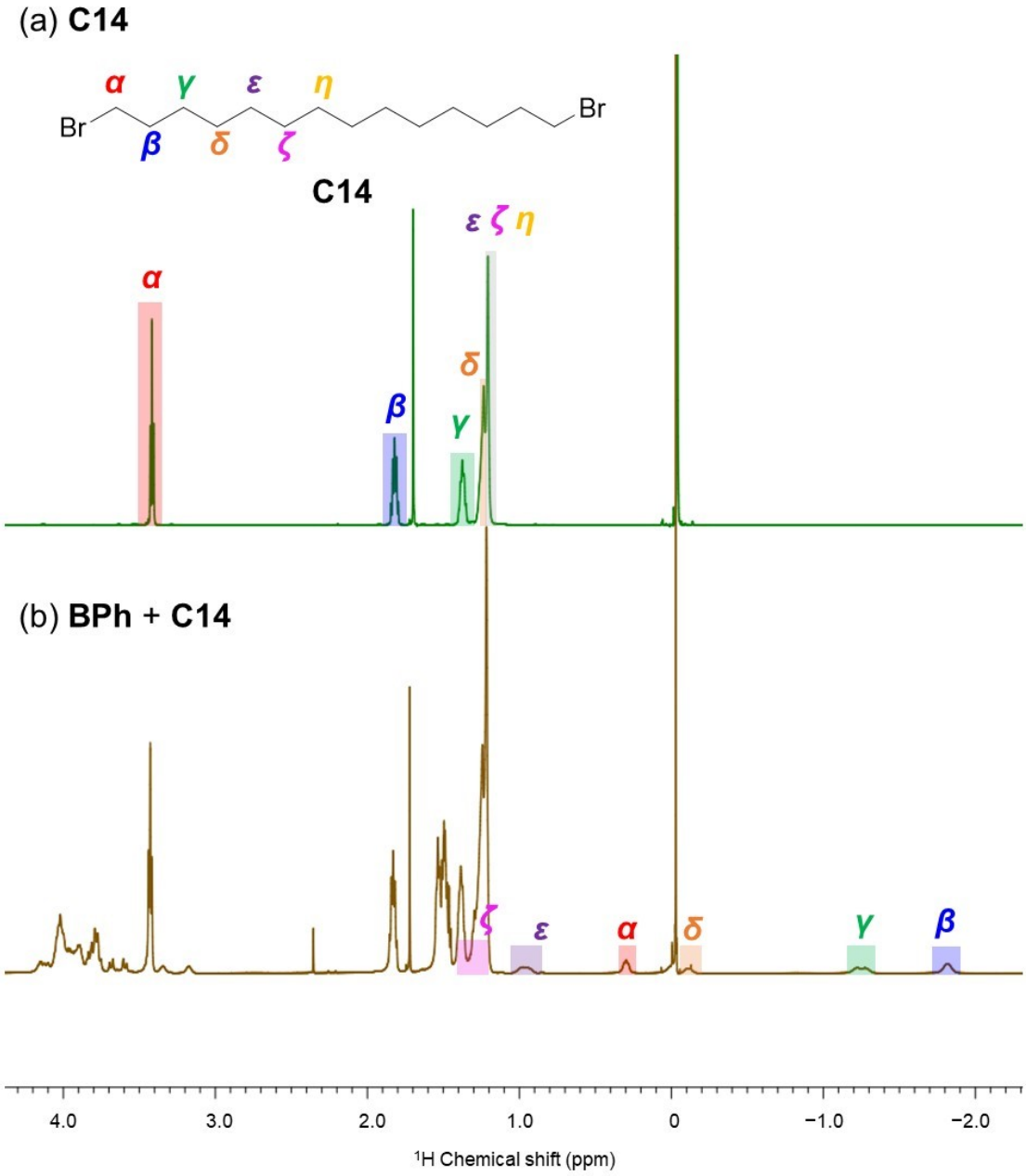

Figure S60. Partial ^{1}H NMR spectra (600 MHz, $CDCl_3$, 233 K) of (a) **C14** (5.0 mM) and (b) **BPh** (1.0 mM) with the addition of 5.0 eq. of **C14**.

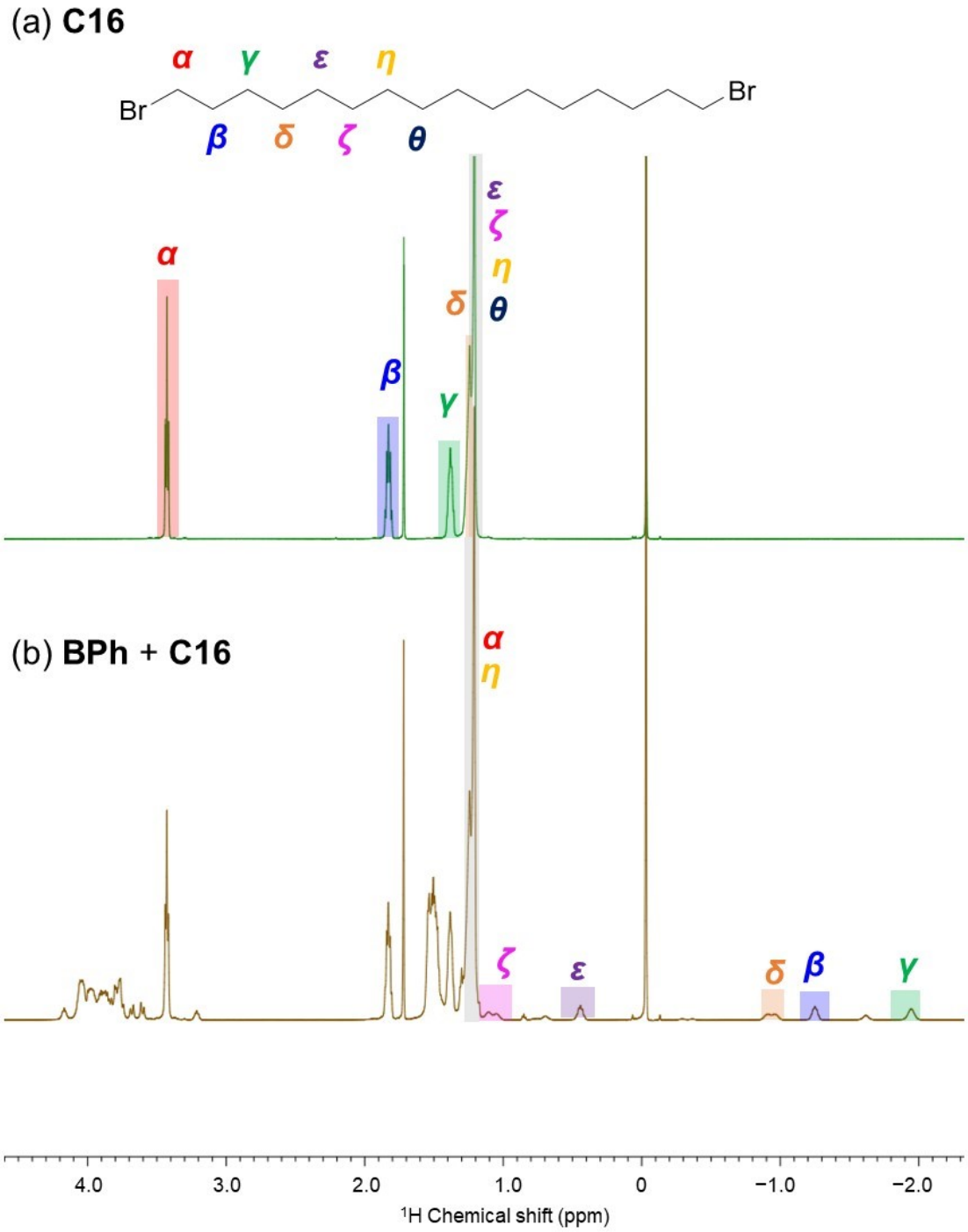

Figure S61. Partial ^{1}H NMR spectra (600 MHz, $CDCl_3$, 233 K) of (a) **C16** (5.0 mM) and (b) **BPh** (1.0 mM) with the addition of 5.0 eq. of **C16**.

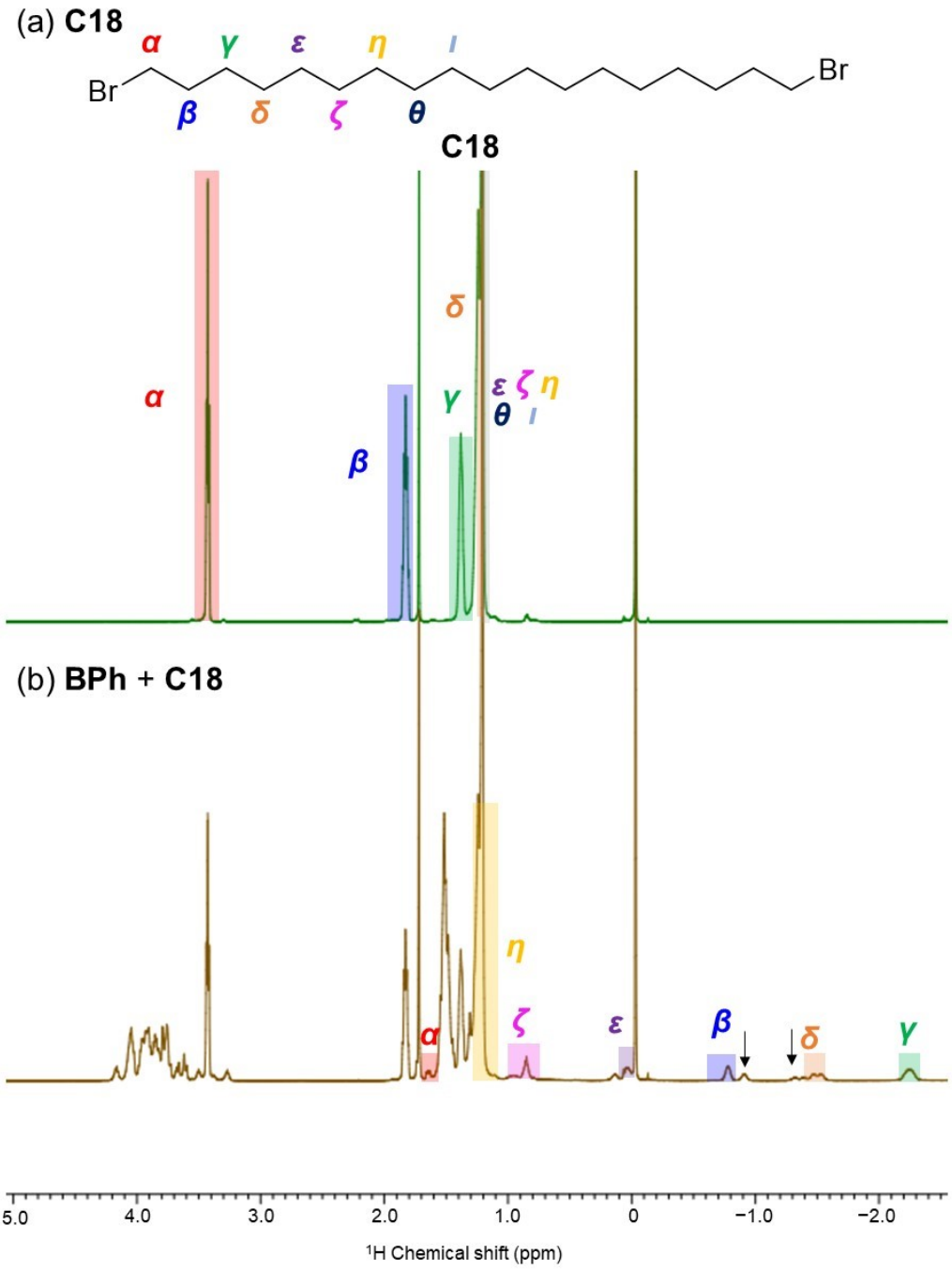

Figure S62. Partial ^{1}H NMR spectra (600 MHz, $CDCl_3$, 233 K) of (a) **C18** (5.0 mM) and (b) **BPh** (1.0 mM) with the addition of 5.0 eq. of **C18**.

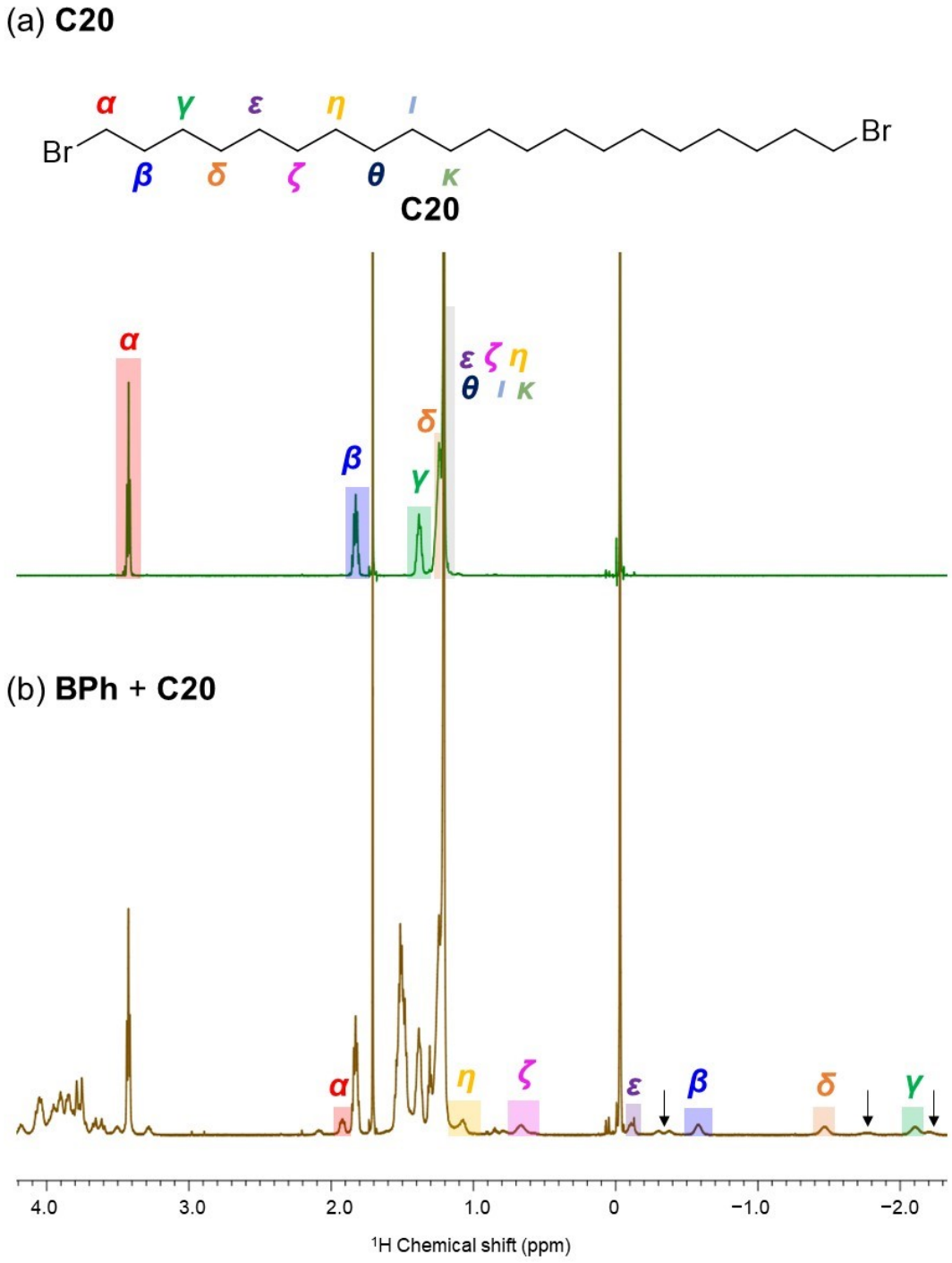

Figure S63. Partial ^{1}H NMR spectra (600 MHz, $CDCl_3$, 233 K) of (a) **C20** (5.0 mM) and (b) **BPh** (1.0 mM) with the addition of 5.0 eq. of **C20**.

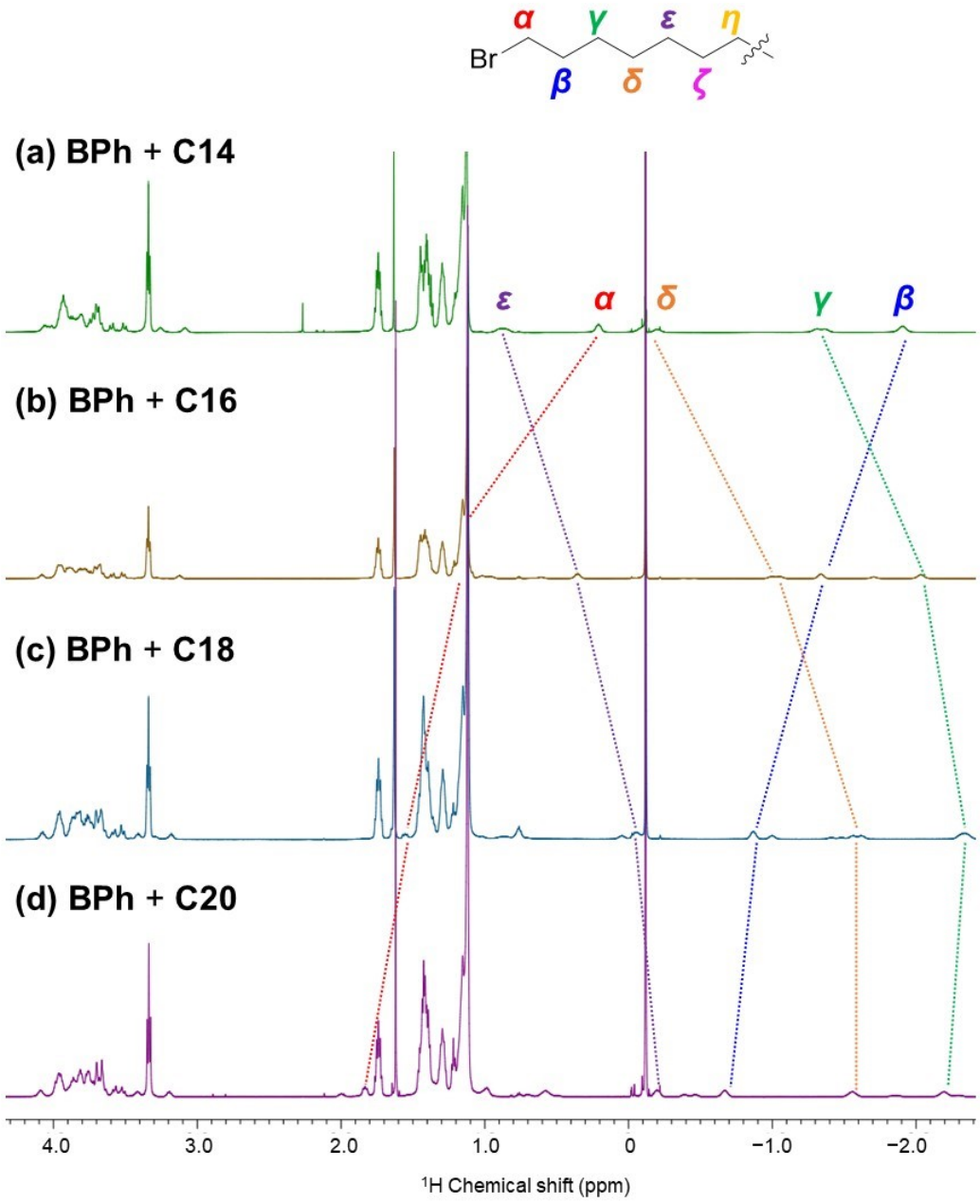

Figure S64. Chemical-shift changes of H_{α}, H_{β}, H_{γ}, H_{δ}, and H_{ε} protons of **C14**, **C16**, **C18** and **C20** (5.0 mM, $CDCl_3$, 233 K) with 1.0 mM of **BPh**.

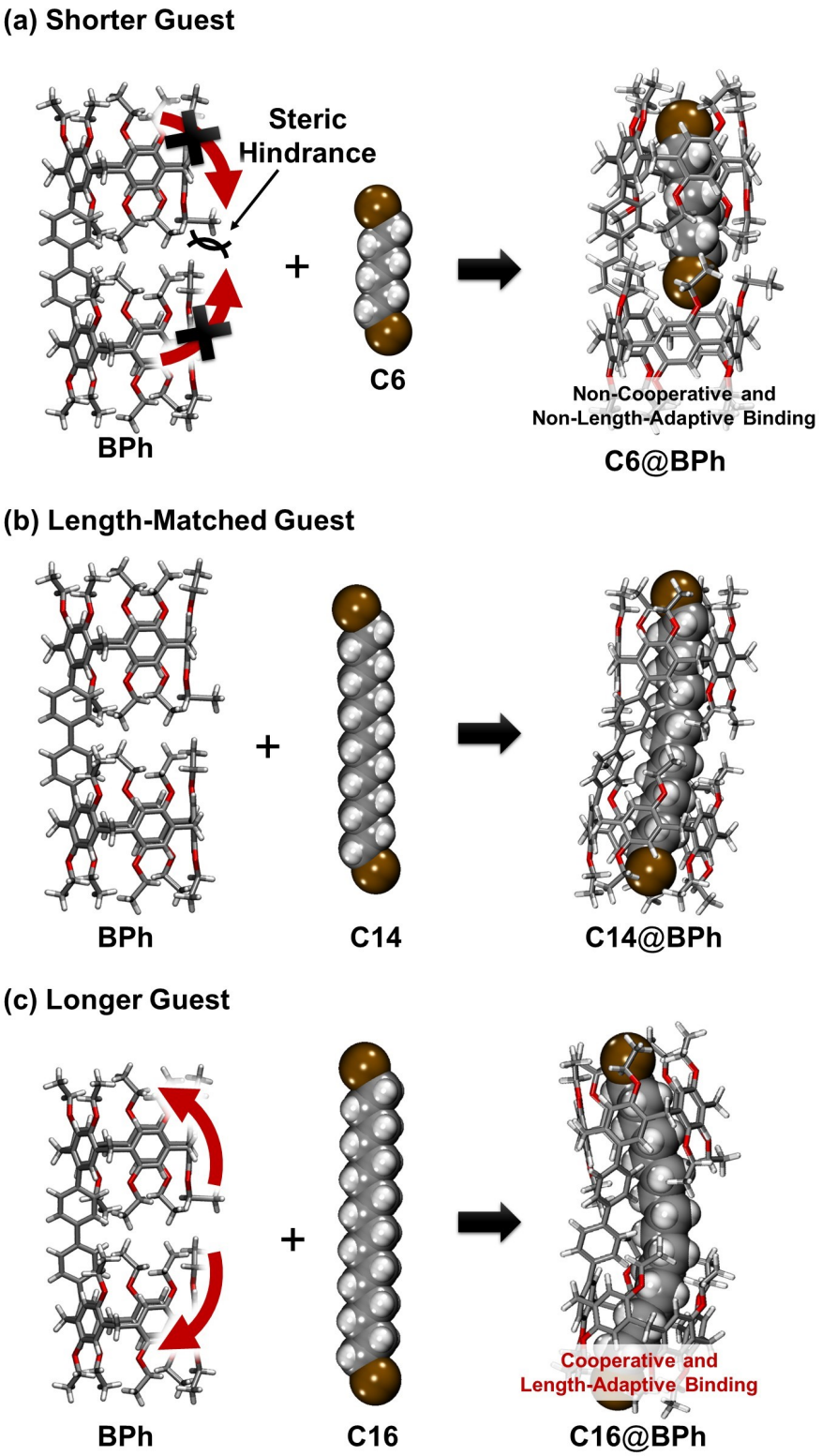

Figure S65. Schematic representation of host–guest behaviors of **BPh** with different guest lengths using geometries optimized at the M06-2X/6-31G(d,p) level of theory.

ESI Note 5

All quantum chemical calculations were performed using Gaussian 16 computational software package.[S14] Geometries of **BPh**, **C14@BPh**, **C16@BPh**, **C18@BPh** and **C20@BPh** were optimized at M06-2X/6-31G(d,p) level of theory.

^{1}H NMR spectra of **C16@BPh** and **C18@BPh** were calculated at B3LYP 6-311+G(2d,p) level of theory with SMD solvation model of chloroform on the basis of gauge-independent atomic orbital (GIAO) method. The calculated spectra were scaled (with scaling factors of −1.0784 (slope) and 31.8723 (intercept)) by Multiwfn 3.8[S15].

Since NMR chemical shifts result from a dynamic process, the chemical shift of H_f is calculated by averaging the values of corresponding H43 and H202 which are equivalent on the NMR time scale (Figure S66a). The distances between H202 and centroid (of the closest benzene rings of the linkages) were 2.630 Å and 2.792 Å for **C16@BPh** and **C18@BPh**, respectively (Figure S66b). This result suggests that the more curved structure of **C16@BPh** allows the H202 atom to come closer to the benzene ring of the linkers, leading to the more shieleded H202 due to ring current shielding effect than that of **C18@BPh**. However, the distance between H43 and centroid of the closest benzene ring of **C16@BPh** was longer than that of **C18@BPh**. H43 protons of **C16@BPh** and **C18@BPh** were not on the planes of benzene rings, and thus, the shielding effect was small. In fact, the shielding tensors for H43 protons of **C16@BPh** and **C18@BPh** were similar values (**C16@BPh**: 26.0099; **C18@BPh**: 26.2113), while those for H202 protons were largely different (**C16@BPh**: 26.7431; **C18@BPh**: 26.2516). Therefore, the contribution from H43 was small and only H202 might be responsible for the upfield-shift of H_f.

For the chemical shift of the free host of **BPh**, due to dynamic conformational change in the solution, the exact ratio of the *connected* conformation to the *unconnected* conformations (or other conformations) could not be determined, and thus, the chemical shift could not be predicted using DFT calculation.

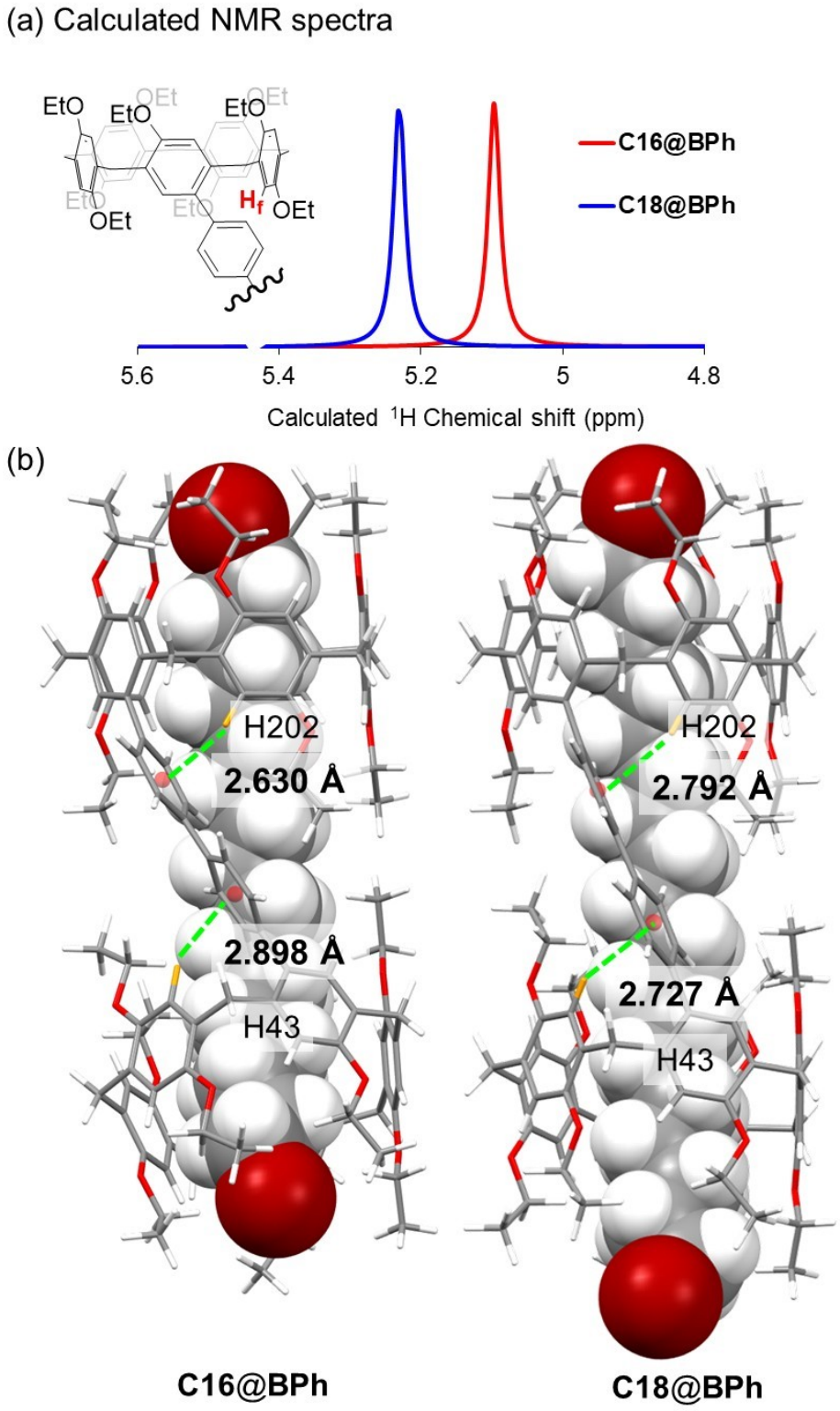

Figure S66. (a) Calculated H_f peaks and (b) the optimized geometries of **C16@BPh** and **C18@BPh** illustrating the distances of H202–centroid and H43–centroid.

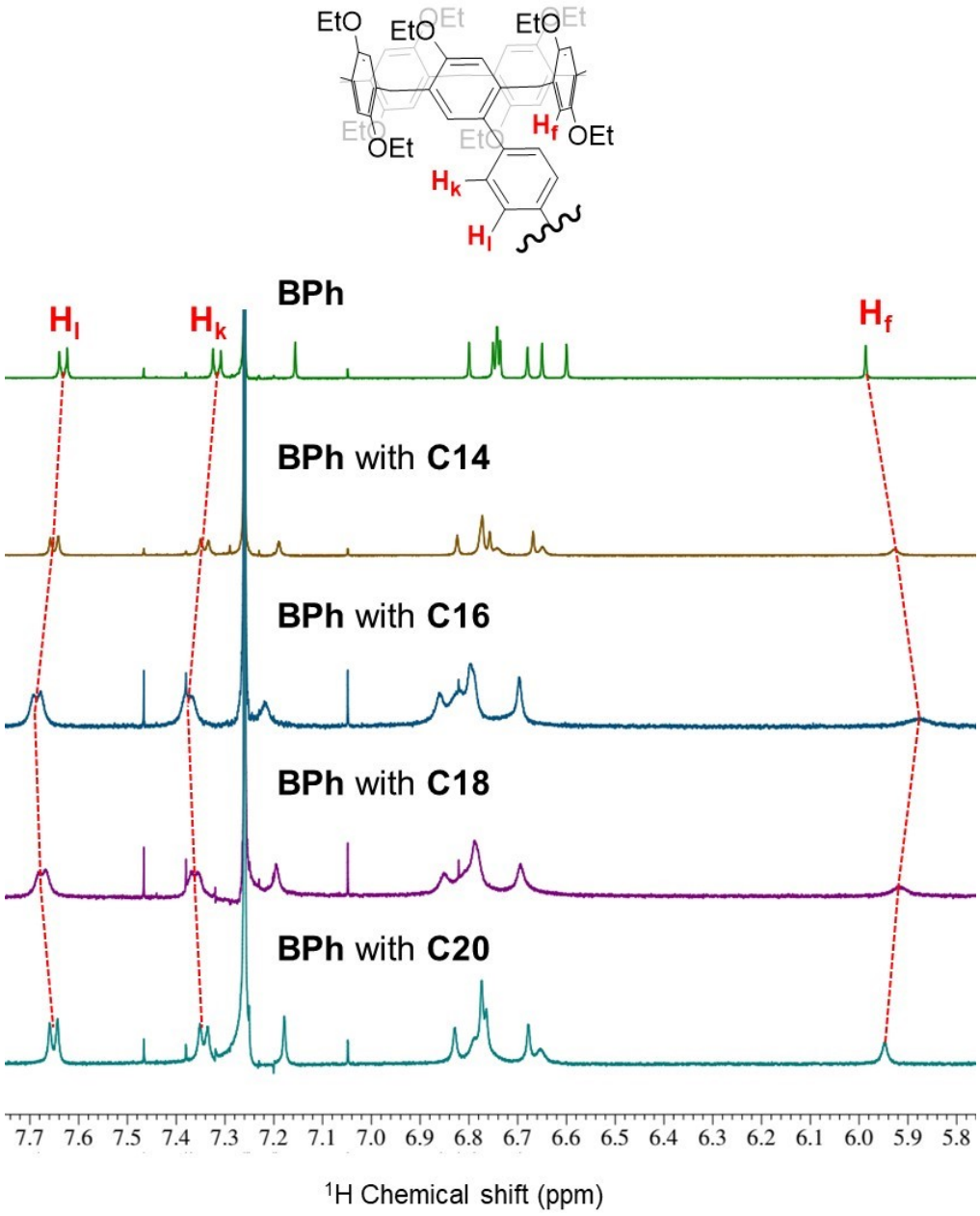

Figure S67. Chemical-shift changes of H_f, H_k, and H_l protons of **BPh** (0.50 mM, $CDCl_3$, 295 K) with 1.0 eq. of *α*,*ω*-dibromoalkanes (**C14**, **C16**, **C18** and **C20**).

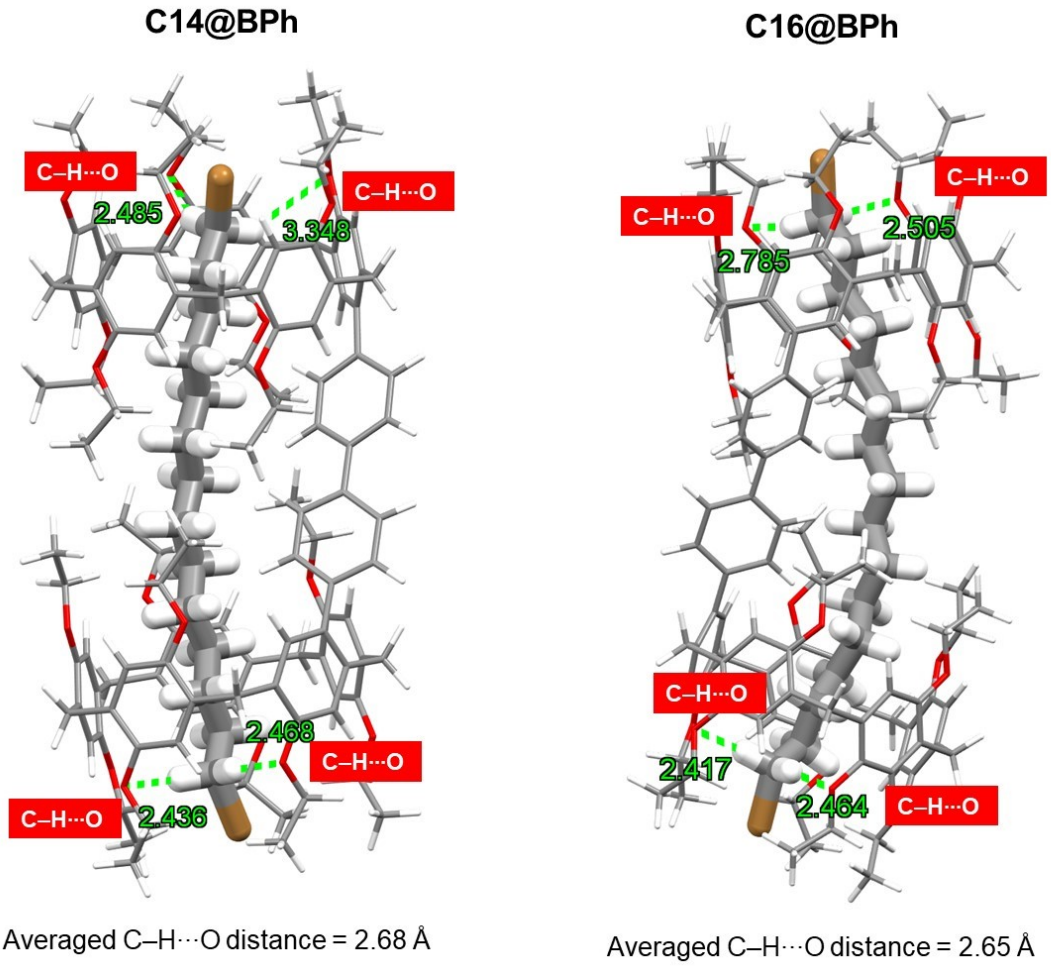

Figure S68. The optimized geometries of **BPh@C14** and **BPh@C16** illustrating the closest distances of C–H···O and the averaged values are noted.

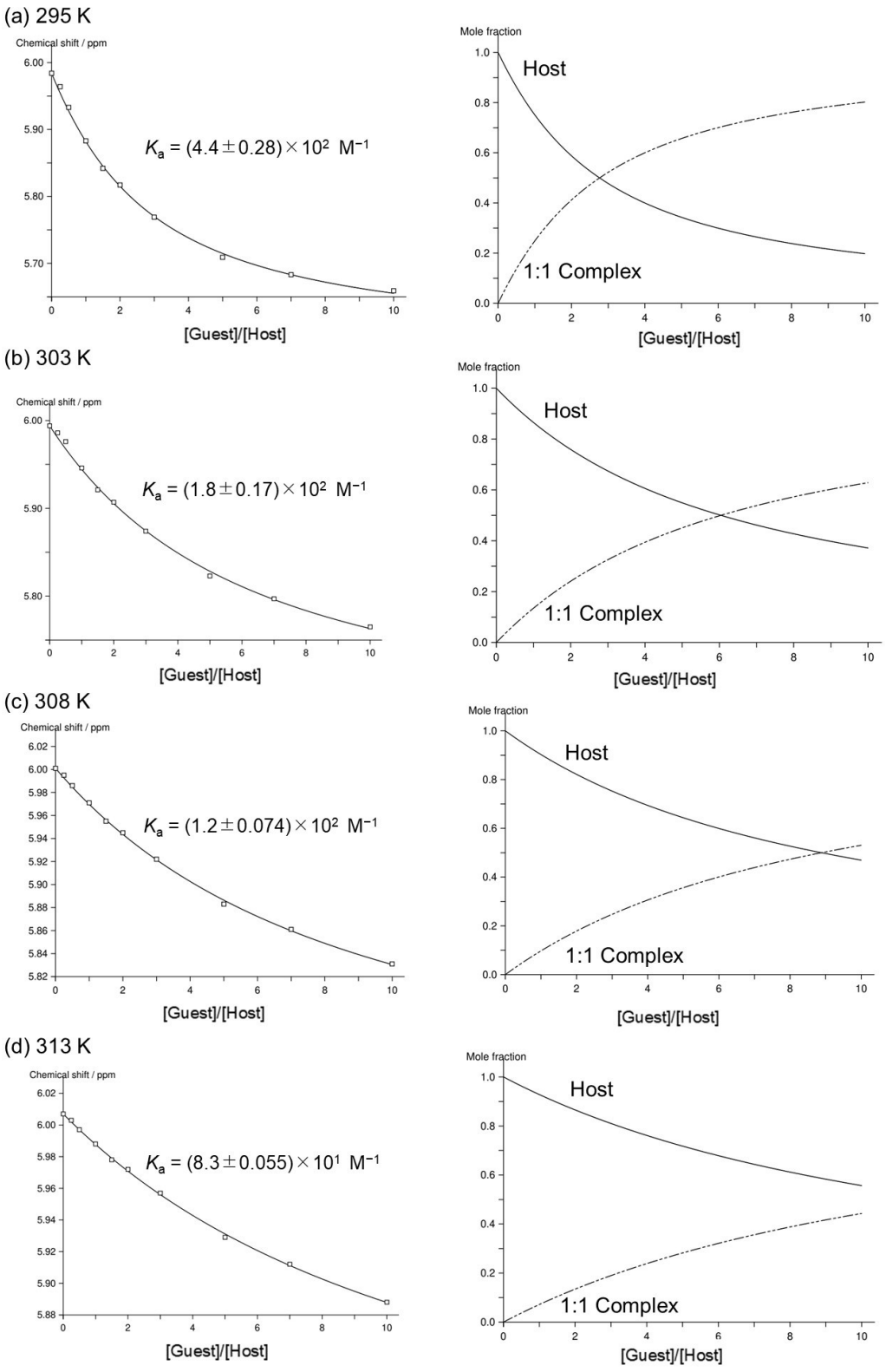

Figure S69. The non-linear curve fitting and the mole fraction of the species for the titration experiments of **BPh** for **C14** at (a) 295 K, (b) 303 K, (c) 308 K, and (d) 313 K.

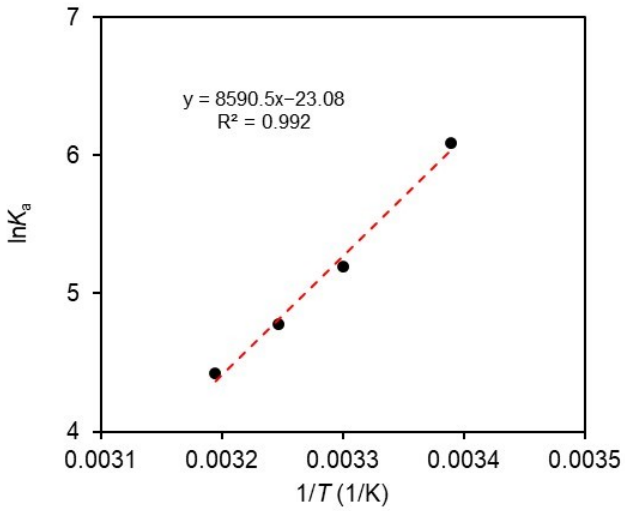

Figure S70. Van't Hoff plot for the titration experiment of **BPh** for **C14**.

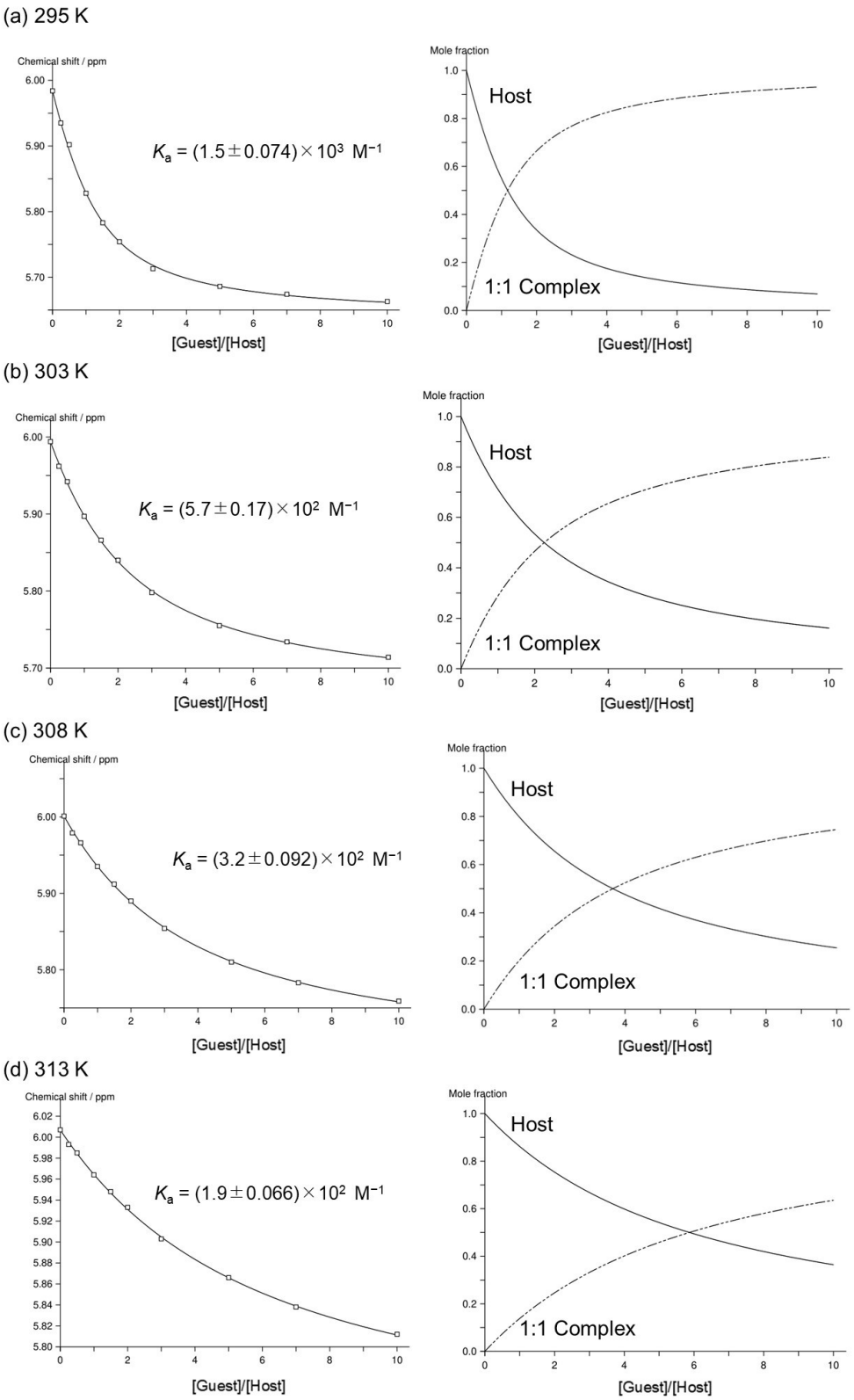

Figure S71. The non-linear curve fitting and the mole fraction of the species for the titration experiments of **BPh** for **C16** at (a) 295 K, (b) 303 K, (c) 308 K, and (d) 313 K.

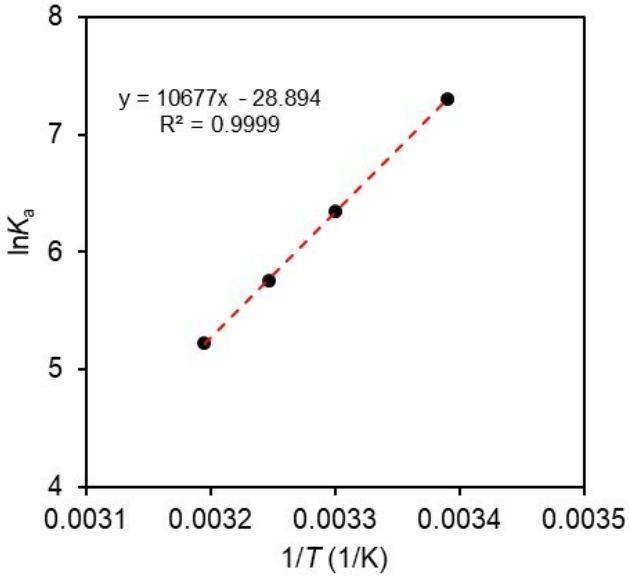

Figure S72. Van't Hoff plot for the titration experiment of **BPh** for **C16**.

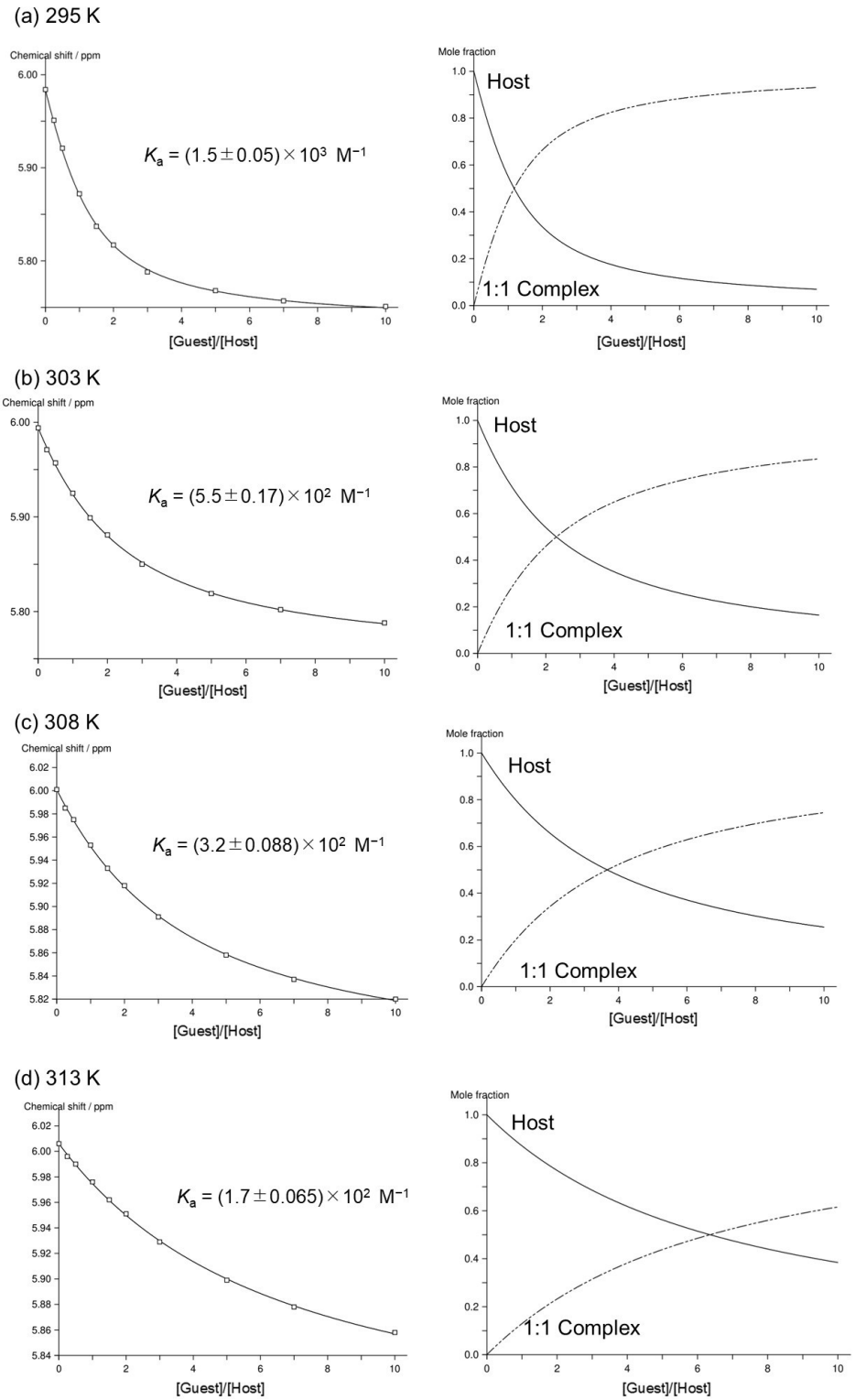

Figure S73. The non-linear curve fitting and the mole fraction of the species for the titration experiments of **BPh** for **C18** at (a) 295 K, (b) 303 K, (c) 308 K and (d) 313 K.

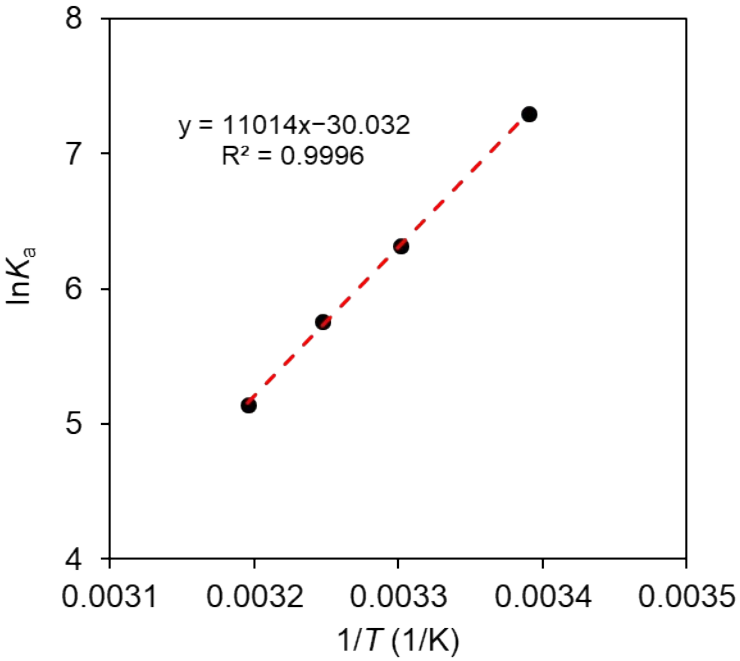

Figure S74. Van't Hoff plot for the titration experiment of **BPh** for **C18**.

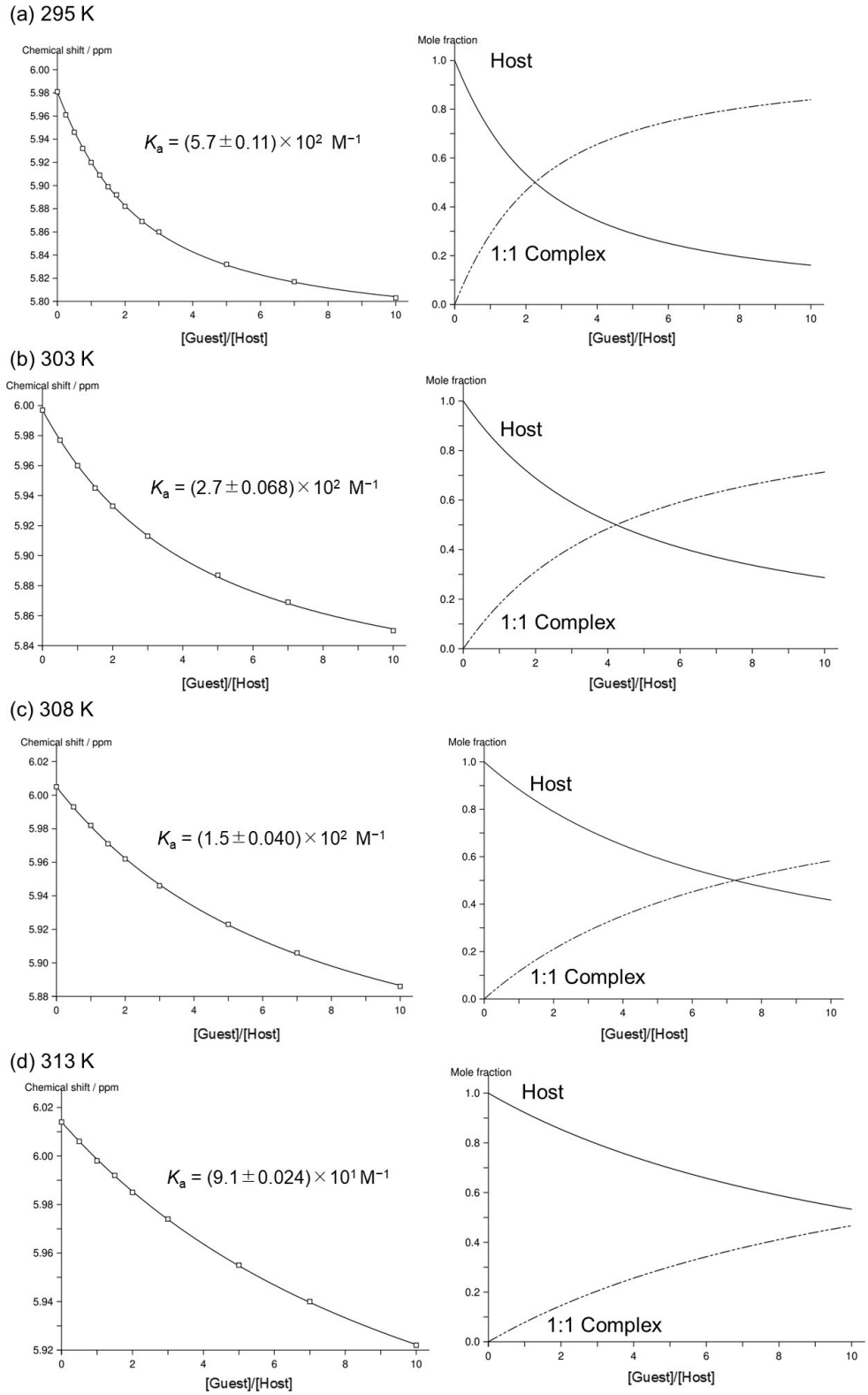

Figure S75. The non-linear curve fitting and the mole fraction of the species for the titration experiments of **BPh** for **C20** at (a) 295 K, (b) 303 K, (c) 308 K, and (d) 313 K.

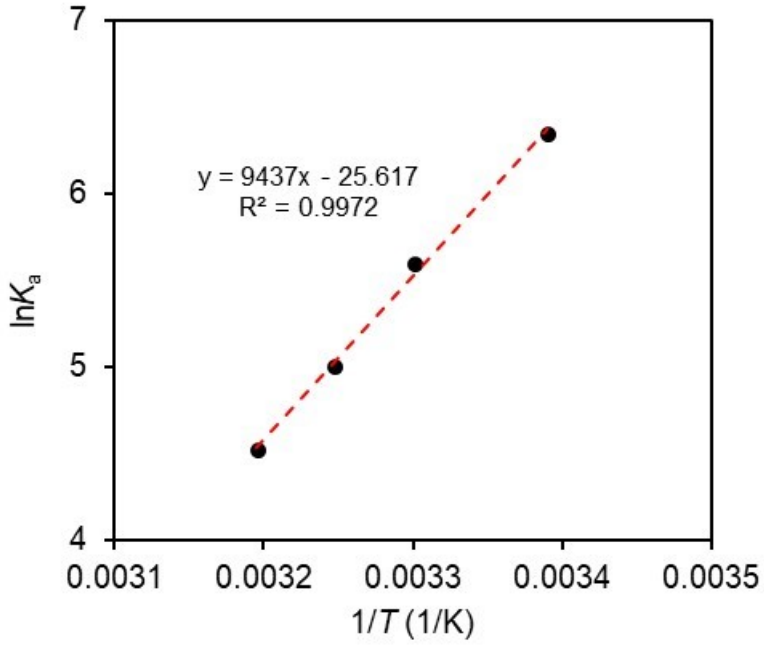

Figure S76. Van't Hoff plot for the titration experiment of **BPh** for **C20**.

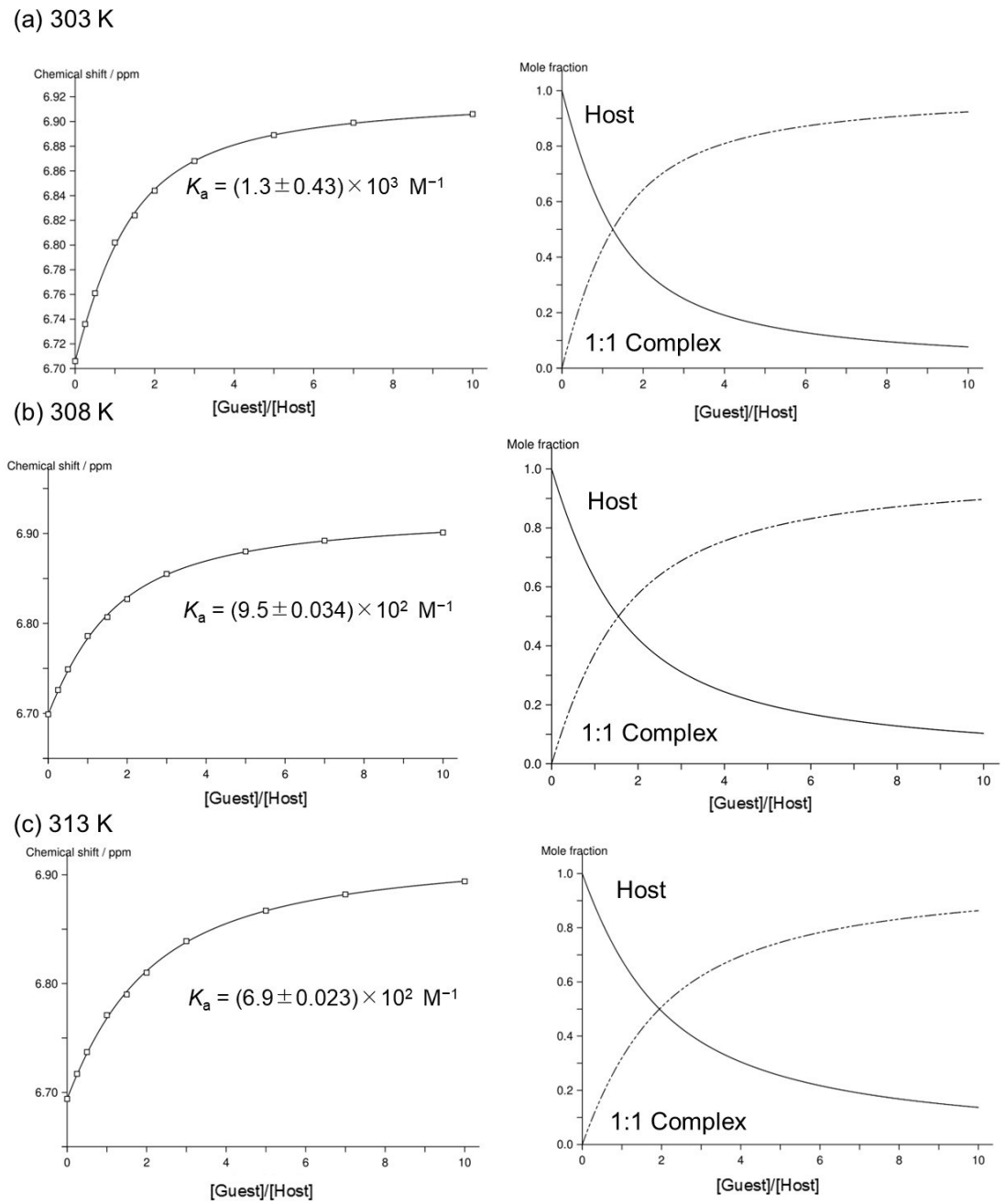

Figure S77. The non-linear curve fitting and the mole fraction of the species for the titration experiments of **1** for **C2** at (a) 303 K, and (b) 308 K, (c) 313 K.

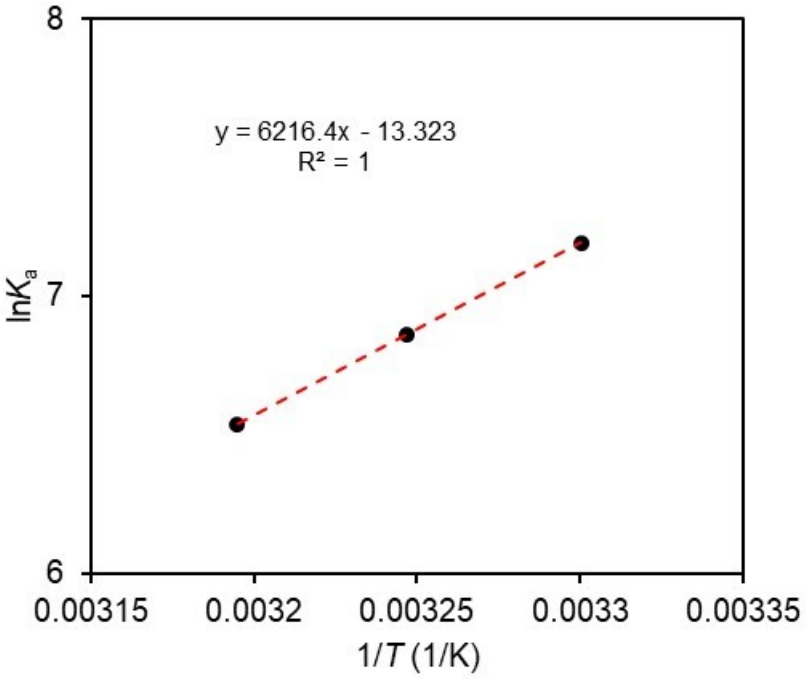

Figure S78. Van't Hoff plot for the titration experiment of **1** for **C2**.

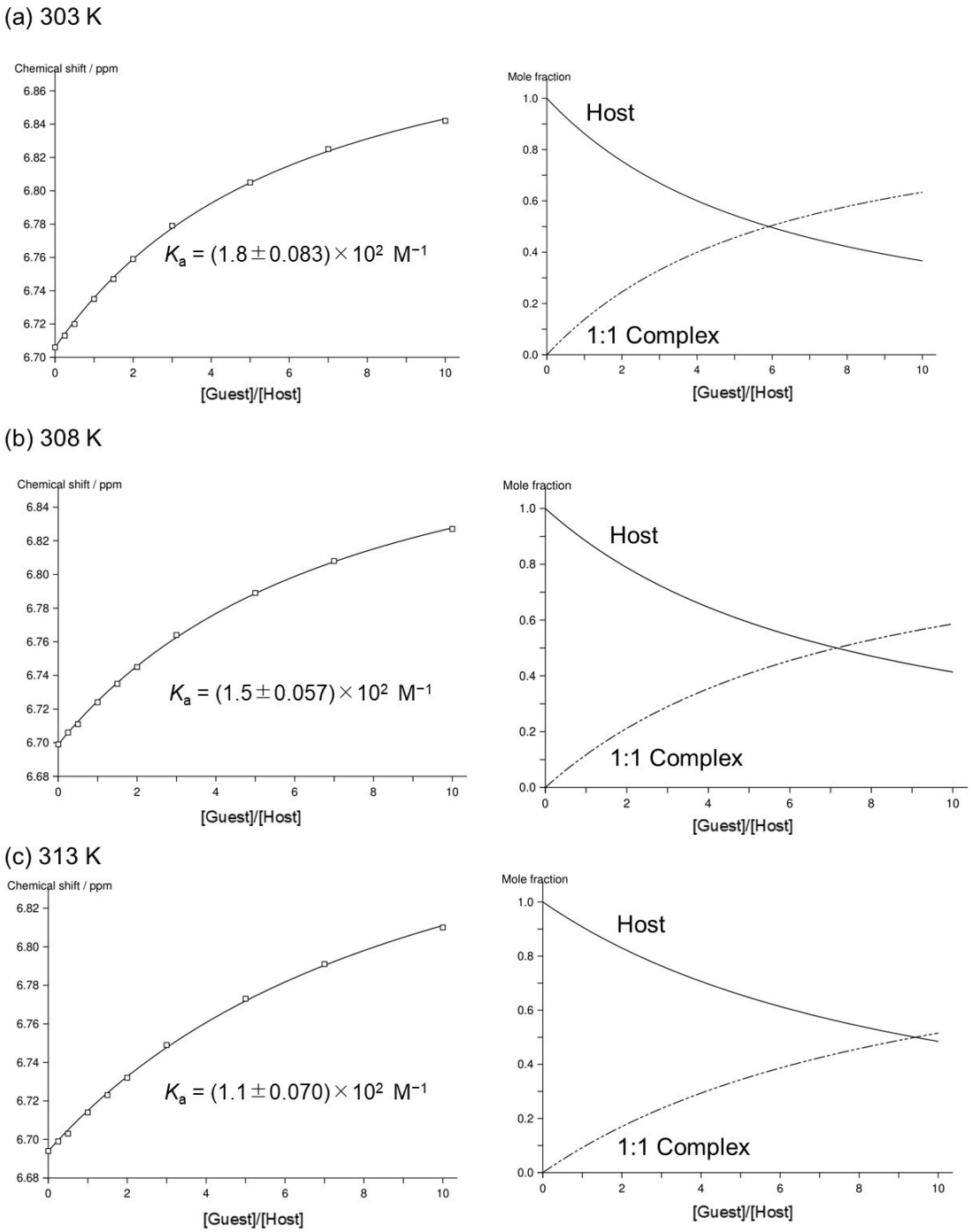

Figure S79. The non-linear curve fitting and the mole fraction of the species for the titration experiments of **1** for **C3** at (a) 303 K, (b) 308 K, and (c) 313 K.

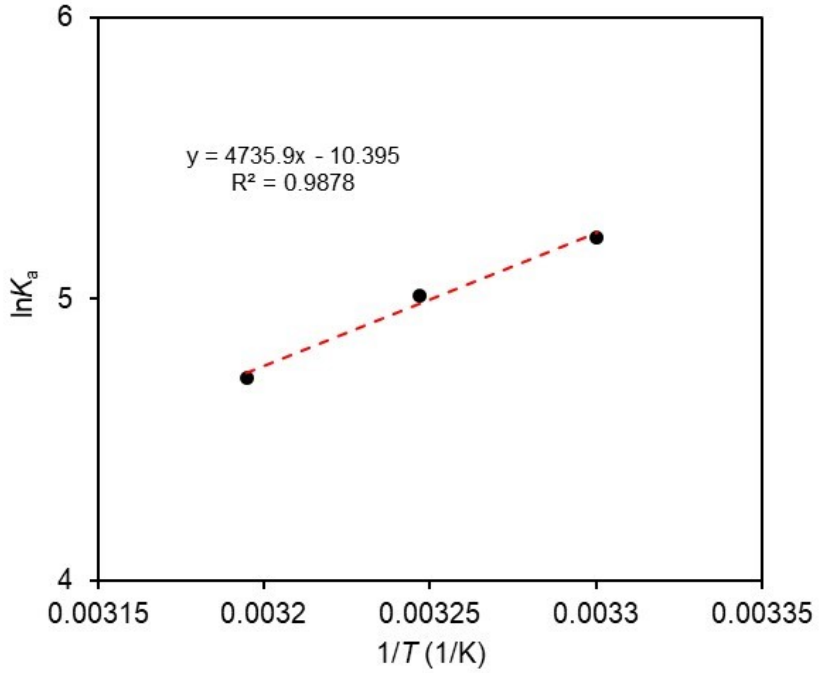

Figure S80. Van't Hoff plot for the titration experiment of **1** for **C3**.

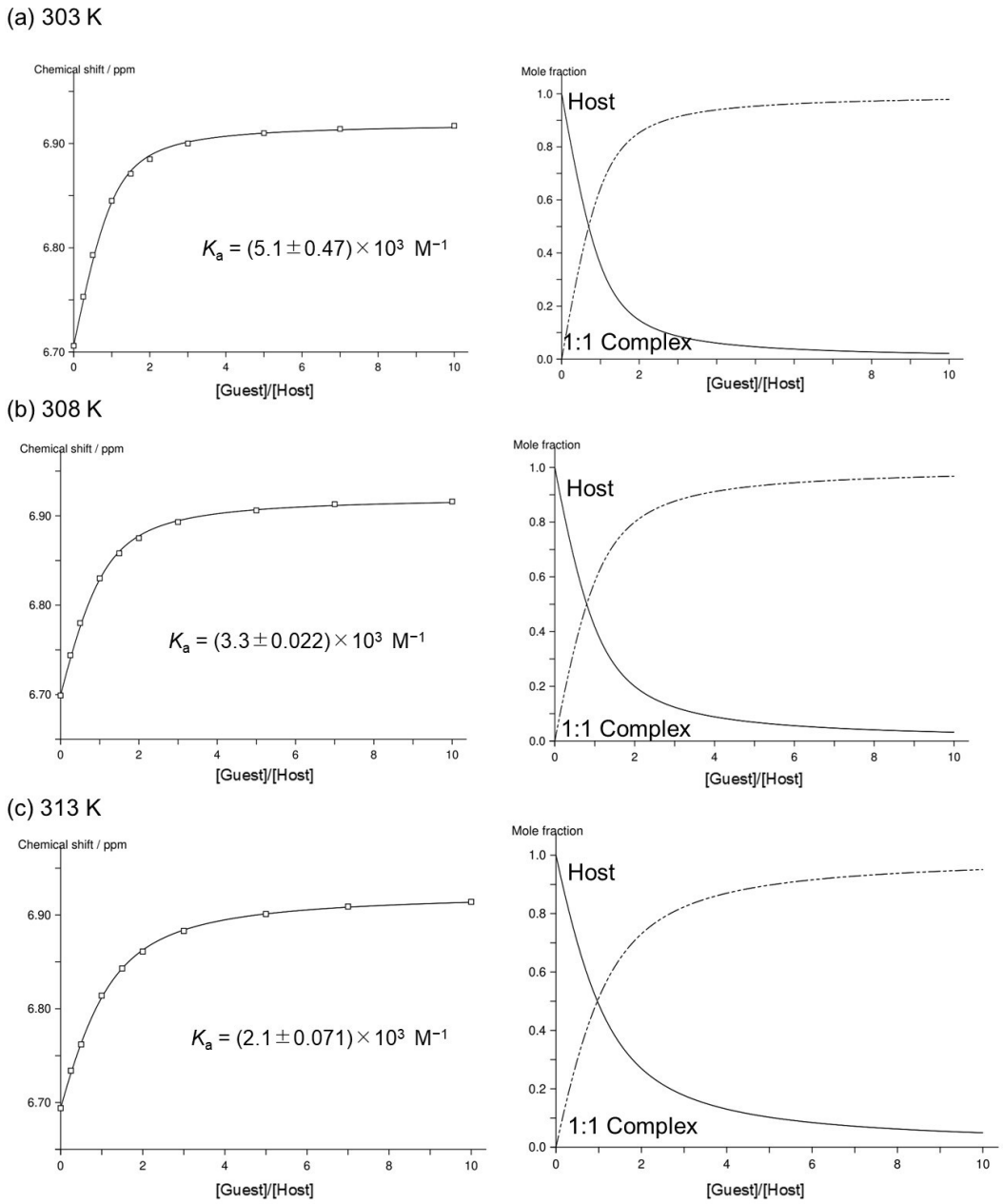

Figure S81. The non-linear curve fitting and the mole fraction of the species for the titration experiments of **1** for **C4** at (a) 303 K, (b) 308 K, and (c) 313 K.

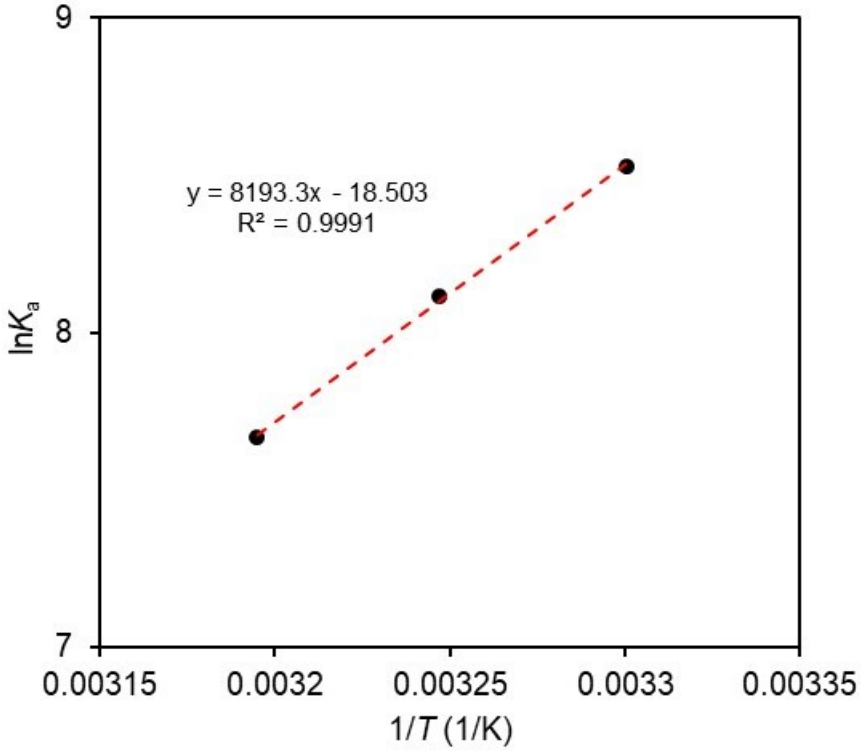

Figure S82. Van't Hoff plot for the titration experiment of **1** for **C4**.

Table S4. Calculated strain energies (ΔE_{strain}s) of **BPh** and guests upon host–guest complexation at M06-2X/6-31G(d,p) level of theory

	C14@BPh	**C16@BPh**	**C18@BPh**	**C20@BPh**
$\Delta E_{strain,host}$ (kcal/mol)	14.6	11.6	12.0	10.5
$\Delta E_{strain,guest}$ (kcal/mol)	2.17	5.13	3.76	2.95
$\Delta E_{strain,total}$ (kcal/mol)	16.8	16.7	15.8	13.5

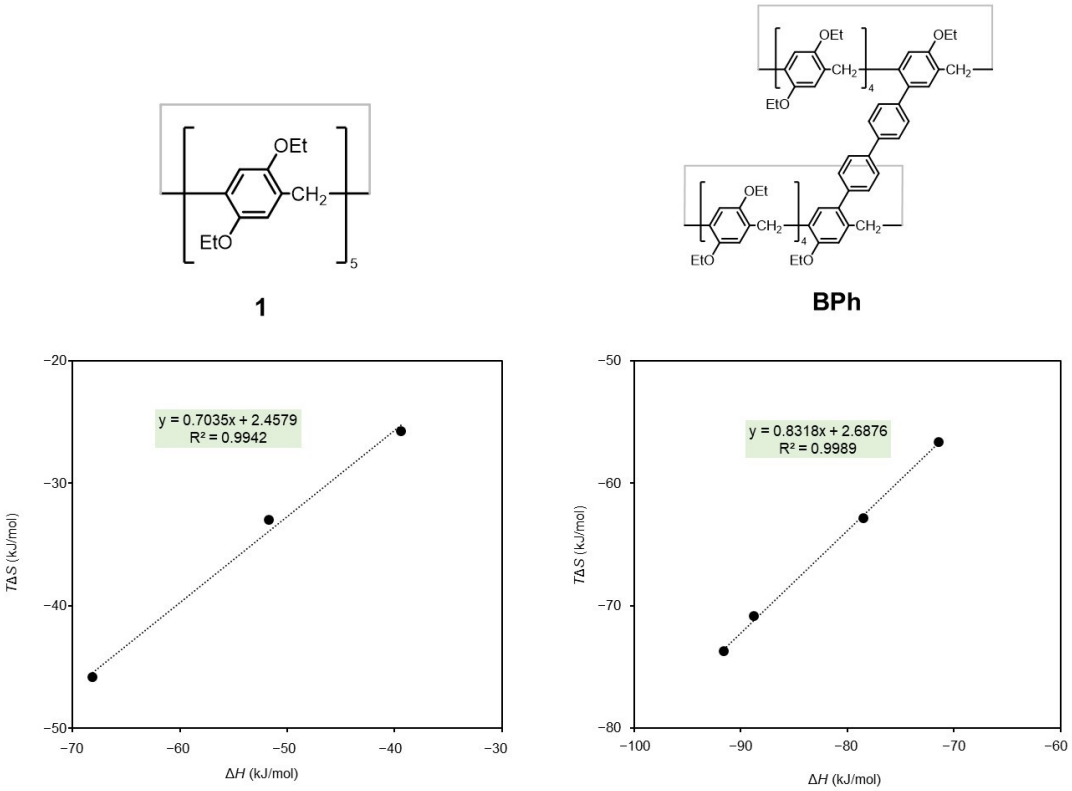

Figure S83. Enthalpy–entropy compensation plots of **1** and **BPh**.

References

S1. S. Akine, TitrationFit, program for analyses of host-guest complexation, Kanazawa University, Kanazawa, Japan, 2013. (http://chem.s.kanazawa-u.ac.jp/coord/titrationfit_e.html)

S2. T. Ogoshi, K. Kitajima, T. Aoki, S. Fujinami, T. Yamagishi and Y. Nakamoto, *J. Org. Chem.*, 2010, **75**, 3268–3273.

S3. T. H. Shi, Y. Nagata, S. Akine, S. Ohtani, K. Kato and T. Ogoshi, *J. Am. Chem. Soc.*, 2022, **144**, 23677–23684.

S4. T. Ogoshi, K. Demachi, K. Kitajima and T. Yamagishi, *Chem. Commun*. 2011, **47**, 7164–7166.

S5. V. Kardelis, K. Li, I. Nierengarten, M. Holler, J.-F. Nierengarten and A. Adronov, *Macromolecules*, 2017, **50**, 9144–9150.

S6. T. Kaneda, K. Kato, S. Ohtani and T. Ogoshi, *Bull. Chem. Soc. Jpn.*, 2024, **97** uoae093.

S7. P. Roesle, F. Stempfle, S. K. Hess, J. Zimmerer, C. Rio Bartulos, B. Lepetit, A. Eckert, P. G. Kroth and S. Mecking, *Angew. Chem. Int. Ed.*, 2014, **53**, 6800–6804.

S8. J. Castilla, R. Risquez, K. Higaki, E. Nanba, K. Ohno, Y. Suzuki, Y. Diaz, C. Ortiz Mellet, J. M. Garcia Fernandez and S. Castillon, *Eur. J. Med. Chem.*, 2015, **90**, 258–266.

S9. M. E. Weber, P. H. Schlesinger and G. W. Gokel, *J. Am. Chem. Soc.*, 2005, **127**, 636–642.

S10. Y. Yamashita, Y. Mutoh, R. Yamasaki, T. Kasama and S. Saito, *Chem. Eur. J.*, 2015, **21**, 2139–2145.

S11. Blaine M. Carter, L. Keller, M. Wessling and D. J. Miller, *J. Mater. Chem. A*, 2019, **7**, 23818–23829.

S12. X. Shu, J. Fan, J. Li, X. Wang, W. Chen, X. Jia and C. Li, *Org. Biomol. Chem.*, 2012, **10**, 3393–3397.

S13. D. Brynn Hibbert and P. Thordarson, *Chem. Commun.*, 2016, **52**, 12792–12805.

S14. Gaussian 16, Revision C.01, M. J. Frisch, G. W. Trucks, H. B. Schlegel, G. E. Scuseria, M. A. Robb, J. R. Cheeseman, G. Scalmani, V. Barone, G. A. Petersson, H. Nakatsuji, X. Li, M. Caricato, A. V. Marenich, J. Bloino, B. G. Janesko, R. Gomperts, B. Mennucci, H. P. Hratchian, J. V. Ortiz, A. F. Izmaylov, J. L. Sonnenberg, D. Williams-Young, F. Ding, F. Lipparini, F. Egidi, J. Goings, B. Peng, A. Petrone, T. Henderson, D. Ranasinghe, V. G. Zakrzewski, J. Gao, N. Rega, G. Zheng, W. Liang, M. Hada, M. Ehara, K. Toyota, R. Fukuda, J. Hasegawa, M. Ishida, T. Nakajima, Y. Honda, O. Kitao, H. Nakai, T. Vreven, K. Throssell, J. A. Montgomery, Jr., J. E. Peralta, F. Ogliaro, M. J. Bearpark, J. J. Heyd, E. N. Brothers, K. N. Kudin, V. N. Staroverov, T. A. Keith, R. Kobayashi, J. Normand, K. Raghavachari, A. P. Rendell, J. C. Burant, S. S. Iyengar, J. Tomasi, M. Cossi, J. M. Millam, M. Klene, C. Adamo, R. Cammi, J. W. Ochterski, R. L. Martin, K. Morokuma, O. Farkas, J. B. Foresman, and D. J. Fox, Gaussian, Inc., Wallingford CT, 2016.T.

S15. Lu and F. Chen, *J. Comput. Chem.*, 2012, **33**, 580–592.